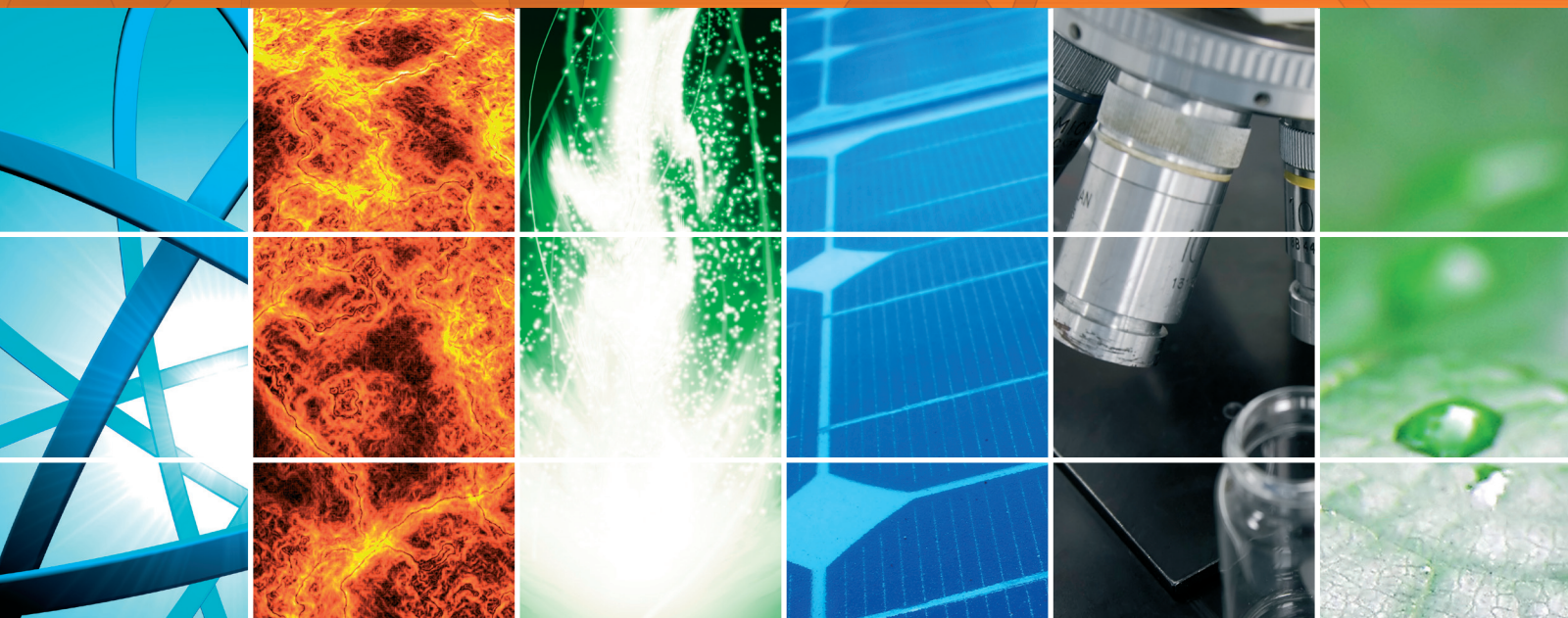


# Solar Photovoltaic Power Plants

Lead Guest Editor: Md. Rabiul Islam

Guest Editors: Wei Xu, Youguang Guo, and Ke Ma





---

# **Solar Photovoltaic Power Plants**

International Journal of Photoenergy

---

## **Solar Photovoltaic Power Plants**

Lead Guest Editor: Md. Rabiul Islam

Guest Editors: Wei Xu, Youguang Guo, and Ke Ma



---

Copyright © 2017 Hindawi. All rights reserved.

This is a special issue published in "International Journal of Photoenergy." All articles are open access articles distributed under the Creative Commons Attribution License, which permits unrestricted use, distribution, and reproduction in any medium, provided the original work is properly cited.

## Editorial Board

- M. S.A. Abdel-Mottaleb, Egypt  
Angelo Albini, Italy  
Maan Alkaisi, New Zealand  
Xavier Allonas, France  
Nicolas Alonso-Vante, France  
A. Álvarez-Gallegos, Mexico  
Wayne A. Anderson, USA  
Raja S. Ashraf, UK  
Vincenzo Augugliaro, Italy  
Detlef W. Bahnemann, Germany  
Valeriy Batoev, Russia  
Ignazio Renato Bellobono, Italy  
Raghu N. Bhattacharya, USA  
Simona Binetti, Italy  
Fabio Bisegna, Italy  
Thomas M. Brown, Italy  
Stephan Buecheler, Switzerland  
Gion Calzaferri, Switzerland  
Joaquim Carneiro, Portugal  
Yatendra S. Chaudhary, India  
V. Cimrová, Czech Republic  
Juan M. Coronado, Spain  
P. Davide Cozzoli, Italy  
Dionysios D. Dionysiou, USA  
Abderrazek Douhal, Spain  
Mahmoud M. El-Nahass, Egypt  
Polycarpos Falaras, Greece  
Chris Ferekides, USA  
Paolo Fornasiero, Italy  
Manuel Fuentes Conde, Spain  
G. Garcia-Belmonte, Spain  
E. Isabel Garcia-Lopez, Italy  
Beverley Glass, Australia  
Mohammed Ashraf Gondal, KSA  
Giulia Grancini, Switzerland  
Pierluigi Guerriero, Italy  
Michael D. Heagy, USA  
Shinya Higashimoto, Japan  
Wing-Kei Ho, Hong Kong  
J. Hüpkes, Germany  
Adel A. Ismail, Kuwait  
Chun-Sheng Jiang, USA  
Jurga Juodkazyte, Lithuania  
Shahed U. M. Khan, USA  
Sylvie Lacombe, France  
Cooper H. Langford, Canada  
Stefan Lis, Poland  
Vittorio Loddo, Italy  
Wouter Maes, Belgium  
M. Ignacio Maldonado, Spain  
Tapas Mallick, UK  
D. Mantzavinos, Greece  
Sheng Meng, China  
Santolo Meo, Italy  
Claudio Minerio, Italy  
Thomas Moehl, Switzerland  
Antoni Morawski, Poland  
F. Morlet-Savary, France  
Mohammad Muneer, India  
M. da G. P. Neves, Portugal  
T. Nyokong, South Africa  
Tsuyoshi Ochiai, Japan  
Kei Ohkubo, Japan  
Leonidas Palilis, Greece  
Leonardo Palmisano, Italy  
Ravindra K. Pandey, USA  
Thierry Pauporté, France  
Pierre Pichat, France  
Philippe Poggi, France  
Gianluca Li Puma, UK  
Tijana Rajh, USA  
F. Riganti Fulginei, Italy  
Peter Robertson, UK  
Leonardo Sandrolini, Italy  
Jinn Kong Sheu, Taiwan  
Waldemar Stampor, Poland  
Zofia Stasicka, Poland  
Elias Stathatos, Greece  
Jegadesan Subbiah, Australia  
Velumani Subramaniam, Mexico  
Mohamad-Ali Tehfe, Canada  
K. R. Justin Thomas, India  
N. V. Tkachenko, Finland  
Ahmad Umar, KSA  
Thomas Unold, Germany  
Roel van De Krol, Germany  
Mark van Der Auweraer, Belgium  
Rienk Van Grondelle, Netherlands  
W. G.J.H.M. Van Sark, Netherlands  
Xuxu Wang, China  
David Worrall, UK  
Yanfa Yan, USA  
Jiangbo Yu, USA  
Klaas Zachariasse, Germany

# Contents

---

## **Solar Photovoltaic Power Plants**

Md. Rabiul Islam, Wei Xu, Youguang Guo, and Ke Ma  
Volume 2017, Article ID 1041375, 2 pages

## **Optimal Site Selection for a Solar Power Plant in the Central Anatolian Region of Turkey**

Ozge Pinar Akkas, Mustafa Yasin Erten, Ertugrul Cam, and Nihat Inanc  
Volume 2017, Article ID 7452715, 13 pages

## **Improving the Hybrid Photovoltaic/Thermal System Performance Using Water-Cooling Technique and Zn-H<sub>2</sub>O Nanofluid**

Hashim A. Hussein, Ali H. Numan, and Ruaa A. Abdulrahman  
Volume 2017, Article ID 6919054, 14 pages

## **Observer-Based Load Frequency Control for Island Microgrid with Photovoltaic Power**

Chaoxu Mu, Weiqiang Liu, Wei Xu, and Md. Rabiul Islam  
Volume 2017, Article ID 2851436, 11 pages

## **PV-Powered CoMP-Based Green Cellular Networks with a Standby Grid Supply**

Abu Jahid, Abdullah Bin Shams, and Md. Farhad Hossain  
Volume 2017, Article ID 6189468, 14 pages

## **Synergetic Control of Grid-Connected Photovoltaic Systems**

Junjie Qian, Kaiting Li, Huaren Wu, Jianfei Yang, and Xiaohui Li  
Volume 2017, Article ID 5051489, 11 pages

## **Analysis on Photovoltaic Energy-Assisted Drying of Green Peas**

Onur Taşkın, Nazmi İzli, and Ali Vardar  
Volume 2016, Article ID 3814262, 8 pages

## **Modeling and Analysis of New Multilevel Inverter for Solar Photovoltaic Power Plant**

Xiaoqiang Guo, Ran He, and Mehdi Narimani  
Volume 2016, Article ID 4063167, 8 pages

## Editorial

# Solar Photovoltaic Power Plants

**Md. Rabiul Islam,<sup>1</sup> Wei Xu,<sup>2</sup> Youguang Guo,<sup>3</sup> and Ke Ma<sup>4</sup>**

<sup>1</sup>*Rajshahi University of Engineering and Technology, Rajshahi, Bangladesh*

<sup>2</sup>*Huazhong University of Science and Technology, Wuhan, China*

<sup>3</sup>*University of Technology Sydney, Ultimo, NWS, Australia*

<sup>4</sup>*Aalborg University, Aalborg, Denmark*

Correspondence should be addressed to Md. Rabiul Islam; [rabiulbd@hotmail.com](mailto:rabiulbd@hotmail.com)

Received 23 April 2017; Accepted 24 April 2017; Published 8 June 2017

Copyright © 2017 Md. Rabiul Islam et al. This is an open access article distributed under the Creative Commons Attribution License, which permits unrestricted use, distribution, and reproduction in any medium, provided the original work is properly cited.

In 2014, the global primary energy consumption was 12,928.4 million tons of oil equivalent which generates about 10,000 million tons of carbon during the burning of fossil fuels. The global energy crisis and environmental degradation problems have led to the rapid development of solar photovoltaic (PV) power plants to replace conventional power plants. Solar PV power plants of more than 10 MW in capacity have thereby become a reality. Future solar PV power plants will have higher power capacity. Indeed, some of them will exceed 1000 MW. Up to 2014, about 1600 installations worldwide were PV power plants larger than 4 MW. A 10 MW solar PV power plant may save about 15,000 tons of CO<sub>2</sub> emissions per annum. More than 90% of the installed capacity consists of grid-connected systems. Since multimegawatt PV power plants require large areas of land, they are usually installed in remote areas, far from cities. For power transmission, a medium voltage network is commonly used.

The power converter topology, system stability, and control of grid-connected PV power plants have attracted considerable interest in recent years, as the existing technologies are not suitable for large-scale PV power plants yet. In the last two decades, extensive research has been carried out in proposing new inverter topologies. Besides the development of inverter topologies, considerable efforts have also been directed toward the progress of maximum power point tracking algorithms and grid stability and control, due to the intermittent nature of solar energy source. In order to push this emerging technology, more research is needed to

solve two enormous challenges, that is, energy and environment by replacing conventional power plants with solar PV power plants.

We received a total of 21 manuscripts, of which 7 were selected for publication on various aspects of PV through the strict experts' peer reviews. A brief description and salient results of the papers to be published in the special issue are given below.

The paper "Modeling and Analysis of New Multilevel Inverter for Solar Photovoltaic Power Plant" by X. Guo et al. explores a novel five-level inverter for the high-voltage PV power plant applications. The model of the inverter is analyzed. With the redundant switching states, a new modulation strategy is proposed to reduce the common-mode voltage and electromagnetic interference. O. P. Akkaş et al.'s paper "Optimal Site Selection for a Solar Power Plant in the Central Anatolia Region of Turkey" describes the criteria for selecting the appropriate location of solar PV power plants by the multicriteria decision-making methods. The results are evaluated for 5 cities in the central Anatolian region of Turkey. The paper by C. Mu et al. entitled "Observer-Based Load Frequency Control for Island Microgrid with Photovoltaic Power" investigated the load frequency control of an island microgrid with PV power and electric vehicles (EVs), where the EVs can be treated as distributed energy storages. Considering the disturbances from load change and PV power, an observer-based integral sliding mode controller is designed to regulate the frequency back to the prescribed value, where the neural network

observer is used to estimate online the PV power. Research paper “Synergetic Control of Grid-Connected Photovoltaic Systems” by J. Qian presents synergetic control for the control of a grid-connected PV system. Modeling of a grid-connected PV system is described, and differential-algebra equations are obtained. Two control strategies are used in normal operation and during low-voltage ride-through of a PV system. Practical synergetic controllers with two control strategies are synthesized. The mathematical expressions are derived for computing control variables. In paper by O. Taşkın et al. entitled “Analysis on Photovoltaic Energy-Assisted Drying of Green Peas”, a PV energy-assisted industrial dryer has been tested in various weather and working conditions. A. Jahid et al.’s paper “PV-Powered CoMP-Based Green Cellular Networks with a Standby Grid Supply” proposes a novel framework for PV-powered cellular networks with a standby grid supply and essential energy management technique for achieving envisaged green networks. The proposal considers an emerging cellular network architecture employing two types of coordinated multipoint (CoMP) transmission techniques for serving the subscribers. Under the proposed framework, each base station is powered by an individual PV solar energy module having an independent storage device. The paper by H. A. Hussein et al. entitled “Improving the Hybrid Photovoltaic/Thermal System Performance Using Water-Cooling Technique and Zn-H<sub>2</sub>O Nanofluid” is devoted to an enhancement of the performance of PV panel under different operating conditions. A new design of active cooling technique is constructed which consists of a small heat exchanger and water circulating pipes placed at the PV rear surface to solve the problem of high heat stored inside the PV cells during the operation.

We hope that this issue will promote new research directions to address the undergoing challenges and technological requirements in solar PV power plants.

## **Acknowledgments**

We would like to take this opportunity to thank all the authors who are interested in publishing their articles in this special issue. Our specific thanks will be to the editorial board members of this journal; without their help and contribution, this issue will never be concluded in due course.

*Md. Rabiul Islam*  
*Wei Xu*  
*Youguang Guo*  
*Ke Ma*

## Research Article

# Optimal Site Selection for a Solar Power Plant in the Central Anatolian Region of Turkey

**Ozge Pinar Akkas, Mustafa Yasin Erten, Ertugrul Cam, and Nihat Inanc**

*Department of Electrical and Electronics Engineering, Kirikkale University, Kirikkale, Turkey*

Correspondence should be addressed to Mustafa Yasin Erten; myerten@gmail.com

Received 17 November 2016; Revised 14 February 2017; Accepted 19 March 2017; Published 7 June 2017

Academic Editor: Md. Rabiul Islam

Copyright © 2017 Ozge Pinar Akkas et al. This is an open access article distributed under the Creative Commons Attribution License, which permits unrestricted use, distribution, and reproduction in any medium, provided the original work is properly cited.

Primary energy sources are running out due to the increase in electrical energy consumption. Environmental problems caused by primary energy sources are also increasing. Using more renewable energy resources (RES) can be considered as one of the most powerful solutions to address these problems. Today, required photovoltaic power systems (PVPS) and wind energy systems (WES) are widely used as RES for addressing these problems. Because of their high costs, feasibility studies are required for locating large systems associated with these resources. In this study, various suggestions are determined about location selection, which is an important stage in the PVPS's establishment. Hence, the criteria for selecting the appropriate location are analyzed by the multicriteria decision making (MCDM) methods and the results are evaluated for 5 cities in the Central Anatolian Region of Turkey. In conclusion, it is determined which city is the most suitable place for installation of solar power plants.

## 1. Introduction

Solar energy is one of the most important RES, and it is becoming more popular day by day for many reasons such as the purification of raw materials and the reduction of dependence on foreign oil and gas. Moreover, solar energy is an inexhaustible reliable source and it is harmless to the ecological environment. The choice of the appropriate solar energy location, which is important in their setup, depends on many factors. These factors should be optimized to get more energy as well as to reduce initial investment and operation costs. These operations should be considered during the first phase of solar energy installation to locate the plant accurately. Hence, many studies are performed in the literature locating the power plants in to the most appropriate places [1–4]. Multicriteria decision making (MCDM) methods are used in the optimization of systems with multiple parameters taken into consideration at the same time [5]. For this purpose, various submethods have been used to meet the requirements.

MCDM is a subbranch of a decision process. The decision process consists of the determination of different criteria for modelling goals, evaluation of alternatives, and getting results. To evaluate the alternatives based on criteria, different methods are used, such as analytic hierarchy process (AHP), analytic network process (ANP), Technique for Order Preference by Similarity to Ideal Solution (TOPSIS), Elimination and Choice Translating Reality English (ELECTRE), The Preference Ranking Organization Method for Enrichment Evaluation (PROMETHEE), and Vise Kriterijumska Optimizacija I Kompromisno Resenje (VIKOR) [6].

There are many studies that use the MCDM methods to solve location problems in the literature. Kengpol et al. developed a decision support system for solar power plant site selection in Thailand. They applied fuzzy analytic hierarchy process (Fuzzy AHP) model for the problem [7]. Uyan worked for suitable site selection in solar farms using geographical information system (GIS) and AHP. Karapinar Region in Konya/Turkey was chosen as the study area [8]. Asakereh et al. used a Fuzzy AHP and GIS to locate the most

appropriate sites for solar energy farms in Shodirvan region in Iran [9]. ElQuoliti used AHP to determine the suitable site for solar power generation in the Western Region of Saudi Arabia. Fourteen site selection criteria are determined in the study [10]. Sozen et al. presented an approach for the location of solar plants by data envelopment analysis (DEA) and using the TOPSIS method. They applied it to 30 different cities in different regions of Turkey [11]. Lee et al. proposed a multiple-criteria decision-making model that incorporates the interpretive structural modeling (ISM), fuzzy ANP, and VIKOR to select the most suitable photovoltaic solar plant location and applied it in a case study in evaluating photovoltaic solar plant locations in Taiwan [12]. Sindhu et al. used hybrid combination of AHP and fuzzy TOPSIS to select an appropriate site in India [13].

In this study, four different MCDM methods are used to select the most suitable city among 5 cities in the Central Anatolian Region of Turkey for the establishment of solar power plant in order to get maximum power output and have minimum cost. Aksaray, Konya, Karaman, Nevşehir, and Niğde, which have the highest solar radiation, are selected for comparison. Three main criteria are defined for solar power plant location selection. These criteria rely on solar energy potential, feeder capacity, and surface slope. This study differs from other studies in terms of comparative use of all the MCDM methods. This situation has not been studied previously in the literature, especially when choosing suitable locations for PVPS. In addition, associating such a study with cities that have not been selected before is another contribution of this study. In conclusion of the study, it is observed that Karaman is determined as the most suitable city for the establishment of the solar plant station.

## 2. Problem Definition

It has become important to determine the installation location of solar energy systems that are in the foreground among the RES. Since the lifetime of such systems is a long time in 25 years, the location of a solar power plant that can obtain maximum energy is significant. Moreover, it is not possible to change the place of the system after installation because of the construction costs.

There are different criteria that can be used to determine the solar power plant location. Solar energy potential, feeder capacity of the distribution center, and surface slope are the main criteria that have been used for the selection of the solar power plant location. These main criteria have subcriteria to examine the problem in detail. Subcriteria of energy potential criterion are photovoltaic (PV) solar radiation, sunshine duration, and the total amount of energy/PV area. The feeder capacity of the distribution center has subcriteria of total capacity and available quota. Subcriteria of the power plant surface are the surface slope, ice load, and wind potential. Each subcriterion has its own weight factor for the related main criterion. In the following, the above-mentioned main criteria for the related cities will be, respectively, explained.

**2.1. Solar Energy Potential.** The location where the solar power plant will be installed is highly related with the solar energy potential of the location. The information about the solar energy potential of a location can be determined from the global radiation values ( $\text{kWh/m}^2\text{-day}$ ), sunshine duration (hours), and PV-type area energy generation ( $\text{kWh/year}$ ). In this study, these values of the cities are obtained from solar energy potential atlas (GEPA) of Directorate General of Renewable Energy in Turkey [14]. In Figures 1–5, each city's global radiation values, sunshine duration, and total amount of energy/PV area are shown.

The data in the figures are used as inputs to the proposed methods. Since the cities are in the same region and are close to each other, the suitable location of the installation cannot be estimated from the figures easily. However, they are very useful while using together with other methods. For this reason, they have been thoroughly examined.

**2.2. Feeder Capacity of the Distribution Center.** When an electric energy production facility is installed in a region, the infrastructure of the region should be examined. Therefore, the transformer capacities, the number of lines, cable sections, and so forth are considered as the parameters. In this context, the allocated capacity should also be considered. The allocated capacity of the transformer center for solar and wind energy power plants within unlicensed electricity generation is obtained with the notification of Directorate General of Turkish Electricity Transmission Corporation (TEİAŞ) [15]. The cities of Aksaray, Konya, Karaman, Nevşehir, and Niğde have a number of 10, 38, 5, 2, and 1 allocated capacities of the feeders, respectively.

**2.3. Surface Slope.** Another main criterion is surface slope. The slope of the surface where a solar power plant will be installed is usually kept below 5% [16]. The data in the study [17] is considered for the average slope data of the cities. Aksaray has 2%, Konya has 1%, Karaman has 3%, Nevşehir has 7%, and Niğde has 5% of surface slope coefficient. This suggests that the cities of Nevşehir and Niğde are problematic in terms of installation. However, these cities, which are good in terms of the amount of sunlight, have not been extracted from the analysis.

## 3. Methods

In this study, the AHP, ELECTRE, TOPSIS, and VIKOR, submethods of the MCDM, are used to decide which of the above-mentioned cities is suitable for the PVPS installation. These methods are described next for a better understanding of the simulations.

**3.1. Analytic Hierarchy Process (AHP).** AHP can be explained as the decision and the estimation method that is used for the identification of the decision hierarchy, and it gives percentage distribution of the decision points in terms of factors which affect the decision [18]. Its solution consists of 5 steps. Firstly, the decision-making problem is defined. The decision points and affecting factors are determined to define the decision-making problem. The number of decision points is denoted by  $m$ , and the

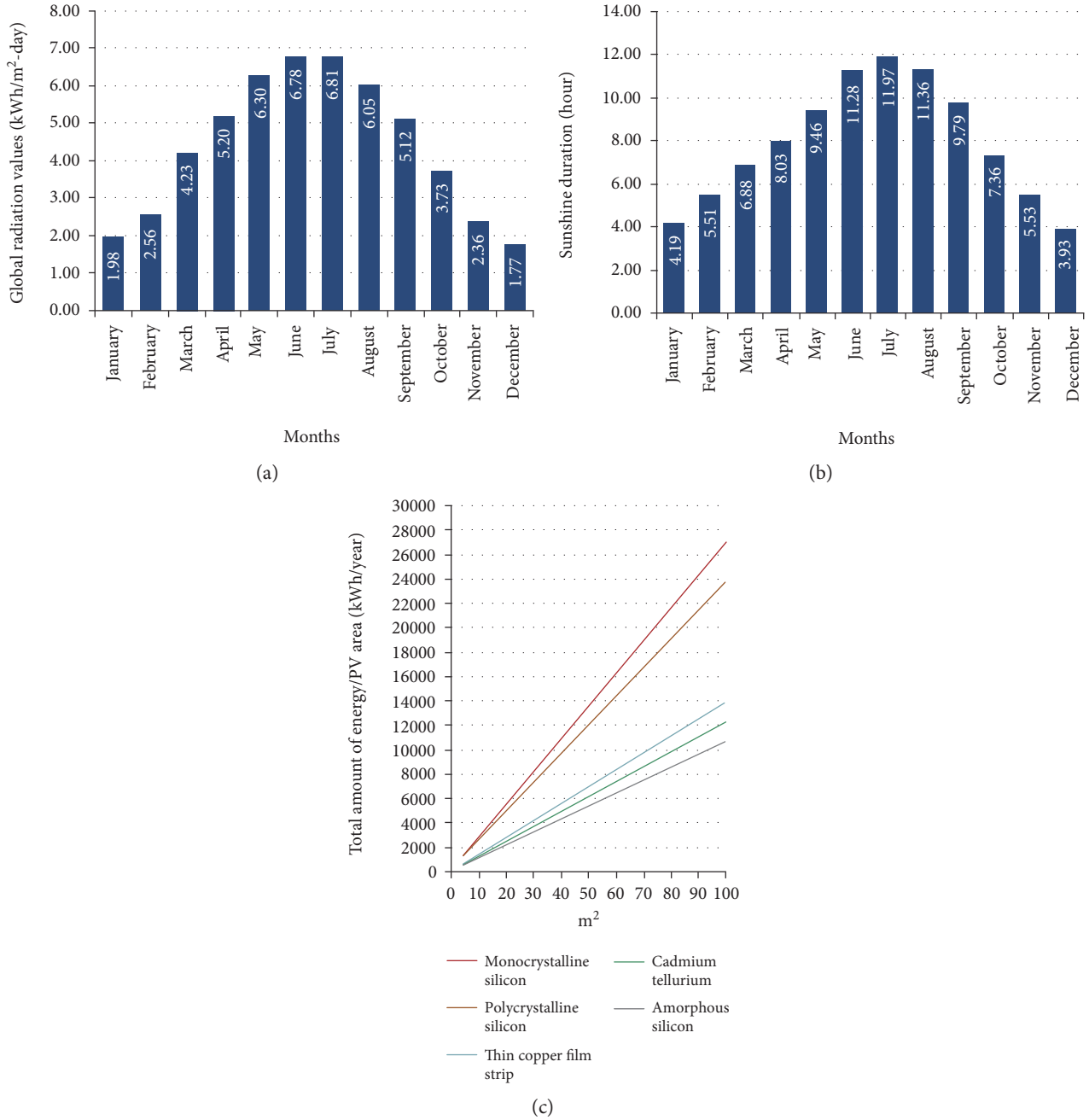


FIGURE 1: Konya province (a) global radiation values, (b) sunshine duration, and (c) total amount of energy/PV area.

number of factors affecting them is denoted by  $n$ . In the second step, comparison matrix among factors is formed. It is a square matrix of size  $n \times n$ . The components on the diagonal of the matrix take the value of "1." The resulting comparison matrix is shown in

$$A = \begin{bmatrix} a_{11} & a_{12} & \dots & a_{1n} \\ a_{21} & a_{22} & \dots & a_{2n} \\ \vdots & \vdots & \ddots & \vdots \\ a_{m1} & a_{m2} & \dots & a_{mn} \end{bmatrix}, \quad (1)$$

where  $a_{mn}$  is the element of  $m$ th row,  $n$ th column of

matrix  $A$ , and shows the intensity of importance of  $m$ th factor over  $n$ th factor. The relative importance of pairwise comparisons is measured according to a numerical scale from 1 to 9 as shown in Table 1 [19]. When factor  $m$  compared to  $n$  is assigned with the number shown in Table 1, the factor  $n$  compared to  $m$  becomes its reciprocal.

In the third step, percentage importance distribution of the factors is determined. Comparison matrix shows the importance level with respect to each factor. The column vector  $B$  that has  $k$  components is formed to determine weights or the percentage importance distribution of all factors by using column vectors that form the comparison matrix. The column vector  $B$  is shown in

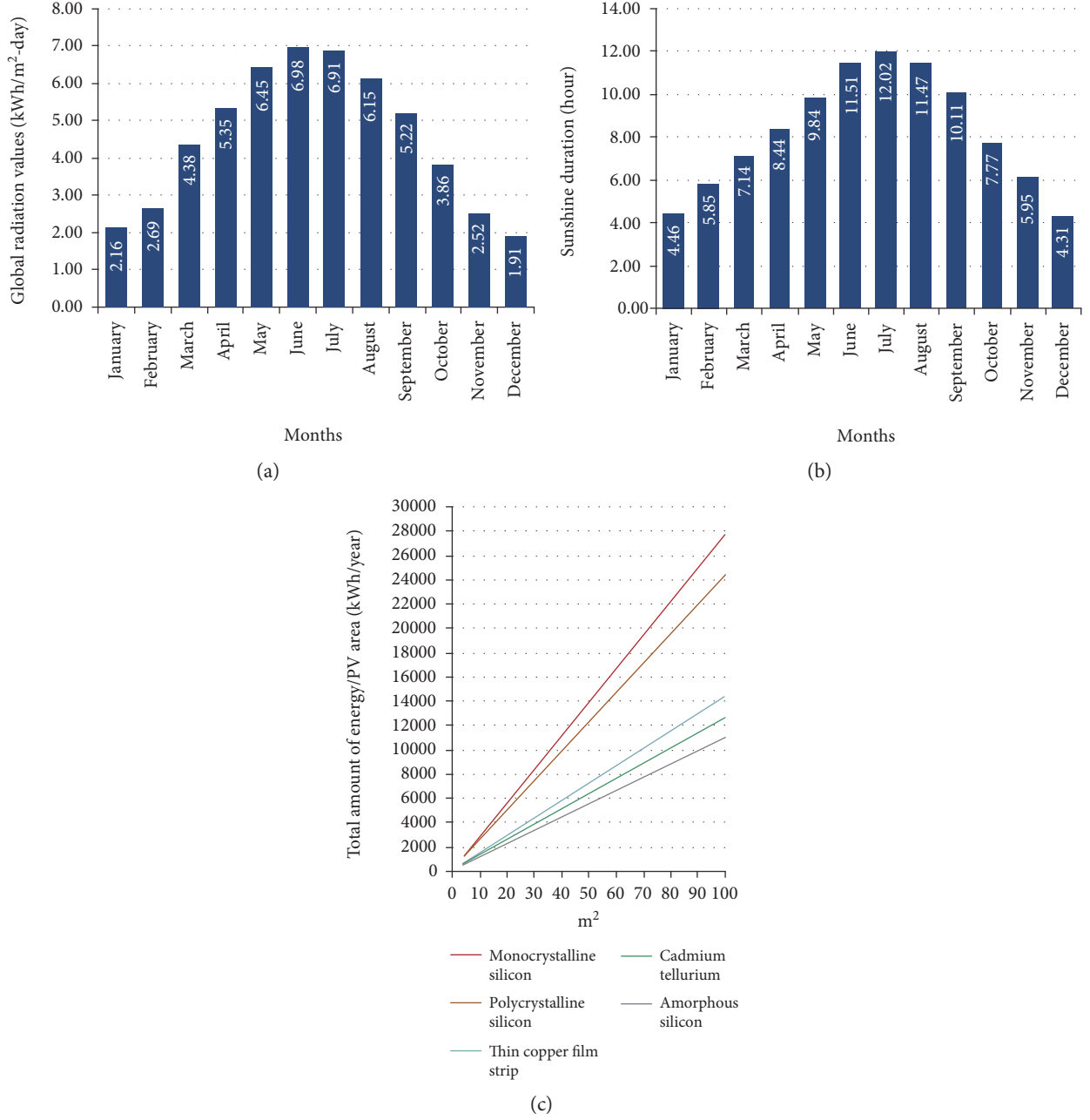


FIGURE 2: Karaman province (a) global radiation values, (b) sunshine duration, and (c) total amount of energy/PV area.

$$B_i = \begin{bmatrix} b_{11} \\ b_{21} \\ \vdots \\ b_{n1} \end{bmatrix}. \quad (2)$$

The components of the column vector  $B$  are calculated as shown in

$$b_{mn} = \frac{a_{mn}}{\sum_{m=1}^k a_{mn}}. \quad (3)$$

The matrix  $C$  is formed by combining the column vector  $B$  as shown in

$$C = \begin{bmatrix} c_{11} & c_{12} & \cdots & c_{1n} \\ c_{21} & c_{22} & \cdots & c_{2n} \\ \vdots & \vdots & \vdots & \vdots \\ c_{m1} & c_{m2} & \cdots & c_{mn} \end{bmatrix}, \quad (4)$$

where  $c_{mn}$  is the element of  $m$ th row,  $n$ th column of matrix  $C$ .

The percentage importance distribution that shows the relative importance of each factor can be obtained with the help of matrix  $C$ . The column vector  $W$  called weighting

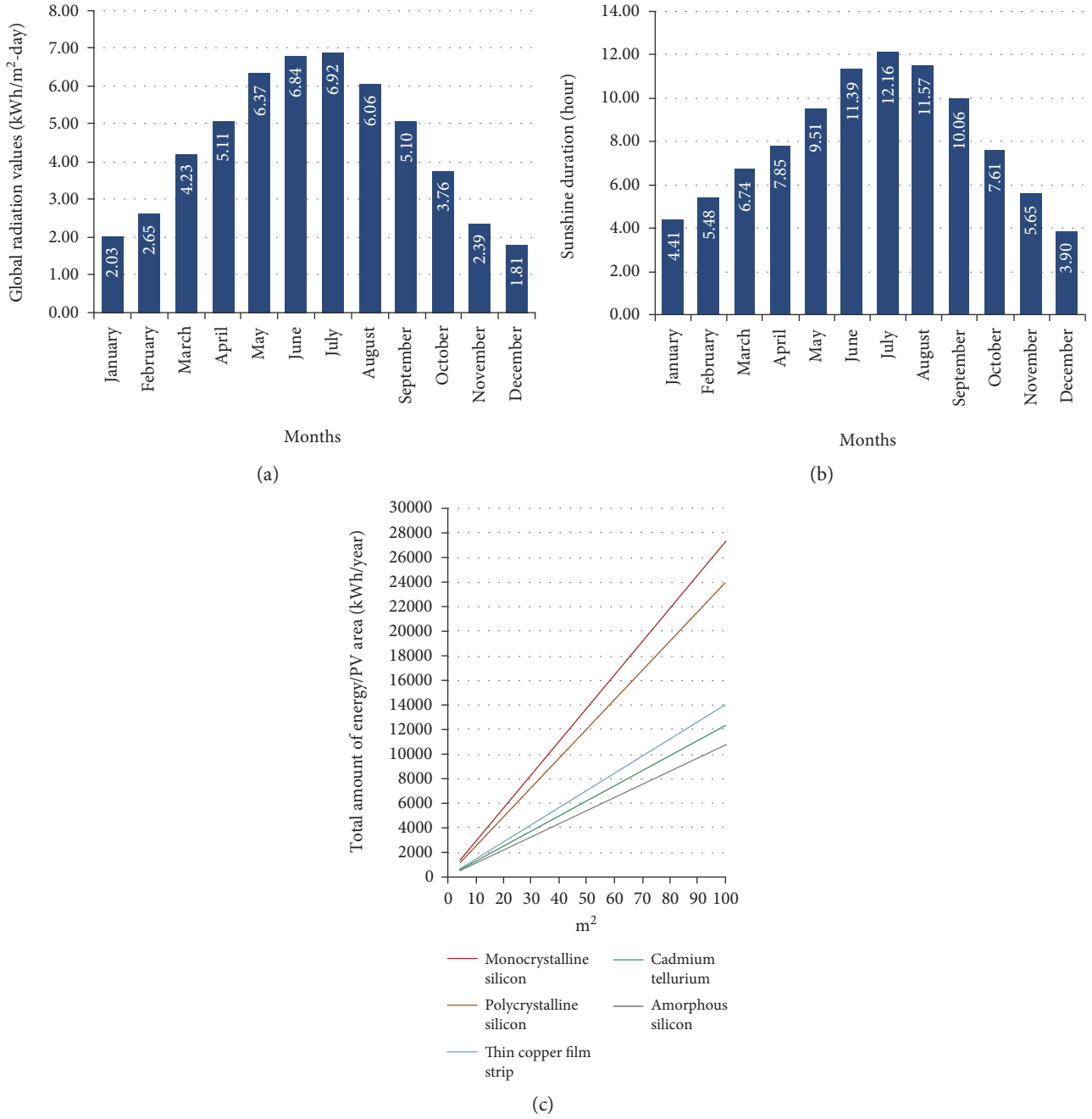


FIGURE 3: Niğde province (a) global radiation values, (b) sunshine duration, and (c) total amount of energy/PV area.

vector is obtained by taking the mean of row components of matrix  $C$ .  $W$  is shown in (5). The calculation of components of vector  $W$  is shown in (6).

$$W = \begin{bmatrix} w_1 \\ w_2 \\ \vdots \\ w_n \end{bmatrix}, \quad (5)$$

$$w_m = \frac{\sum_{n=1}^k c_{mn}}{k}. \quad (6)$$

In the fourth step, consistency of factor comparison is measured. Consistency ratio (CR) determines whether the comparisons that are made by AHP method are true or not. Firstly, column vector  $D$  is obtained by multiplying comparison matrix  $A$  with weighting vector  $W$  as shown in

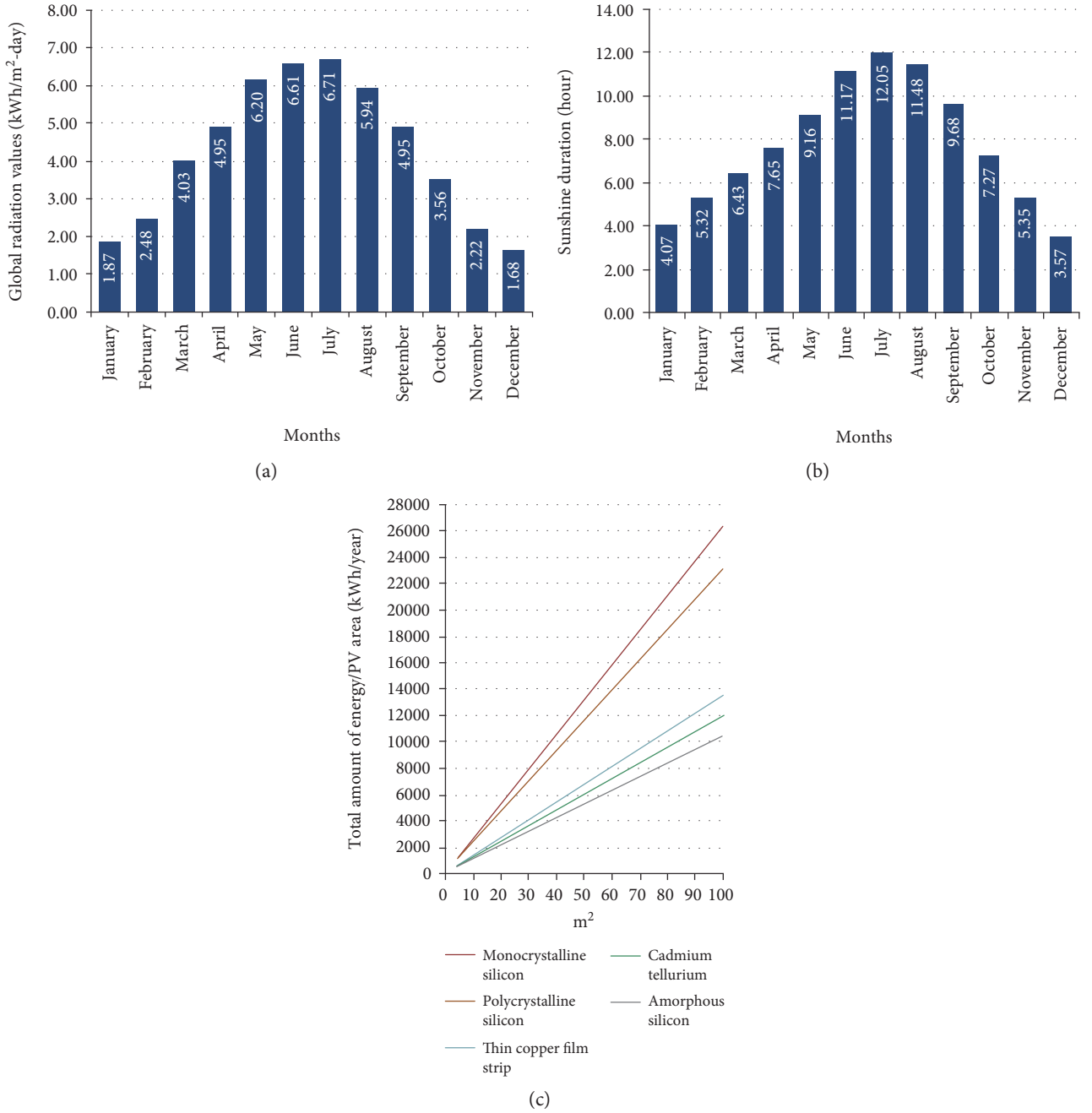


FIGURE 4: Nevşehir province (a) global radiation values, (b) sunshine duration, and (c) total amount of energy/PV area.

$$D = \begin{bmatrix} a_{11} & a_{12} & \dots & a_{1n} \\ a_{21} & a_{22} & \dots & a_{2n} \\ \vdots & \vdots & \vdots & \vdots \\ a_{m1} & a_{m2} & \dots & a_{mn} \end{bmatrix} x \begin{bmatrix} w_1 \\ w_2 \\ \vdots \\ w_n \end{bmatrix}. \quad (7)$$

Main value related to each evaluation factor (EF) is obtained by dividing column vector  $D$  to the corresponding elements of column vector  $W$  as shown in

$$EF_m = \frac{d_m}{w_m} \quad (m = 1, 2, \dots, k). \quad (8)$$

Mean value related to the comparison ( $\lambda$ ) is obtained by taking the mean of EF elements as shown in

$$\lambda = \frac{\sum_{i=m}^k EF_m}{k}. \quad (9)$$

Then, consistency index (CI) and the (CR) are calculated as shown in (10) and (11).

The value of CR must be smaller than 0.10 to be consistent with comparison matrix [20].

Random index (RI) in (11) takes different values by the number of criteria. The values of RI according to  $n$ , which is the number of criteria, are shown in Table 2.

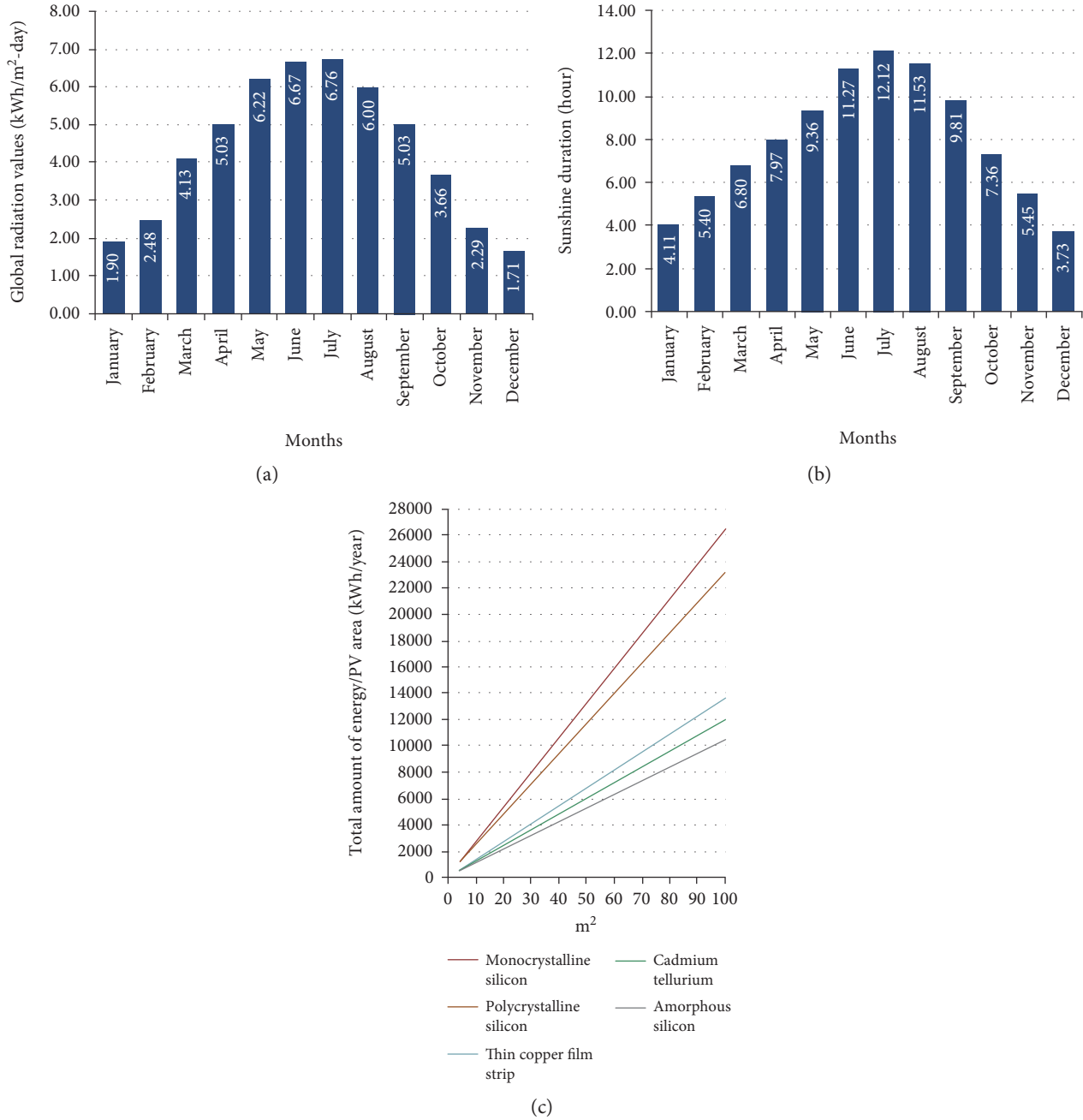


FIGURE 5: Aksaray province (a) global radiation values, (b) sunshine duration, and (c) total amount of energy/PV area.

In this study, the value of RI is taken as 0.58 from the table since there are 3 criteria.

$$CI = \frac{\lambda - k}{k - 1}, \tag{10}$$

$$CR = \frac{CI}{RI}. \tag{11}$$

In the final step, percentage importance distribution (PID) at  $m$  decision points is found for each factor. In other words, the comparisons and matrix operations are repeated  $k$  times. However, the size of the comparison matrix that will be used as the decision points of each factor will be  $m \times m$ .

After each comparison operation, column vector  $S$  that shows percentage distribution and has a size of  $m \times 1$  is obtained. The column vector  $S$  is shown in

$$S_m = \begin{bmatrix} s_{11} \\ s_{21} \\ \vdots \\ s_{m1} \end{bmatrix}. \tag{12}$$

The decision matrix  $K$  is formed with  $m \times n$  size, and it consists of  $n$  column vector  $S$  which has the size of  $m \times 1$ . It is shown in

TABLE 1: Rating scale of AHP method.

Intensity of importance	Definition	Explanation
1	Equal importance	Two factors contribute equally to the objective.
3	More important	Experience and judgement slightly favour one over the other.
5	Much more important	Experience and judgement strongly favour one over the other.
7	Very much more important	Experience and judgement very strongly favour one over the other.
9	Absolutely more important	The evidence favouring one over the other is of the highest possible validity.
2, 4, 6, 8	Intermediate values	When compromise is needed.

TABLE 2: The values of RI.

$k$	RI	$k$	RI
1	0	6	1.24
2	0	7	1.32
3	0.58	8	1.41
4	0.90	9	1.45
5	1.12	10	1.49

$$K = \begin{bmatrix} s_{11} & s_{12} & \cdots & s_{1n} \\ s_{21} & s_{22} & \cdots & s_{2n} \\ \vdots & \vdots & \vdots & \vdots \\ s_{m1} & s_{m2} & \cdots & s_{mn} \end{bmatrix}. \quad (13)$$

As a result, the column vector  $L$  is obtained by multiplying the decision matrix with column vector  $W$  (weighting vector) as shown in (14). The column vector  $L$  gives the percentage distribution of decision points, and the sum of its elements is 1.

$$L = \begin{bmatrix} s_{11} & s_{12} & \cdots & s_{1n} \\ s_{21} & s_{22} & \cdots & s_{2n} \\ \vdots & \vdots & \vdots & \vdots \\ s_{m1} & s_{m2} & \cdots & s_{mn} \end{bmatrix} \times \begin{bmatrix} w_1 \\ w_2 \\ \vdots \\ w_n \end{bmatrix} = \begin{bmatrix} l_{11} \\ l_{21} \\ \vdots \\ l_{m1} \end{bmatrix}. \quad (14)$$

**3.2. Elimination and Choice Translating Reality English (ELECTRE).** The method depends on dual superiority comparisons among the decision points for each evaluation factor. This method basically consists of 8 steps [21]. Firstly, the decision matrix  $A$  is formed. There are decision points and evaluation factors in rows and columns of the decision matrix. The matrix  $A$  is the initial matrix that is formed by the decision maker. The number of decision points and the number of the evaluation factors are represented by  $m$  and  $n$  in the  $A_{mn}$  matrix. The resulting decision matrix is shown in

$$A_{mn} = \begin{bmatrix} a_{11} & a_{12} & \cdots & a_{1n} \\ a_{21} & a_{22} & \cdots & a_{2n} \\ \vdots & \vdots & \vdots & \vdots \\ a_{m1} & a_{m2} & \cdots & a_{mn} \end{bmatrix}. \quad (15)$$

In the second step, standard decision matrix,  $X$ , is formed. It is shown in

$$X_{mn} = \begin{bmatrix} x_{11} & x_{12} & \cdots & x_{1n} \\ x_{21} & x_{22} & \cdots & x_{2n} \\ \vdots & \vdots & \vdots & \vdots \\ x_{m1} & x_{m2} & \cdots & x_{mn} \end{bmatrix}. \quad (16)$$

$X$  is formed by the help of matrix  $A$ . The elements of matrix  $X$  are calculated as shown in

$$x_{mn} = \frac{a_{mn}}{\sqrt{\sum_{k=1}^m a_{kn}^2}}, \quad (17)$$

where  $m$  is the number of the decision points,  $n$  is the number of the columns, and  $a$  is the element of matrix  $A$ .

In the third step, the weighted standard decision matrix,  $Y$ , is formed. The matrix  $Y$  is used to reflect importance differences of the criteria to the solution. The matrix  $Y$  is obtained by multiplying matrix  $X$  with a weighting vector  $w_i$  as shown in

$$Y_{mn} = \begin{bmatrix} w_1 x_{11} & w_2 x_{12} & \cdots & w_n x_{1n} \\ w_1 x_{21} & w_2 x_{22} & \cdots & w_n x_{2n} \\ \vdots & \vdots & \vdots & \vdots \\ w_1 x_{m1} & w_2 x_{m2} & \cdots & w_n x_{mn} \end{bmatrix}. \quad (18)$$

In the fourth step, consistency ( $C_{kl}$ ) and inconsistency ( $D_{kl}$ ) sets are determined. Matrix  $Y$  is used to determine the consistency sets. The decision points are evaluated in terms of the criteria. Equation (19) is used in this evaluation process. Every consistency set corresponds to one inconsistency set in this method. Inconsistency set consists of the elements that are not in the consistency set.

$$C_{kl} = \{n, y_{kn} \geq y_{ln}\}. \quad (19)$$

In the fifth step, consistency ( $C$ ) and inconsistency ( $D$ ) matrices are formed with the help of the consistency and inconsistency sets. The elements of the consistency matrix are found with (20), and the elements of the inconsistency matrix are found with (21).

$$c_{kl} = \sum_{n \in C_{kl}} w_n, \quad (20)$$

$$d_{kl} = \frac{\max_{n \in D_{kl}} |y_{kn} - y_{ln}|}{\max_n |y_{kn} - y_{ln}|}. \quad (21)$$

The matrix  $C$  is obtained with (20) as shown in (22), and the matrix  $D$  is obtained with (21) as shown in (23).

$$C = \begin{bmatrix} - & c_{12} & c_{13} & \cdots & c_{1m} \\ c_{21} & - & c_{23} & \cdots & c_{2m} \\ \vdots & \vdots & \vdots & \vdots & \vdots \\ c_{m1} & c_{m2} & c_{m3} & \cdots & - \end{bmatrix}, \quad (22)$$

$$D = \begin{bmatrix} - & d_{12} & d_{13} & \cdots & d_{1m} \\ d_{21} & - & d_{23} & \cdots & d_{2m} \\ \vdots & \vdots & \vdots & \vdots & \vdots \\ d_{m1} & d_{m2} & d_{m3} & \cdots & - \end{bmatrix}. \quad (23)$$

In the sixth step, consistency superiority ( $F$ ) and inconsistency superiority ( $G$ ) matrices are formed.

The matrix  $F$  is in the size of  $m \times m$ , and the elements of the matrix  $F$  are obtained by the comparison of a consistency threshold value ( $\underline{c}$ ) and the elements of consistency matrix ( $c_{kl}$ ). Consistency threshold value is found with

$$\underline{c} = \frac{1}{m(m-1)} \sum_{k=1}^m \sum_{l=1}^m c_{kl}. \quad (24)$$

The elements of the matrix  $F$  ( $f_{kl}$ ) take a value of 1 or 0, and there are no values on the diagonal of the matrix because the diagonal elements show the same decision point. If  $c_{kl} \geq \underline{c} \Rightarrow f_{kl} = 1$ , and if  $c_{kl} < \underline{c} \Rightarrow f_{kl} = 0$ .

The matrix  $G$  is in the size of  $m \times m$ , and it is formed in the same manner as matrix  $F$ . Inconsistency threshold value ( $\underline{d}$ ) is found with

$$\underline{d} = \frac{1}{m(m-1)} \sum_{k=1}^m \sum_{l=1}^m d_{kl}. \quad (25)$$

The elements of the matrix  $G$  ( $g_{kl}$ ) take a value of 1 or 0, and there are no values on the diagonal of the matrix because the diagonal elements show the same decision point. If  $d_{kl} < \underline{d} \Rightarrow g_{kl} = 1$ , and if  $d_{kl} \geq \underline{d} \Rightarrow g_{kl} = 0$ .

In the seventh step, total dominance matrix ( $E$ ) is formed.  $E$  is obtained with the multiplication of matrices  $F$  and  $K$  and consists of 1's and 0's. Finally, the order of importance of the decision points is determined.

**3.3. Technique for Order Preference by Similarity to Ideal Solution (TOPSIS).** In the first step of this method, the decision matrix  $A$  is formed. There are decision points in the rows of the decision matrix and evaluation factors at the columns of the decision matrix. The matrix  $A$  is an initial matrix that is formed by the decision maker [22]. The resulting decision matrix is shown in

$$A_{mn} = \begin{bmatrix} a_{11} & a_{12} & \cdots & a_{1n} \\ a_{21} & a_{22} & \cdots & a_{2n} \\ \vdots & \vdots & \vdots & \vdots \\ a_{m1} & a_{m2} & \cdots & a_{mn} \end{bmatrix}. \quad (26)$$

In the second step, standard decision matrix  $R$  is formed. The matrix  $R$  is shown in

$$R_{mn} = \begin{bmatrix} r_{11} & r_{12} & \cdots & r_{1n} \\ r_{21} & r_{22} & \cdots & r_{2n} \\ \vdots & \vdots & \vdots & \vdots \\ r_{m1} & r_{m2} & \cdots & r_{mn} \end{bmatrix}. \quad (27)$$

The elements of the matrix  $R$  are calculated with the help of the matrix  $A$  as shown in

$$r_{mn} = \frac{a_{mn}}{\sqrt{\sum_{k=1}^m a_{kn}^2}}. \quad (28)$$

In the third step, standard weighted decision matrix  $V$  is formed. Firstly, weight values ( $w_n$ ) related to evaluation factors are determined. Then, elements for each column in the matrix  $R$  are multiplied with related  $w_n$  value. The matrix  $V$  is shown in

$$V_{mn} = \begin{bmatrix} w_1 r_{11} & w_2 r_{12} & \cdots & w_n r_{1n} \\ w_1 r_{21} & w_2 r_{22} & \cdots & w_n r_{2n} \\ \vdots & \vdots & \vdots & \vdots \\ w_1 r_{m1} & w_2 r_{m2} & \cdots & w_n r_{mn} \end{bmatrix}. \quad (29)$$

In the fourth step, ideal ( $A^*$ ) and nonideal ( $A^-$ ) solutions are formed. The biggest value of the weighted evaluation factors of matrix  $V$  is chosen to form an ideal solution set. Equation (30) shows the finding of the ideal solution set.

$$A^* = \left\{ \left( \max_m v_{mn} \mid n \in N \right), \left( \min_m v_{mn} \mid n \in N' \right) \right\}. \quad (30)$$

The smallest value of weighted evaluation factors of matrix  $V$  is chosen to form a nonideal solution set. Equation (31) shows the finding of the nonideal solution set.

$$A^- = \left\{ \left( \min_m v_{mn} \mid n \in N \right), \left( \max_m v_{mn} \mid n \in N' \right) \right\}. \quad (31)$$

In the fifth step, discrimination measurements are calculated. The deviation values related to the decision points are calculated with the help of Euclidean distance approach. Ideal discrimination ( $S_m^*$ ) and nonideal discrimination ( $S_m^-$ ) measurement values are found with

$$S_m^* = \sqrt{\sum_{n=1}^n (v_{mn} - v_n^*)^2}, \quad (32)$$

$$S_m^- = \sqrt{\sum_{n=1}^n (v_{mn} - v_n^-)^2}. \quad (33)$$

In the final step, the relative proximity of the ideal solution is calculated. The ideal and nonideal discrimination values are used to calculate relative proximity of the ideal solution for each decision point. The calculation is shown in

$$C_m^* = \frac{S_m^-}{S_m^- + S_m^*}. \quad (34)$$

In (34), the value of  $C_m^*$  is between 0 and 1 as shown in

TABLE 3: Comparison matrix for solar energy potential.

Solar energy potential	Aksaray	Konya	Karaman	Nevşehir	Niğde
Aksaray	1	1/3	1/7	3	1/5
Konya	3	1	1/5	5	1/3
Karaman	7	5	1	9	3
Nevşehir	1/3	1/5	1/9	1	1/7
Niğde	5	3	1/3	7	1

TABLE 4: Comparison matrix for maximum capacity that can be allocated.

Maximum capacity that can be allocated	Aksaray	Konya	Karaman	Nevşehir	Niğde
Aksaray	1	1/3	3	5	8
Konya	3	1	5	7	9
Karaman	1/3	1/5	1	2	5
Nevşehir	1/5	1/7	1/2	1	3
Niğde	1/8	1/9	1/5	1/3	1

$$0 \leq C_m^* \leq 1. \tag{35}$$

If  $C_m^*$  equals 1, it shows the absolute proximity of related decision point to the ideal solution, and if  $C_m^*$  equals 0, it shows the absolute proximity of the related decision point to the nonideal solution.

3.4. *Vise Kriterijumska Optimizacija I Kompromisno Resenje (VIKOR)*. This method solves the problems by calculating the best and the worst values of all the criteria functions. The best ( $f_m^*$ ) and the worst ( $f_m^-$ ) values are found with [22, 23]

$$f_m^* = \max f_{mn}, \tag{36}$$

$$f_m^- = \min f_{mn}, \tag{37}$$

where  $m$  represents criteria and  $n$  represents alternatives.

Then, the values of  $S_n$  and  $R_n$  are calculated with [22, 23]

$$S_n = \sum_{m=1}^n \frac{w_m (f_m^* - f_{mn})}{f_m^* - f_m^-}, \tag{38}$$

$$R_n = \max \left[ \frac{w_m (f_m^* - f_{mn})}{f_m^* - f_m^-} \right], \tag{39}$$

where  $w_m$  represents the weight of the  $m$ th criteria.

After that, the value of  $Q_n$  that represents the maximum group benefit is found with (40) for each alternative.

$$Q_n = \frac{\nu(S_n - S^*)}{S^- - S^*} + \frac{(1 - \nu)(R_n - R^*)}{R^- - R^*}, \tag{40}$$

where  $S^* = \min^n S_n$ ,  $S^- = \max^n S_n$ ,  $R^* = \min^n R_n$ , and  $R^- = \max^n R_n$ .  $\nu$  refers to the weight for the strategy that ensures maximum group utility, and  $(1 - \nu)$  refers to the weight of the minimum regret in dissent. The value of  $\nu$

TABLE 5: Comparison matrix for surface slope.

	Aksaray	Konya	Karaman	Nevşehir	Niğde
Aksaray	1	1/3	2	8	5
Konya	3	1	5	9	7
Karaman	1/2	1/5	1	6	3
Nevşehir	1/8	1/9	1/6	1	1/3
Niğde	1/5	1/7	1/3	3	1

TABLE 6: Decision matrix.

	Solar energy potential	Surface slope	Capacity
Aksaray	4	8	8
Konya	6	10	10
Karaman	10	6	6
Nevşehir	2	2	4
Niğde	8	4	2

TABLE 7: Matrix E.

	Aksaray	Konya	Karaman	Nevşehir	Niğde
Aksaray	—	0	0	1	0
Konya	1	—	0	1	0
Karaman	1	1	—	1	1
Nevşehir	0	0	0	—	0
Niğde	1	0	0	1	—

TABLE 8: Proximity values based on ideal solution.

	$C^*$
Aksaray	0.34
Konya	0.56
Karaman	0.83
Nevşehir	0.07
Niğde	0.62

changes between 0 and 1. Generally, the value of  $\nu$  is taken as 0.5.

Finally, the calculated values of  $S_n$ ,  $R_n$ , and  $Q_n$  are ranked in a decreasing order.  $Q_n$  with the smallest value is expressed as the best option among alternatives.

## 4. Simulation and Results

In this study, a simulation is implemented by using the MATLAB program to establish the location of the solar power plants for the suggested cities with the help of the methods that are described next. The results obtained from the methods according to the problem definition have been explained in this section.

4.1. *AHP Results*. In this method, the matrices to be found for the three main criteria described in the previous chapters will

TABLE 9: Values of  $S_n$ ,  $R_n$ ,  $Q_n$ , and decreasing order.

	$S_n$	Order of $S_n$	$R_n$	Order of $R_n$	$Q_n$	Order of $Q_n$
Aksaray	0.575	4	0.4875	4	0.6086	4
Konya	0.325	2	0.325	3	0.2939	2
Karaman	0.175	1	0.115	1	0	1
Nevşehir	0.9425	5	0.65	5	1	5
Niğde	0.4825	3	0.23	2	0.3077	3

TABLE 10: Results with AHP, ELECTRE, TOPSIS, and VIKOR methods.

Method	1	2	3	4	5
AHP	Karaman	Konya	Niğde	Aksaray	Nevşehir
ELECTRE	Karaman	Konya/Niğde	Konya/Niğde	Aksaray	Nevşehir
TOPSIS	Karaman	Niğde	Konya	Aksaray	Nevşehir
VIKOR	Karaman	Konya	Niğde	Aksaray	Nevşehir

be shown in a tabular form. These matrices are the comparative matrices of the solar energy potential, the allocated capacity, and the surface slope. The data to be used for this purpose is taken from the study in [14]. Since the rows and columns have the same cities, the diagonal values of Table 3 are 1. However, the other elements of the matrices are composed of different values found by using the AHP equations. These values show which city is superior to the others.

The comparison matrix that is formed by comparing the cities is shown in Table 3. Here, the row side shows the main variable. (This will also be applied to all other tabs throughout the article.) So, the order of importance will also be extracted according to the row. For example, Karaman has more solar energy potential than Aksaray, because when Karaman is written in a row and Aksaray is written in a column, the intersection point of the two cities in the table is determined as 7. However, for the opposite case, the element at the intersection point is 1/7. When the whole table is examined in this way, it can be seen that Karaman has the greatest solar potential. This city is followed by Niğde, Konya, Aksaray, and Nevşehir, respectively.

After that, the CR value is calculated with the help of (11). This value is 0.054 for the solar energy potential criterion. A CR value that is less than 0.10 indicates consistency.

Similar to the above procedures, maximum allocated capacity values are found. The data of the maximum capacity are taken from the study in [15]. According to the data, Konya has the highest maximum capacity that can be allocated. Aksaray, Karaman, Nevşehir, and Niğde follow Konya, respectively. The comparison matrix among alternatives for the maximum allocated capacity criterion is given in Table 4.

After that, the CR value is calculated with the help of 11. This value is 0.042 for the maximum allocated capacity criterion. Since this value is also smaller than 0.10, CR of the maximum allocated capacity value is consistent.

With the same repeated operations, the surface gradient matrix is also constructed using the data from the study [17]. The generated matrix, as Table 5, is given next. According to the table, Konya has the most suitable city

and is followed by Aksaray, Karaman, Niğde, and Nevşehir, respectively.

The value of the CR for the surface slope criteria is calculated with (11) and found as 0.047. It is less than 0.10, and it shows the consistency.

Equation (14) is used to combine all the results. As a result, it is found where the PVPS should be installed. Accordingly, installation should be done in the cities of Karaman, Konya, Niğde, Aksaray, and Nevşehir, respectively. The percentage values for this situation are listed as 37%, 26%, 18%, 14%, and 5%, respectively.

**4.2. ELECTRE Results.** In this method, the decision matrix is formed as mentioned in (15). The decision points (Aksaray, Konya, Karaman, Nevşehir, and Niğde) are put in the rows, and evaluation factors (solar energy potential, surface slope, and capacity) are put in the columns of the decision matrix. While forming the decision matrix, 2, 4, 6, 8, and 10 points are given to alternatives by considering their importance. For example, Karaman has the biggest point 10 due to having the highest solar energy potential. This city is followed by Niğde, Konya, Aksaray, and Nevşehir with 8, 6, 4, and 2 points, respectively, for the solar energy potential criterion. The decision matrix is shown in Table 6.

After forming the decision matrix, total dominance matrix called matrix  $E$  is found by doing solution steps of ELECTRE method that are shown in (16)–(25). The matrix  $E$  is shown in Table 7.

When results in Table 7 are examined, the order of importance of decision points is determined by looking at the values of 1. It is seen that Karaman is more dominant than all of the other cities. Konya and Niğde are more dominant than Aksaray and Nevşehir. It is observed that Konya and Niğde are not superior to each other. Therefore, the second choice can be Konya or Niğde. Aksaray is more dominant than Nevşehir. Nevşehir is not more dominant than any of the other cities. When the results are combined, the order of priority for the solution is found as Karaman > Konya = Niğde > Aksaray > Nevşehir.

**4.3. TOPSIS Results.** In this method, decision matrix is needed to obtain proximity values. Therefore, the decision matrix in Table 6 that is used in the solution with ELECTRE method is taken. After that, the solution steps of the TOPSIS method that are shown in (27)–(35) are performed. The results helping us to find the ideal decision points are obtained with calculating proximity values based on the ideal solution. They are shown in Table 8.

The alternative, which has  $C^*$  value closest to 1, is the ideal solution as mentioned in (35). According to the results in Table 8, Karaman which has the biggest  $C^*$  is the ideal city for the problem solution. This city is followed by Niğde, Konya, Aksaray, and Nevşehir, respectively.

**4.4. VIKOR Results.** In this method, the decision matrix in Table 6 that is used in the solution with the ELECTRE method is taken again. After that, the solution steps of VIKOR method that are shown in (36)–(40) are performed. The values of  $S_n$ ,  $R_n$ , and  $Q_n$  are calculated. These values are ordered decreasingly. The results are shown in Table 9.

According to the VIKOR method,  $Q_n$  with the smallest value is expressed as the best option among the alternatives as mentioned in the solution steps of this method. When Table 9 is examined, Karaman has the smallest value of  $Q_n$ . Therefore, Karaman is the first choice among the alternatives. This city is followed by Konya, Niğde, Aksaray, and Nevşehir, respectively, for solar power plant installation by looking at the value of  $Q_n$ .

**4.5. Comparative Results of All Methods.** Table 10 is obtained by combining the results of the 4 MCDM methods used above. Thus, it is aimed that all the results could be seen together.

## 5. Conclusions

In this study, deciding on the most suitable location for a solar power plant installation is investigated. The results are obtained with the AHP, ELECTRE, TOPSIS, and VIKOR methods from MCDM submethods. The cities of Aksaray, Konya, Karaman, Nevşehir, and Niğde from the Central Anatolian Region of Turkey are selected for the study. The solar energy potential, the allocated feeder connection capacity, and the surface slope are chosen as criteria for the study. According to the chosen criteria, it has shown that Karaman has been identified as the most suitable city for solar power plant installation for all of the methods. Moreover, current practical works are also in the line with our study's results. Therefore, this is a verification of the methods used in this study and they can be proposed for a solar power plant location selection.

## Conflicts of Interest

The authors declare that there is no conflict of interests regarding the publication of this paper.

## References

- [1] H. M. Kandirmaz, K. Kaba, and M. Avci, "Estimation of monthly sunshine duration in Turkey using artificial neural networks," *International Journal of Photoenergy*, vol. 2014, Article ID 680596, 9 pages, 2014.
- [2] T. Khatib, A. Mohamed, K. Sopian, and M. Mahmoud, "Assessment of artificial neural networks for hourly solar radiation prediction," *International Journal of Photoenergy*, vol. 2012, Article ID 946890, 7 pages, 2012.
- [3] S. Daliendo, A. Chouder, P. Guerriero et al., "Monitoring diagnosis, and power forecasting for photovoltaic fields: a review," *International Journal of Photoenergy*, vol. 2017, Article ID 1356851, 13 pages, 2017.
- [4] S. Kittisontirak, A. Bupi, P. Chinnavornrungrsee, K. Sriprapha, P. Thajchayapong, and W. Titiroongruang, "An improved PV output forecasting model by using weight function: a case study in Cambodia," *International Journal of Photoenergy*, vol. 2016, Article ID 2616750, 10 pages, 2016.
- [5] Ö. Aydın, S. Öznehir, and E. Akçali, "Optimal hospital location selection by analytical hierarchical process," *Suleyman Demirel University the Journal of Faculty Economics and Administrative Sciences*, vol. 14, no. 2, pp. 69–86, 2009.
- [6] Y. Çınar, *Çok Nitelikli Karar Verme ve Bankaların Mali Performansının Değerlendirilmesi Örneği*, [M.S. Thesis], Ankara Üniversitesi, Sosyal Bilimler Enstitüsü, 2004.
- [7] A. Kengpol, P. Rontlaong, and M. Tuominen, "Design of a decision support system for site selection using fuzzy AHP: a case study of solar power plant in north eastern parts of Thailand," in *2012 Proceedings of PICMET '12: Technology Management for Emerging Technologies*, pp. 734–743, 2012.
- [8] M. Uyan, "GIS-based solar farms site selection using analytic hierarchy process (AHP) in Karapınar region, Konya/Turkey," *Renewable and Sustainable Energy Reviews*, vol. 28, pp. 11–17, 2013.
- [9] A. Asakereh, M. Omid, R. Alimardani, and F. Sarmadian, "Developing a GIS-based fuzzy AHP model for selecting solar energy sites in Shodirwan region in Iran," *International Journal of Advanced Science and Technology*, vol. 68, pp. 37–48, 2014.
- [10] S. A. H. ElQuoliti, "An analytic hierarchy process to evaluate candidate locations for solar energy stations: Kingdom of Saudi Arabia as a case study," *International Journal on Power Engineering and Energy (IJPEE)*, vol. 6, no. 3, 2015.
- [11] A. Sozen, A. Mirzapour, and M. T. Çakır, "Selection of the best location for solar plants in Turkey," *Journal of Energy in Southern Africa*, vol. 26, no. 4, 2015.
- [12] A. H. I. Lee, H. Kang, and Y. Liou, "A hybrid multiple-criteria decision-making approach for photovoltaic solar plant location selection," *Sustainability*, vol. 9, no. 2, p. 184, 2017.
- [13] S. Sindhu, V. Nehra, and S. Luthra, "Investigation of feasibility study of solar farms deployment using hybrid AHP-TOPSIS analysis: case study of India," *Renewable and Sustainable Energy Reviews*, vol. 73, pp. 496–511, 2017.
- [14] Directorate General of renewable energy, October 2016, <http://www.eie.gov.tr/MyCalculator/Default.aspx>.
- [15] Energy institute, October 2016, <http://enerjienstitusu.com/2016/03/21/teias-ges-res-trafo-merkezi-kapasiteleri-mart-2016/>.
- [16] D. Turney and V. Fthenakis, "Environmental impacts from the installation and operation of large-scale solar power plants,"

- Renewable and Sustainable Energy Reviews*, vol. 15, no. 6, pp. 3261–3270, 2011.
- [17] M. Elibüyük and E. Yılmaz, “Altitude steps and slope groups of Turkey in comparison with geographical regions and sub-regions,” *Coğrafi Bilimler Dergisi*, vol. 8, no. 1, pp. 27–55, 2010.
- [18] T. L. Saaty, *The Analytic Hierarchy Process*, McGraw Hill, New York, 1980.
- [19] G. Coyle, “The analytic hierarchy process (AHP),” *Practical Strategy, Open Access Material, AHP*, 2014.
- [20] F. Dweiri, S. Kumar, S. A. Khan, and V. Jain, “Designing an integrated AHP based decision support system for supplier selection in automotive industry,” *Expert Systems with Applications*, vol. 62, pp. 273–283, 2016.
- [21] F. Urfaloğlu and T. Genç, “Comparison of the economic performance between Turkey and the European Union members with multi criteria decision making methods,” *Marmara University Journal of E.A.S.*, vol. 35, no. 2, pp. 329–360, 2013.
- [22] İ. Ertuğrul and A. Özçil, “Air conditioner selection with TOPSIS and VIKOR methods in multi-criteria decision making,” *Çankırı Karatekin University, Journal of the Faculty of Economics and Administrative Sciences*, vol. 4, no. 1, pp. 267–282, 2014.
- [23] M. Kuo and G. Liang, “Combining VIKOR with GRA techniques to evaluate service quality of airports under fuzzy environment,” *Expert Systems with Applications*, vol. 38, no. 3, pp. 1304–1312, 2011.

## Research Article

# Improving the Hybrid Photovoltaic/Thermal System Performance Using Water-Cooling Technique and Zn-H<sub>2</sub>O Nanofluid

Hashim A. Hussein, Ali H. Numan, and Ruaa A. Abdulrahman

*Electromechanical Engineering Department, University of Technology, Baghdad, Iraq*

Correspondence should be addressed to Hashim A. Hussein; hashim171967@gmail.com

Received 2 October 2016; Revised 20 December 2016; Accepted 16 January 2017; Published 2 May 2017

Academic Editor: Md. Rabiul Islam

Copyright © 2017 Hashim A. Hussein et al. This is an open access article distributed under the Creative Commons Attribution License, which permits unrestricted use, distribution, and reproduction in any medium, provided the original work is properly cited.

This paper presented the improvement of the performance of the photovoltaic panels under Iraqi weather conditions. The biggest problem is the heat stored inside the PV cells during operation in summer season. A new design of an active cooling technique which consists of a small heat exchanger and water circulating pipes placed at the PV rear surface is implemented. Nanofluids (Zn-H<sub>2</sub>O) with five concentration ratios (0.1, 0.2, 0.3, 0.4, and 0.5%) are prepared and optimized. The experimental results showed that the increase in output power is achieved. It was found that, without any cooling, the measuring of the PV temperature was 76°C in 12 June 2016; therefore, the conversion efficiency does not exceed more than 5.5%. The photovoltaic/thermal system was operated under active water cooling technique. The temperature dropped from 76 to 70°C. This led to increase in the electrical efficiency of 6.5% at an optimum flow rate of 2 L/min, and the thermal efficiency was 60%. While using a nanofluid (Zn-H<sub>2</sub>O) optimum concentration ratio of 0.3% and a flow rate of 2 L/min, the temperature dropped more significantly to 58°C. This led to the increase in the electrical efficiency of 7.8%. The current innovative technique approved that the heat extracted from the PV cells contributed to the increase of the overall energy output.

## 1. Introduction

Photovoltaic (PV) systems represent a solution for the problem of low carbon, nonfossil fuel used to generate electricity. Solar radiation absorbed and converted by semiconductor devices (solar cells) can provide a supply of electricity to meet energy needs. An energy source with less emissions of carbon, no dependence on fossil fuels, massive potential for developing countries, and well suited to be distributed, PV, is considered as a medium and long range energy prospect as presented by Firth [1]. The photovoltaic system has advantages compared to other systems, such as low maintenance, unattended operation, reliable long life between 20 and 30 years, no fuel and no fumes, easy to install, and low recurrent costs as presented by Oi [2]. Basically, the solar PV/T system can be broadly categorized into two systems: photovoltaic and solar thermal system. The PV/T system refers to a system that uses heat transfer fluid to extract heat from the panel. The fluid is water or air and sometimes both. The photovoltaic thermal system (PV/T) has been

developed for several reasons; one of the main reasons is that the PV/T system can give higher efficiency than PV alone and thermal collector system as presented by Teo [3]. The application of nanofluid in solar collectors leads to a homogeneous temperature distribution inside the receiver. In addition, greater light absorption, a high absorption at visible wavelengths, and a low emissivity at infrared wavelengths can be achieved, and sunlight can be directly converted into useful heat as presented by Taylor et al. [4]. Nanoparticles have the following advantages in solar power plants: (1) the extremely small size of the particles ideally allows them to pass through pumps and plumbing without adverse impacts, (2) nanofluids can absorb energy directly skipping intermediate heat transfer steps, (3) the nanofluids can be optically selective (i.e., high absorption in the solar range and low remittance in the infrared), (4) a more uniform receiver temperature can be achieved inside the collector (reducing material constraints), (5) enhanced heat transfer via greater convection and thermal conductivity may enhance receiver performance, and (6) absorption efficiency may be improved by tuning the



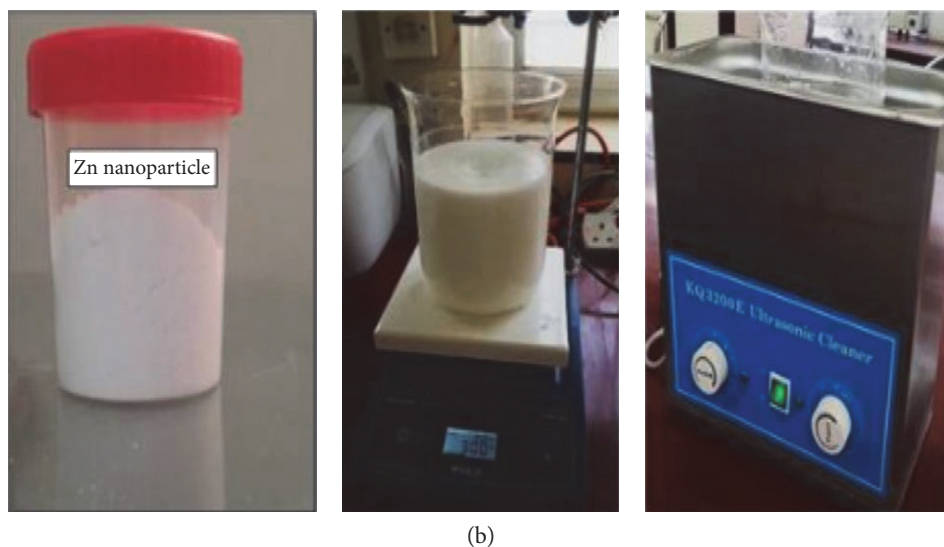
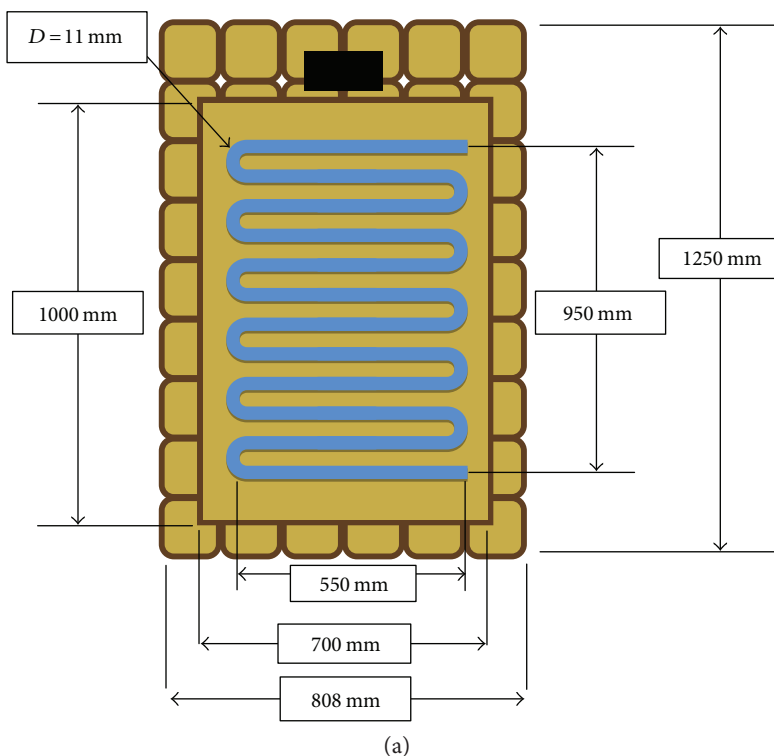


FIGURE 2: (a) Dimensions of thermal pipes mounted on the backside of PV. (b) Steps of nanofluid preparation.

Chaji et al. [8] studied the effect of various concentrations of  $\text{TiO}_2$  nanoparticles in water with three values of flow rates, namely, 36, 72, and 108 L/hr. They investigated four particles' concentration ratios (0, 0.1, 0.2, and 0.3% wet). The results showed that adding nanoparticles to water increased the initial efficiency of flat plate solar collector by 3.5 to 10.5% and the index of collector total efficiency by 2.6 to 7% relative to that of the base fluid.

The major problem in PV is the accumulation of heat, which reduces the electrical performance obviously; therefore, heat must be dissipated. In Iraq, the problem becomes much serious, because of a hot weather in most of the year;

this makes the electrical efficiency of PV cells to decrease with the increase of the heat inside the PV cells. The active solution for this problem can be using a water-cooling technique to decrease the heat effects by transferring the heat to the water which can be used in many applications as a hot water. Thermal conductivity enhancement can be achieved by using nanofluid applications such as  $\text{Zn-H}_2\text{O}$ . The originality of the current work is the use of a new design of a cooling technique including copper pipes placed on PV rear surface to absorb the heat accumulated inside the PV cells. This aim was achieved through evaluation of the performance of photovoltaic panels

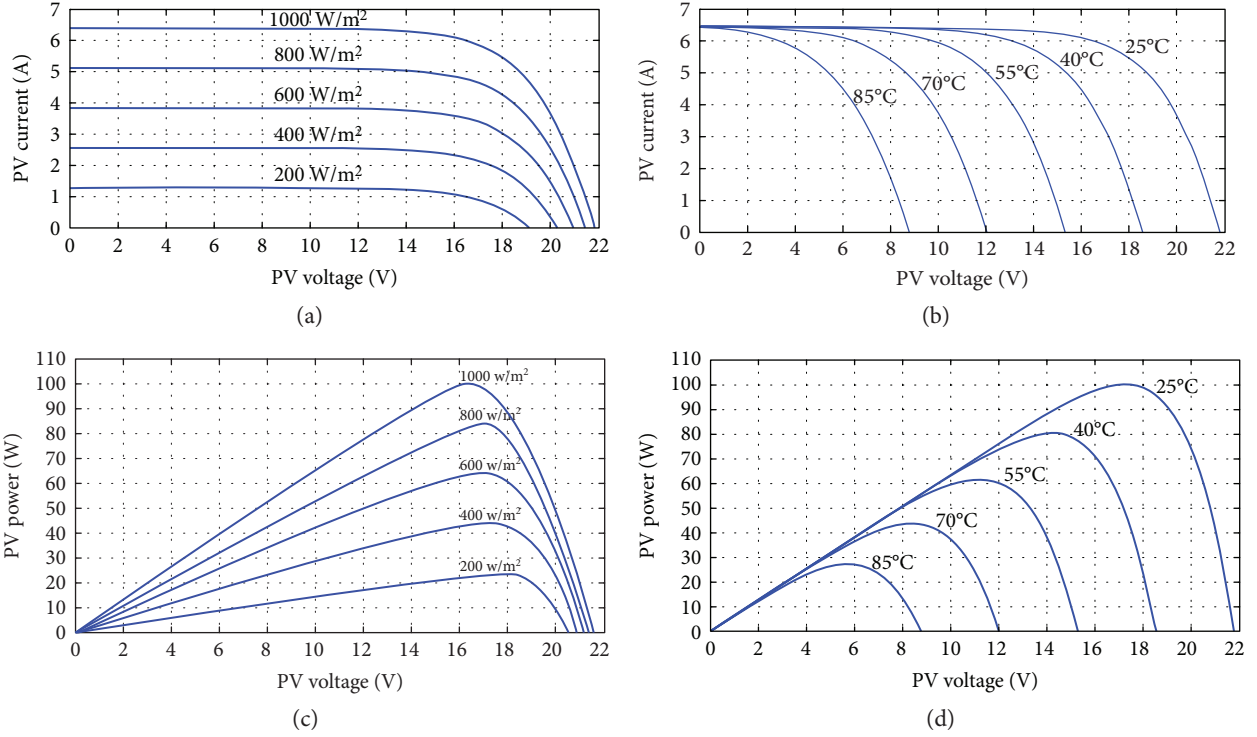


FIGURE 3: (a) Theoretical  $I$ - $V$  characteristics with radiation at constant temp. ( $25^{\circ}\text{C}$ ). (b)  $P$ - $V$  characteristics with radiation at constant temp. ( $25^{\circ}\text{C}$ ). (c)  $I$ - $V$  characteristics with temperature at constant radiation ( $1000\text{ W/m}^2$ ). (d)  $P$ - $V$  characteristics with temperature at constant radiation ( $1000\text{ W/m}^2$ ).

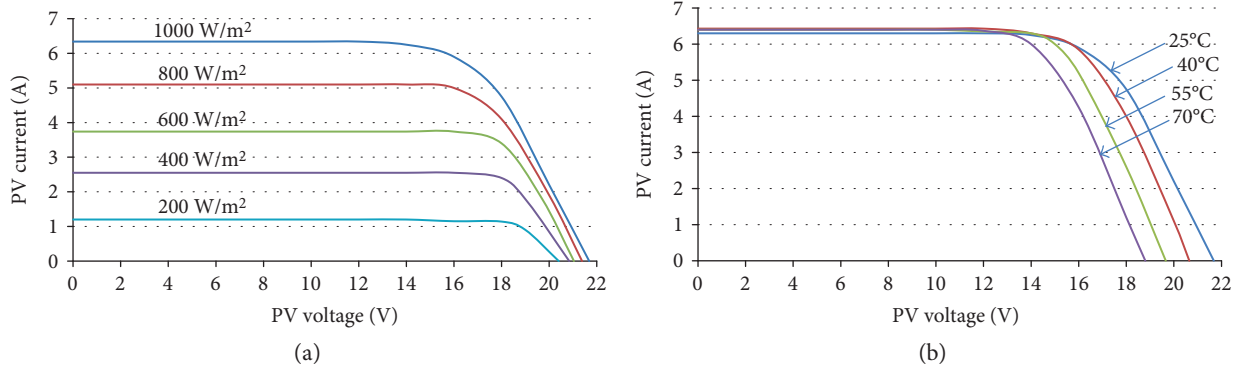


FIGURE 4: (a) Experimental  $I$ - $V$  characteristics with radiation at constant temp. ( $25^{\circ}\text{C}$ ). (b)  $I$ - $V$  characteristics with temp. at constant radiation ( $1000\text{ W/m}^2$ ).

under different operating conditions, enhancement of the electrical and thermal performance for the photovoltaic/thermal system with water pumping system at different water mass flow rates, and studying the effect of using nanofluid (Zn) as a working fluid in water-circulating pipes at different concentration ratios (0.1, 0.2, 0.3, 0.4, and 0.5).

## 2. Mathematical Modeling

**2.1. Overall Performance of PV/T System.** The equations of the nominal electrical efficiency ( $\eta_0$ ) presented by Ben [9] are as follows:

$$\eta_0 = \frac{V_{mp} I_{mp}}{A_c G}, \quad (1)$$

$$\eta_{elec} = \eta_0 [1 - \beta(T_c - T_0)],$$

$$Q = m C_p (T_0 - T_i).$$

The thermal efficiency is evaluated by the following equations, presented by El-Seesy et al. [10]:

$$\eta_{th} = \frac{m c_p (T_0 - T_i)}{A_c G}, \quad (2)$$

$$\eta_{total} = \eta_{th} + \eta_{elec} = \frac{m c_p \int (T_0 - T_i) dt + \int V I dt}{A_c \int G(t) dt}.$$

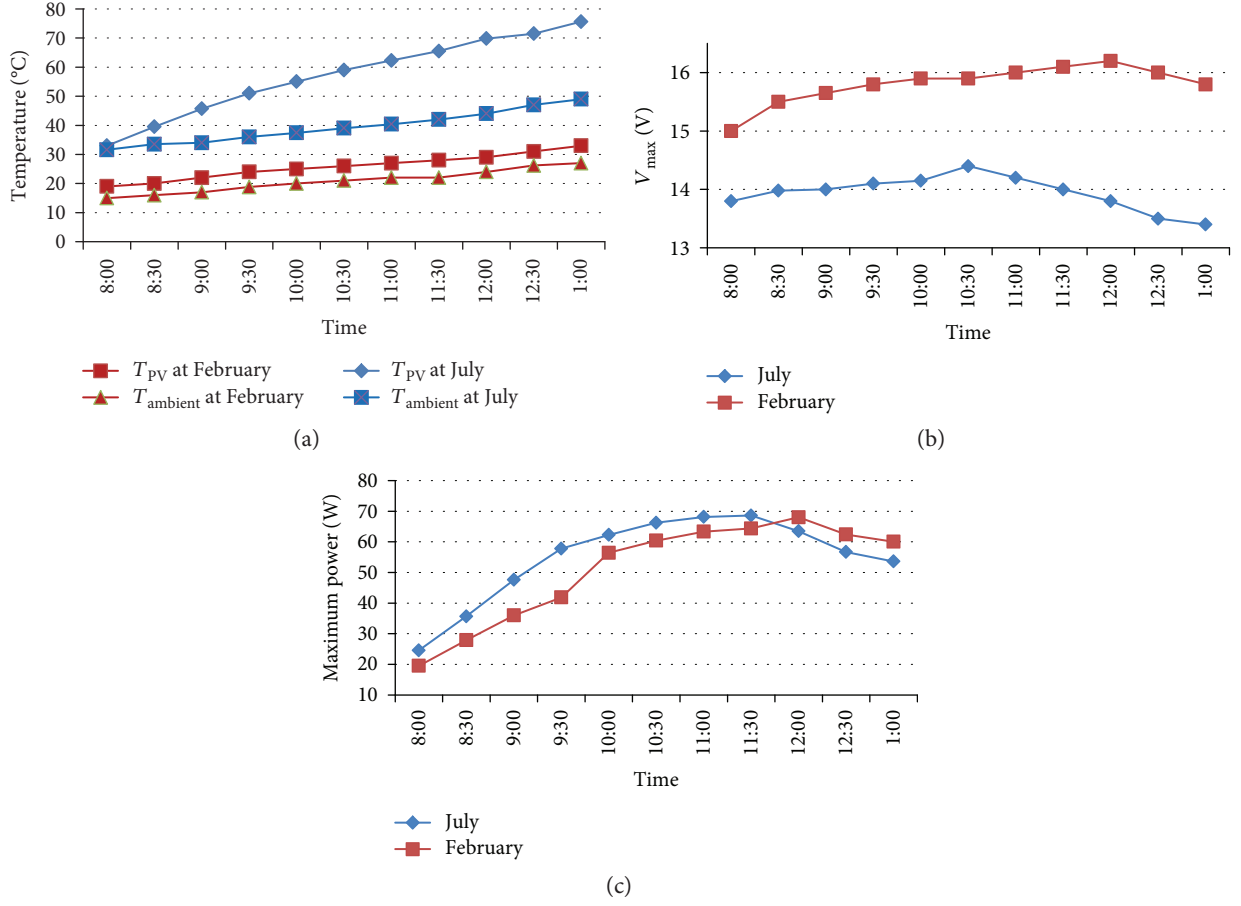


FIGURE 5: (a) Temperature variations at climatic conditions. (b) Comparison between the voltages at climatic conditions. (c) Comparison between the output powers at climatic conditions.

**2.2. Thermophysical Properties of Zn-H<sub>2</sub>O Nanofluid.** Thermophysical properties of the working fluid (Zn-H<sub>2</sub>O nanofluid) are changed due to influence of the nanoparticles. These properties for conventional fluids can be found from standard tables or equations as presented by Darby [11]. The properties of nanofluids can be estimated by using the following equations, as presented by Albadr and Hussein [12, 13]:

$$\begin{aligned}
 \rho_{nf} &= (1 - \phi)\rho_f + \phi\rho_p, \\
 (\rho C_p)_{nf} &= (1 - \phi)(\rho C_p)_f + \phi(\rho C_p)_p, \\
 \mu_{nf} &= (1 + 2.5\phi)\mu_w, \\
 K_{nf} &= \left[ \frac{K_p + 2K_f - 2(K_f - K_p)\phi}{K_p + 2K_f - (K_f - K_p)\phi} \right] K_f, \\
 \phi &= \frac{m_p/\rho_p}{(m_p/m_p) + (m_f/\rho_f)}, \\
 \alpha_{nf} &= \frac{K_{nf}}{\rho_{nf} C_{p_{nf}}}, \\
 \nu &= \frac{\mu}{\rho}.
 \end{aligned} \tag{3}$$

Calculation of Reynolds, Peclet, and Prandtl numbers is as follows [13]:

$$\begin{aligned}
 Re &= \frac{VD}{\nu}, \\
 Pe &= \frac{VD}{\alpha_{nf}}, \\
 Pr &= \frac{\nu_{nf}}{\alpha_{nf}}.
 \end{aligned} \tag{4}$$

Friction factors ( $f$ ) and Nusselt numbers ( $Nu$ ) for single-phase flow have been calculated from the following equations:

$$\begin{aligned}
 f &= [1.58 \ln Re - 3.82]^{-2}, \\
 Nu &= \frac{(0.125 f)(Re - 1000)Pr}{1 + 12.7 (0.125 f)^{0.5} (Pr^{2/3} - 1)}.
 \end{aligned} \tag{5}$$

Friction factor of each flow rate for nanofluid which can be found in single-phase flow cannot be used for calculating friction factor as well as Nusselt number as presented by Hussein [13].

$$\begin{aligned}
 f &= 0.961 Re^{-0.375} \phi^{0.052}, \\
 Nu &= 0.074 Re_{nf}^{0.707} Pr_{nf}^{0.385} \phi^{0.074}.
 \end{aligned} \tag{6}$$

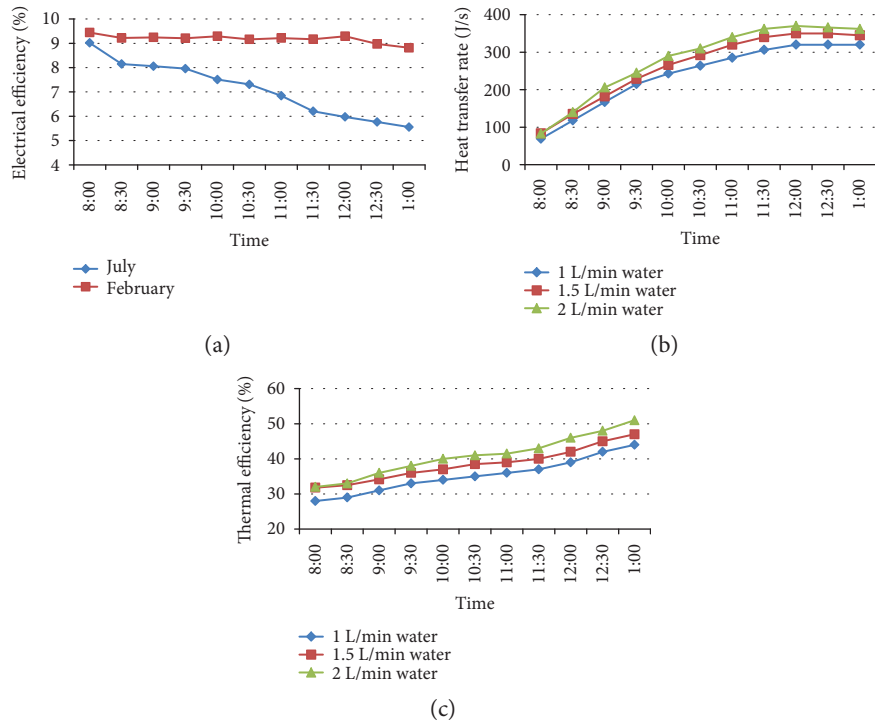


FIGURE 6: (a) Comparison of the electrical efficiency at climatic conditions. (b) Heat transfer rate with different mass flow rates. (c) Effect of the mass flow rates of water on the thermal efficiency.

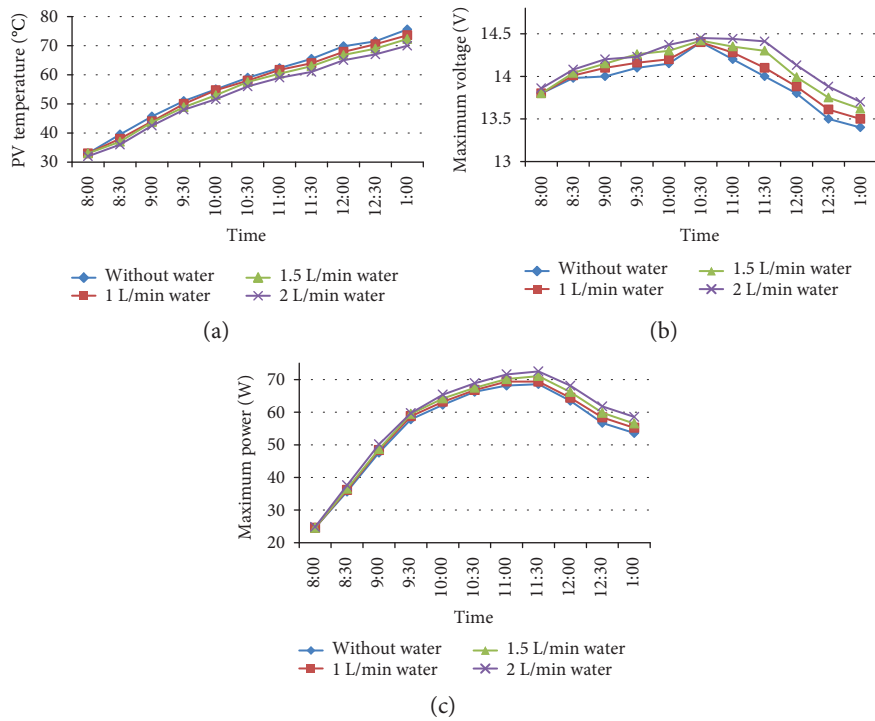


FIGURE 7: (a) Effect of mass flow rates on the PV temperature. (b) Effect of mass flow rates on the voltage. (c) Effect of mass flow rates on the PV power.

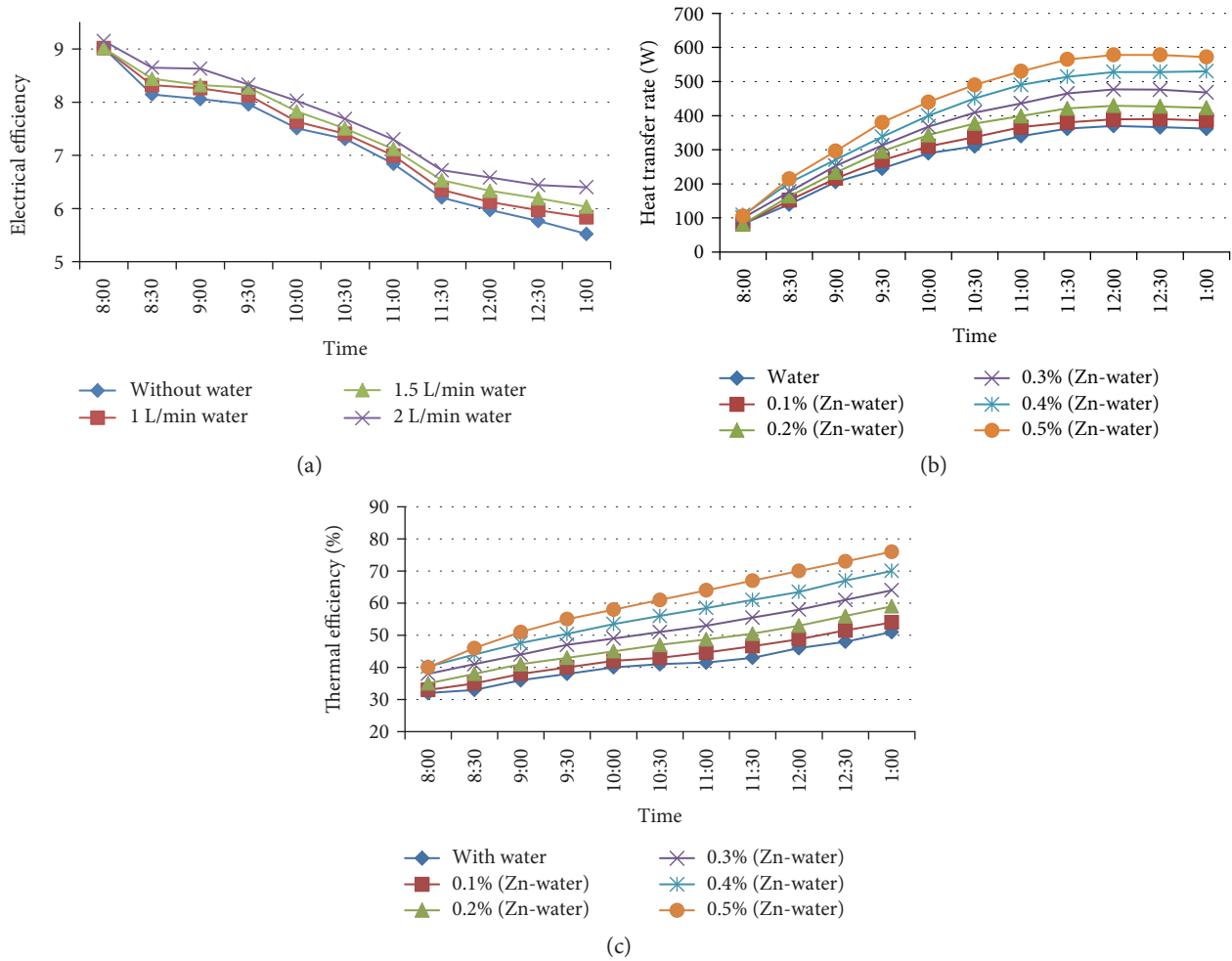


FIGURE 8: (a) Effect of mass flow rates on the electrical efficiency. (b) Heat transfer rate at constant flow rate (2 L/min) at different nanofluid concentrations. (c) Effect of Zn-H<sub>2</sub>O nanofluid at 2 L/min on thermal efficiency.

### 3. Material and Methods

**3.1. Experimental Setup.** The prototype of PV/T system is where the water pumping system was used for all experimental investigations of electrical and thermal effects on system performance and suggested improvements. The setup comprises PV panel, charge controller, battery, DC-DC boost converter, PMDC motor used as a pumping system load, copper pipes fixed on the backside of PV panel, and a radiator with a fan and circulation pump for cooling hot water. The experiment was performed on the site of Electromechanical Engineering Department, University of Technology, in summer and winter seasons.

The photograph of the setup as shown in Figures 1(a) and 1(b) explains the schematic diagram of the complete experimental setup. The major component of the experimental setup is the PV panel that produces direct current (DC) electricity. In this work, the SR-100S PV panel which was made from a monocrystalline semiconductor has been used. The PV panel consists 9 × 6 cells which have generated 100 Watts maximum power under standard test condition (STC) and typically can generate nearly 5.8 A at maximum solar

radiation. The quantities measured during the experiment were as follows: (1) Digital solar meter mounted on the plane of a photovoltaic panel is used to indicate the change of solar irradiance. (2) Five K-type thermocouples connected to the 12-channel digital temperature recorder (type Lutron BTM-4208SD) were used to measure the temperature of PV panel, working fluid, and ambient temperature. (3) The maximum current and voltage, short-circuit current and open-circuit voltage, of the PV panel were recorded manually using multimeters. (4) The mass flow rate of the working fluid (Zn-H<sub>2</sub>O nanofluid) was measured using flow rate meter.

**3.2. PV/T Description.** In this work, a specially made serpentine flow collector has been designed. The PV/T collector comprises PV module and thermal collector which are made of copper sheet and pipe. The copper sheet and the piping are paste directly to the back side of PV panel. Copper material has been used due to its high thermal conductivity with the pipe's inner diameter of 11 mm and thickness of 1 mm to transfer the temperature from PV panel to the working fluid. Thermal sink was used between the bottom surface of PV

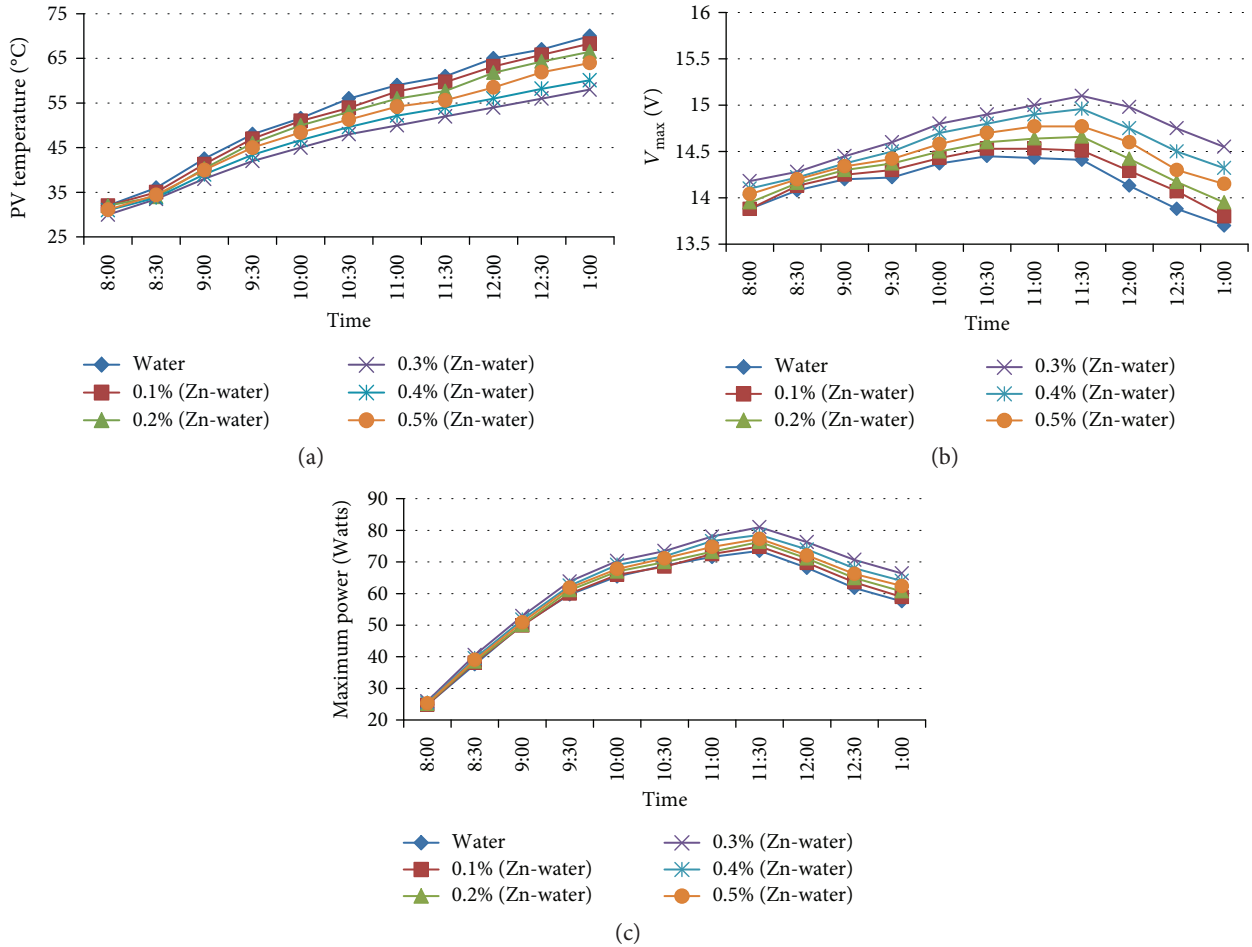


FIGURE 9: (a) Effect of Zn-H<sub>2</sub>O nanofluid at 2 L/min on the photovoltaic temperature. (b) Effect of Zn-H<sub>2</sub>O nanofluid at 2 L/min on the voltage. (c) Effect of Zn-H<sub>2</sub>O nanofluid at 2 L/min on the power.

panel and the surface of 2 mm copper plate to increase thermal conductivity.

The copper pipes are linked using a welding machine. The storage capacity of piping system is 1.5 liters welded on the copper sheet with a height and length and then fixed on the back surface of standard PV panel. The welding method is with 40% tin and 60% silver. The oscillatory flow has at least one inlet and outlet to permit working fluid to enter and to exit from the copper pipes, respectively. Water enters the pipes with low temperature and travel as hot water. The hot water can be consumed or stored for later use. However, this work is dedicated to water pumping system and thus there is no need for hot water output from the proposed PV/T system. In this way, solar radiation energy can be fully used for solar heating applications. The dimension of the thermal collector is shown in Figure 2(a).

**3.3. Preparation of Nanofluid.** After studying the impact of a water-cooling technique on the performance of PV/T system, Zn-water nanofluid was prepared at five concentration ratios (0.1, 0.2, 0.3, 0.4, and 0.5%) by mixing the particles with 1.5 liters of ionized water. Figure 2(b) shows that Zn-water nanofluid has been prepared in the corrosion laboratory of

the Materials Engineering Department at the University of Technology. Nanopowder was purchased, and a type of Zn nanoparticle was used in this study. The diameter of the nanoparticle is 30 nm.

## 4. Results and Discussion

**4.1. Simulation of the PV Output Characteristics.** The PV Matlab model that has been developed is tested to assess the solar radiation effects and PV temperature variations. From the results, it notes that the current increases proportionally with the increase of solar radiation, but the voltage increases nonlinearly with solar radiation and then increases the level of power output as shown in Figure 3. On the other hand, the temperature primarily affects the PV voltage. The rising temperature of PV panel primarily influences the PV voltage more than the PV current. That reason subsequently leads to decrease the power. When the temperature of PV module increases from 25 to 85 at irradiation of 1000 W/m<sup>2</sup>, the PV open-circuit voltage is decreased from 21.8 to 18.8 volts and this leads to decrease the PV power generated from 100 to 84 Watts which represents the variation of current-voltage (*I-V*) and power-voltage (*P-V*)

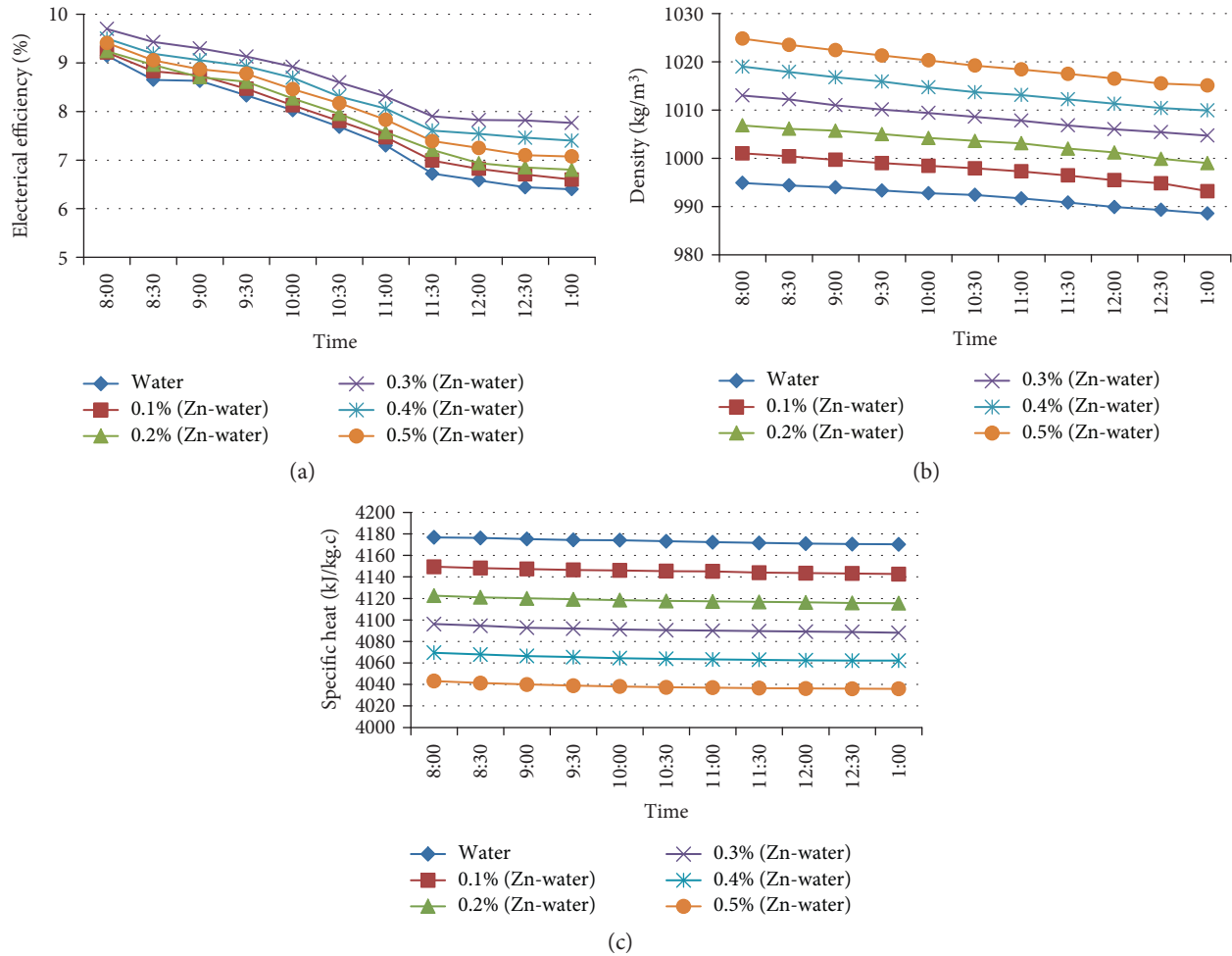


FIGURE 10: Effect of Zn-H<sub>2</sub>O nanofluid concentrations at 2 L/min on (a) electrical efficiency, (b) working fluid density, and (c) specific heat.

characteristics. After solving the governing equations of the electrical and thermal performance of the system as mentioned in the introduction section which helped to determine and obtained the results, the thermal performance of PV/T system is shown in Figure 4.

**4.2. PV Performance with Water-Cooling Technique.** Figure 5 shows the temperature difference, voltage, and maximum power variations of the hybrid system PV/T, respectively. These curves represented the changing of temperature difference depending on the solar radiation and ambient temperature with time. The temperature difference between inlet and outlet is almost in linear relationship with the solar radiation at changing value of radiation from 200 W/m<sup>2</sup> to 900 W/m<sup>2</sup> and then falls to 700 W/m<sup>2</sup> nearly. It is observed that when the increase of flow rate causes a decrease in the output temperature and the temperature difference and when the decrease of flow rate leads to increase in the output temperature and the temperature difference and then gets the best thermal gain, this is due to the fluid which takes a long time to absorb heat from the surface of PV module.

Figure 6 shows that the 2 L/min flow rate gives the best performance for the thermal efficiency of the PV/T system due to the increase in heat transfer rate of fluid in pipes which represents that the 2 L/min flow rate of working fluid (water) gives good improvement in current and voltage for photovoltaic/thermal system due to the reduction in photovoltaic temperature at this value of flow rate and the cooling process gives improvement on power generated from photovoltaic, but the better power produced at the 2 L/min flow rate is because more heat dissipated in the radiator with increasing flow rate of working fluid circulated.

It is observed that the electrical efficiency of the PV module increases with increasing the flow rate of fluid. The best electrical efficiency is obtained at optimum flow rate (2 L/min) because all the performance is improved at this rate. The results show that the operation of pumping system depends deeply on the performance of the photovoltaic system and the peak power of the photovoltaic system. The DC voltage influences the speed of running motor. It is observed that low voltage generated from PV module due to high operating temperature leads to a decrease in the output of DC pump, while high voltage leads to an increase

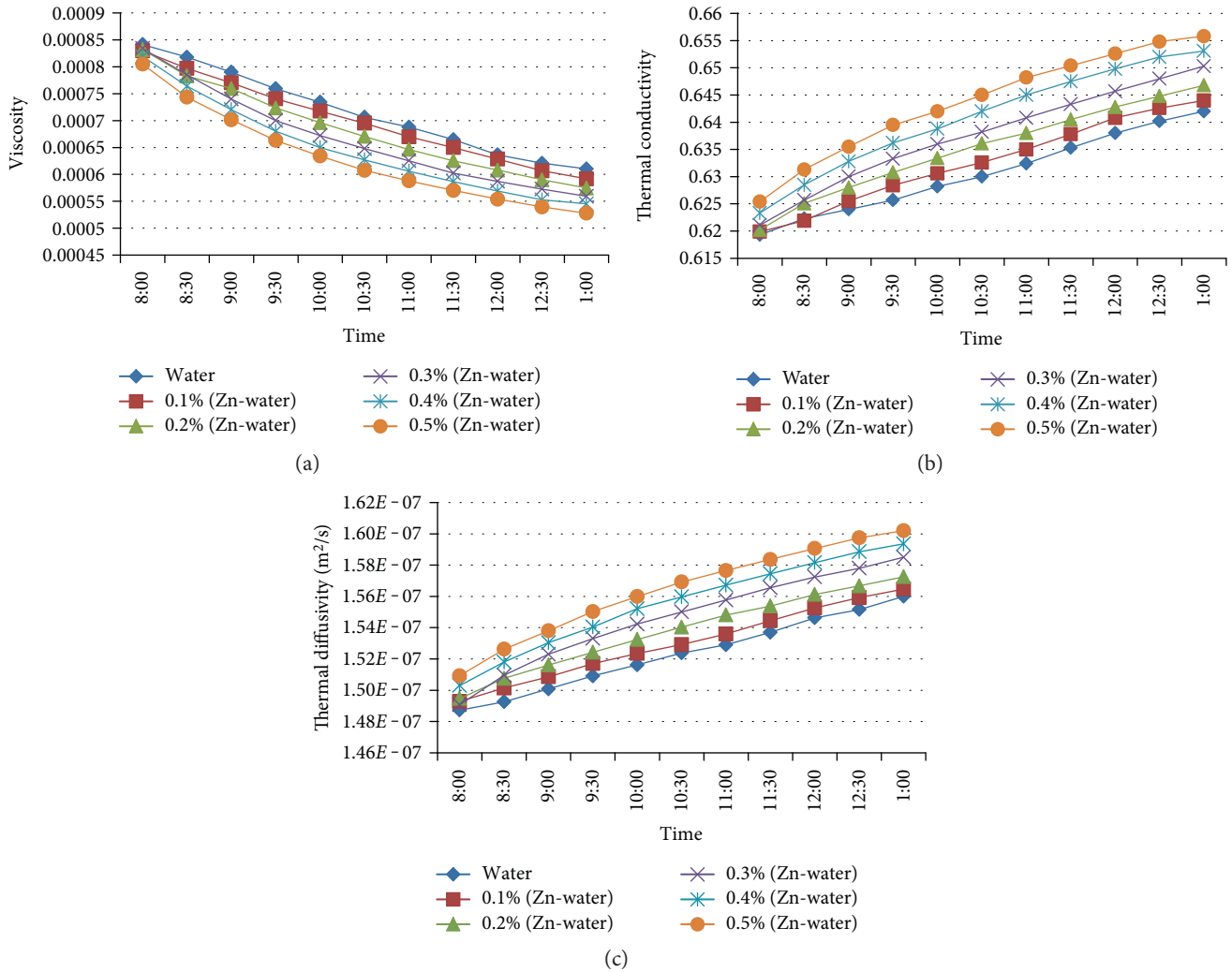


FIGURE 11: Effect of Zn-H<sub>2</sub>O nanofluid at 2 L/min on (a) viscosity, (b) thermal conductivity, and (c) thermal diffusivity.

in the output of DC pump. It is observed that circulating the fluid through pipes at photovoltaic cells' rear surface strongly enhances the performance of system and subsystem, since motor pump can receive most of the power of cells by improving the performance of PV module as shown in Figure 7.

**4.3. PV Performance with the Use of Zn-H<sub>2</sub>O Nanofluid.** The thermal conductivity of Zn metal is higher than the water: 112.2 W/m.k for Zn metal while for the water, 0.596 W/m.k. This feature gives an increase in the thermal conductivity of working fluid. Figure 8(b) shows that the heat transfer rate increases with the increase of volume concentration ratio of nanofluid because the nanofluid thermal conductivity increases as the concentration ratios of nanofluid increases and that led to an increase in the thermal performance of photovoltaic/thermal system as shown in Figure 8(c) that is due to the increase of heat transfer rate with the concentration ratio. It is found that 2 L/min of mass flow rate gives the best thermal performance and electrical performance under water test of PV/T.

Figure 9 explains that the value 0.3% gives the best cooling for photovoltaic. This is due to the increase in thermal conductivity of Zn-H<sub>2</sub>O nanofluid at this ratio which led to more absorption of heat from photovoltaic surface. If the concentration ratio increases more than 0.3%, the PV temperature will increase because of the increase in density and viscosity of working fluid with the rising of concentration ratio, and this gives reverse impact of improvement. By decreasing PV temperature with the use of nanofluid, the maximum power produced from the PV module will be increased. It was noticed that the better maximum power generated is at 0.3% nanofluid concentration ratio because this volume ratio gives good cooling for PV module; also, it was observed that there is an improvement in  $I_{max}$  and  $V_{max}$  which leads to enhancement in PV power when using nanofluid and a good case at 0.3% concentration ratio. The electrical efficiency of PV module is improved by using nanofluid at 0.3% volume concentration ratio and reduced when it is greater than 0.3% because of the increase of PV temperature as the volume concentration ratio increases above 0.3%, as shown in Figure 10.

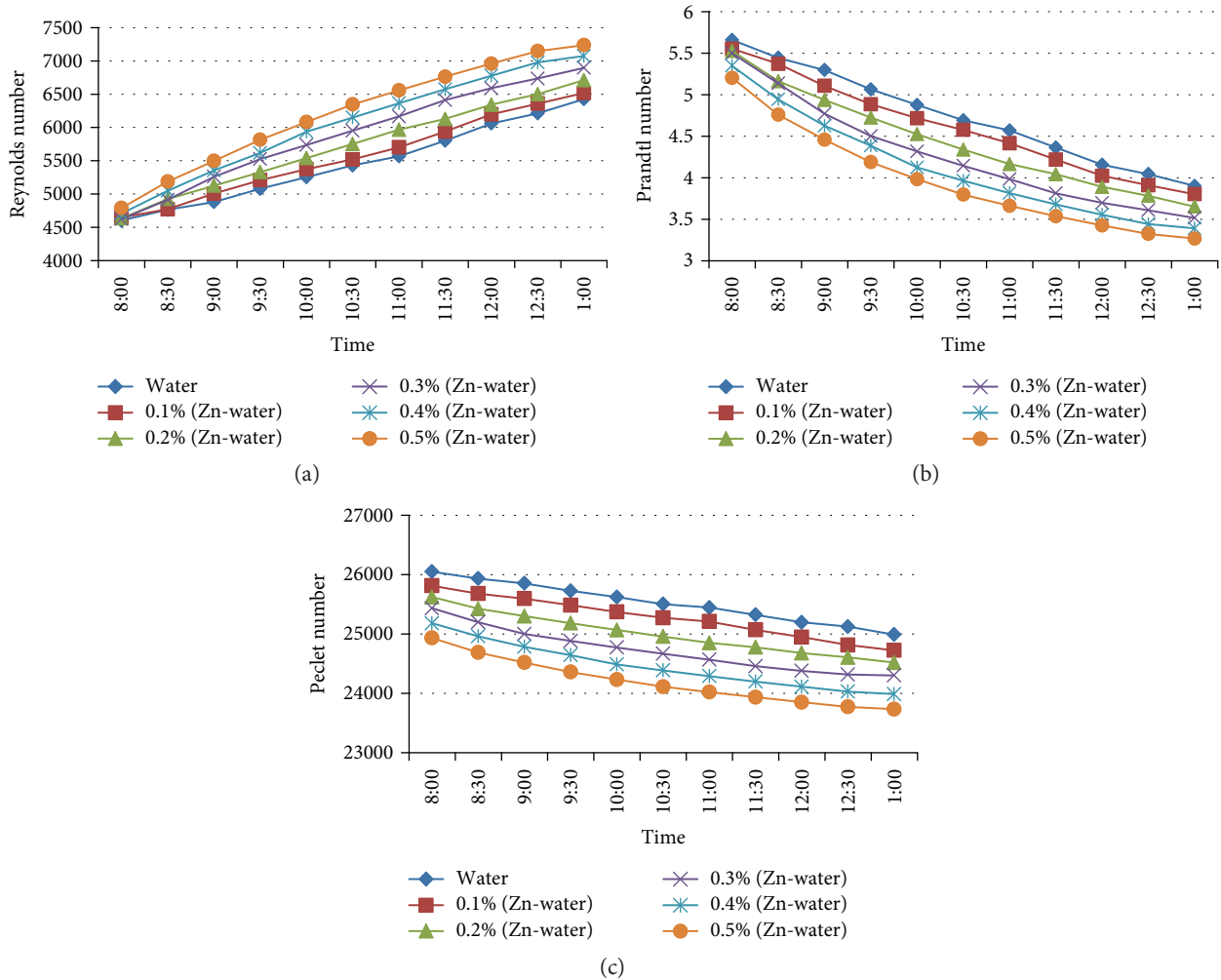


FIGURE 12: Effect of Zn-H<sub>2</sub>O nanofluid at 2 L/min on (a) Reynolds number, (b) Prandtl number, and (c) Peclet number.

4.4. *Physical Properties of Zn-H<sub>2</sub>O Nanofluid.* All the physical properties of working fluid will change depending on the concentration ratio of nanoparticles such as density, specific heat, viscosity, and thermal conductivity. It was observed from the sketch that the variation of density of nanofluid is a function of volume concentration ratios and the density of water when increasing the temperature. Figure 11(a) represents the changes in specific heat of nanofluid with increasing the volume concentration ratios. This behavior is due to the change in density of nanofluid as a function of temperature. Figure 11(b) represents the viscosity of nanofluid as a function of volume concentration ratio. The results showed the decrease in nanofluid viscosity at all volume concentration ratios with rising temperature; this is explained by changing the physical properties of the water at rising temperature. Figure 11 shows the changes in thermal conductivity and thermal diffusivity of nanofluid, respectively, with increase in volume concentration ratios where the thermal conductivity is the most important in the physical properties of nanofluid, and it primarily depends on the temperature of fluid. It was observed that at higher temperature, there is greatest impact on these

values and we noticed that with increasing the concentration ratios, the more heat are absorbed at the same time as compared with all values of volume concentration ratios, and this rise in temperatures leads to an increase in the thermal conductivity and thermal diffusivity of nanofluid, respectively. Figure 12 shows the influence of volume concentration ratios on Reynolds number; increasing concentration ratios led to increasing absorbing temperature, leading to increase in Reynolds number. This increase in Reynolds number is due to the reduction in viscosity of nanofluid and increase in density of nanofluid. Figure 12(c) represents the decreasing in Prandtl number with increasing in temperature for all volume concentration ratios; this is due to the increase in density and thermal diffusivity and the decline in viscosity with higher temperature. The influence of volume concentration ratios on Peclet number is shown in Figure 13. It is observed from the graph that the Peclet number decreased because of the increase in thermal diffusivity. The influence of volume concentration ratios as a function of temperature on the Nusselt number is shown in Figure 13(b). It was observed that the Nusselt number increased with volume concentration ratios (0.1,

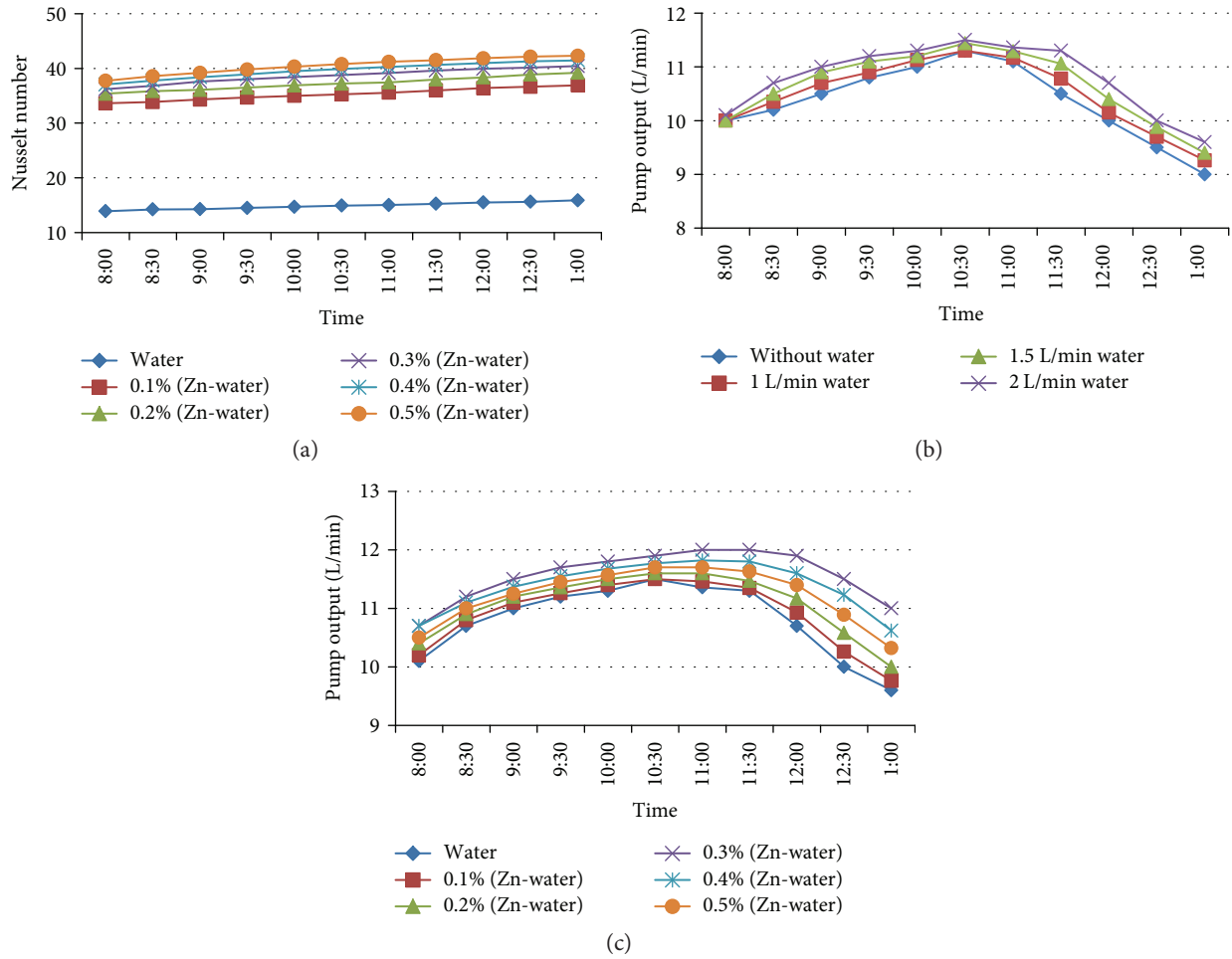


FIGURE 13: Effect of Zn-H<sub>2</sub>O nanofluid at 2 L/min on (a) Nusselt number, (b) pump output at different mass flow rates, and (c) pump output at constant mass flow rate (2 L/min) with different concentration ratios.

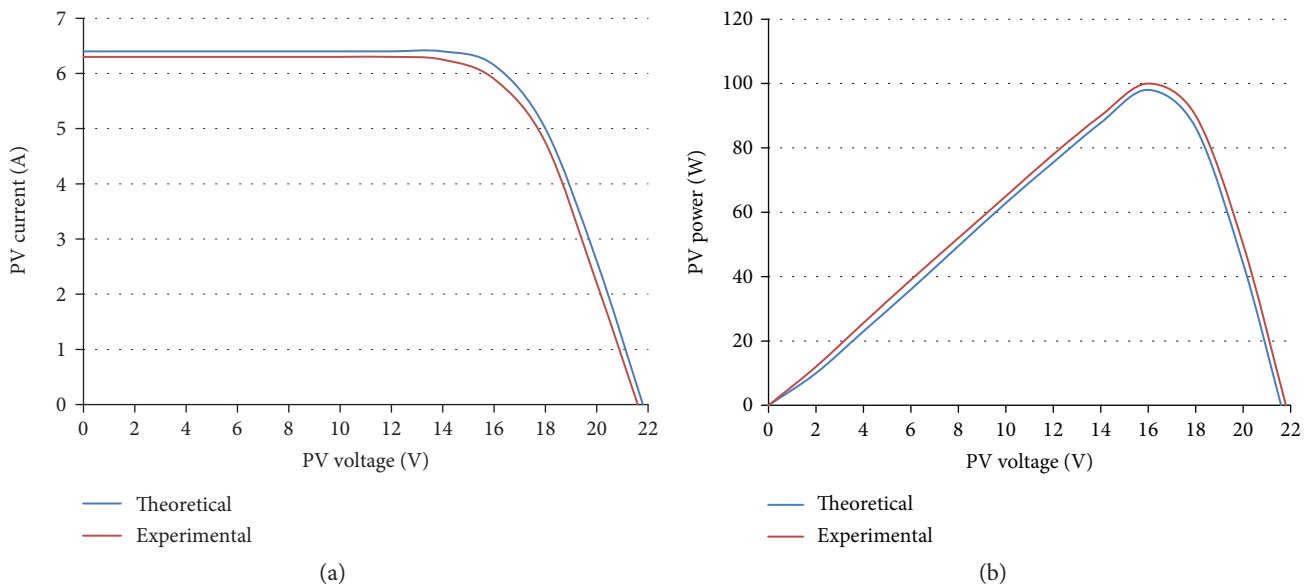


FIGURE 14: (a) Theoretical and experimental results comparison of  $I-V$  at 25°C, 1000 W/m<sup>2</sup>. (b) Theoretical and experimental results comparison of  $P-V$  at 25°C, 1000 W/m<sup>2</sup>.

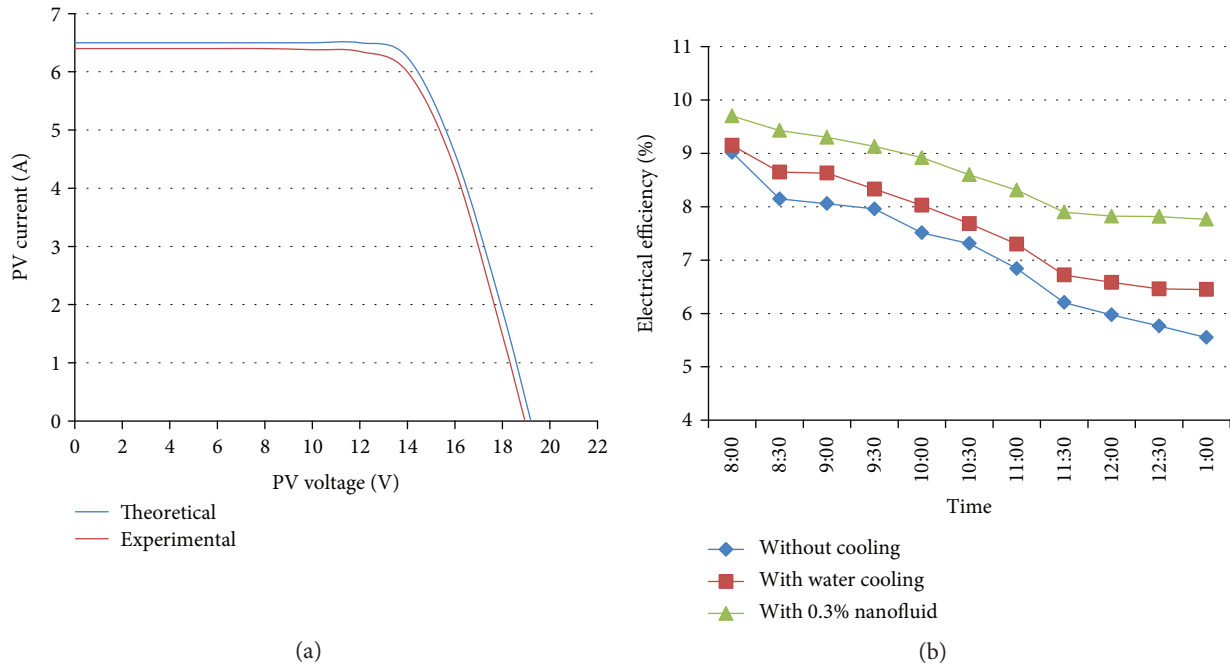


FIGURE 15: (a) Theoretical and experimental results comparison of  $I$ - $V$  at  $1000 \text{ W/m}^2$  and  $70^\circ\text{C}$ . (b) Comparison of electrical efficiency of PV/T without water, with water (2 L/min), and with Zn- $\text{H}_2\text{O}$  nanofluid.

0.2, 0.3, 0.4, and 0.5%). This increase is due to the increase of the Reynolds and Prandtl numbers with the rising temperature, and with increasing concentration ratios, this leads to increasing the value of Nusselt number.

**4.5. PV Performance of Water Pumping System.** In this work, we have tested the operation of pumping systems designed to supply water for drinking or irrigation. The results show that the operating of pumping system depends deeply on the performance of the photovoltaic system and the peak power of the photovoltaic system.

The goal achieved via this study is the investigation of solar radiation changing effects on the pumping system performances. The obtained results show that due to increasing solar radiation, the pump flow increased. The DC voltage influences the speed of running motor. It is observed that low voltage generated from PV module due to high operating temperature lead to a decrease in the output of DC pump, while high voltage lead to an increase in the output of DC pump. It is observed that circulating the fluid through pipes at the photovoltaic cells' rear surface strongly enhances the performance of systems and subsystems, since motor pumps can receive most of the power of the cells by improving performance of the PV module as shown in Figures 13(b) and 13(c).

**4.6. Results Comparison.** When comparing between the experimental results which have been measured manually as shown in Figures 15(a) and 15(b) with theoretical results obtained from simulation using Matlab/Simulink for PV characteristics under the conditions (1) effect of solar radiation at constant temperature ( $25^\circ\text{C}$ ) and (2) effect of temperature at constant irradiation ( $1000 \text{ W/m}^2$ ). It can

be noticed from these figures that the difference between experimental and theoretical results is about less than 2% which is quite acceptable.

## 5. Conclusions

The variations in solar radiation mainly influence the output current, while the changes in temperature mainly affect the output voltage. Hybrid PV/T systems are one of the methods used to enhance the electrical efficiency of panel then improve the photovoltaic water pumping system performance. The electrical and thermal efficiencies of the hybrid system will increase with increasing mass flow rate of water. At optimum flow rate of 2 L/min, electrical efficiency was 6.5% and thermal efficiency was 60%. The results indicated that when nanofluid (Zn) is used at various concentration ratios (0.1, 0.2, 0.3, 0.4, and 0.5%) at 2 L/min flow rate, the cell temperature dropped more significantly from  $76^\circ\text{C}$  to  $58^\circ\text{C}$  at an optimum concentration ratio of 0.3% nanofluid; this led to an increase in the electrical efficiency of PV panel to 7.8%.

## Nomenclature

- $A$ : Area of the PV module ( $\text{m}^2$ )
- $A_c$ : Area of collector ( $\text{m}^2$ )
- $C_{\text{pf}}$ : Heat capacity of the base fluid (J/kg.c)
- $C_{\text{pnf}}$ : Heat capacity of the nanofluid (J/kg.c)
- $G$ : Solar radiation ( $\text{W/m}^2$ )
- $I_m$ : Maximum current of PV (A)
- $I_{\text{sc}}$ : Short-circuit current of solar cell (A)
- $K_f$ : Thermal conductivity of base fluid (W/m.c)

$K_I$ : Cell's short-circuit current temperature coefficient (A/k)  
 $K_{nf}$ : Thermal conductivity of the nanofluid (W/m.c)  
 $K_p$ : Thermal conductivity of the nanoparticle (W/m.c)  
 $m$ : Mass flow rate (kg/s)  
 $\phi$ : Volume concentration of the nanoparticles  
 $T_{in}$ : Inlet temperature of the working fluid ( $^{\circ}$ C)  
 $T_0$ : Temperature of standard condition ( $25^{\circ}$ C)  
 $T_{out}$ : Outlet temperature of working fluid ( $^{\circ}$ C)  
 $V_m$ : Maximum voltage of PV (V)  
 $V_{PV}$ : Output voltage (V)  
 $\beta$ : Coefficient of silicon cell ( $\beta = 0.0045^{\circ}$ C $^{-1}$ )  
 $\eta_0$ : Nominal electrical efficiency at standard conditions  
 $\mu_{nf}$ : Nanofluid viscosity (kg/m.s)  
 $\mu_w$ : Water viscosity(kg/m.s)  
 $\rho_{nf}$ : Density of the nanofluid (kg/m $^3$ )  
 $\rho_p$ : Density of the nanoparticles (kg/m $^3$ ).

- [12] J. Albadr, "Heat transfer through heat exchanger using Al $2$ O $3$  nanofluid at different concentrations," *Case Studies in Thermal Engineering*, vol. 1, no. 1, pp. 38–44, 2013.
- [13] A. M. Hussein, "Experimental measurements of nanofluids thermal properties," *International Journal of Automotive and Mechanical Engineering (IJAME)*, vol. 7, pp. 850–863, 2013.

## Conflicts of Interest

The authors declare that they have no conflicts of interest.

## References

- [1] S. K. Firth, *Raising efficiency in photovoltaic systems: high resolution monitoring and performance analysis*, [Ph.D. Thesis], De Montfort University, UK, 2006.
- [2] A. Oi, *Design and simulation of photovoltaic water pumping system*, [MSc. Thesis], California Polytechnic State University, San Luis Obispo, California, 2005.
- [3] H. Teo, *Photovoltaic thermal (PV/T) system: effect of active cooling*, [MSc. Thesis], National University of Singapore, Singapore, 2010.
- [4] R. A. Taylor, P. E. Phelan, T. P. Otanicar et al., "Applicability of nanofluids in high flux solar collectors," *Renewable and Sustainable Energy*, vol. 3, no. 2, article 023104, 2011.
- [5] M. Abdolzadeh and M. Ameri, "Improving the effectiveness of a photovoltaic water pumping system by spraying water over the front of photovoltaic cells," *Renewable Energy*, vol. 34, no. 1, pp. 91–96, 2009.
- [6] W. A. EL-Basit, A. M. A. B. D. El-Maksood, and F. A. E.-M. S. Soliman, "Mathematical model for photovoltaic cells," *Leonardo Journal of Sciences*, vol. 23, pp. 13–28, 2013.
- [7] S. Odeh and M. Behnia, "Improving photovoltaic module efficiency using water cooling," *Heat Transfer Engineering*, vol. 30, no. 6, pp. 499–505, 2009.
- [8] H. Chaji, Y. Ajabshirchi, E. Esmaeilzadeh, S. Z. Heris, M. Hedayatizadeh, and M. Kahani, "Experimental study on thermal efficiency of flat plate solar collector using TiO $2$ /water nanofluid," *Modern Applied Science*, vol. 7, no. 10, p. 60, 2013.
- [9] H. Ben, "Study of electrical and thermal performance of a hybrid PVT collector," *International Journal of Electrical and Electronics*, vol. 3, no. 4, pp. 95–106, 2013.
- [10] I. E. El-Seesy, T. Khalil, and M. T. Ahmed, "Experimental investigations and developing of photovoltaic/thermal system," *World Applied Sciences Journal*, vol. 19, no. 9, pp. 1342–1347, 2012.
- [11] R. Darby, *Chemical Engineering Fluid Mechanics*, Marcel Dekker, Inc, New York, 2nd edition, 2001.

## Research Article

# Observer-Based Load Frequency Control for Island Microgrid with Photovoltaic Power

Chaoxu Mu,<sup>1</sup> Weiqiang Liu,<sup>1</sup> Wei Xu,<sup>2,3</sup> and Md. Rabiul Islam<sup>4</sup>

<sup>1</sup>Tianjin Key Laboratory of Process Measurement and Control, School of Electrical and Information Engineering, Tianjin University, Tianjin 300072, China

<sup>2</sup>State Key Laboratory of Advanced Electromagnetic Engineering and Technology, School of Electrical and Electronic Engineering, Huazhong University of Science and Technology, Wuhan 430074, China

<sup>3</sup>College of Mechanical and Electrical Engineering, Huanggang Normal University, Huanggang 438000, China

<sup>4</sup>Department of Electrical and Electronic Engineering, Rajshahi University of Engineering and Technology, Rajshahi 6204, Bangladesh

Correspondence should be addressed to Wei Xu; [weixu@hust.edu.cn](mailto:weixu@hust.edu.cn)

Received 28 November 2016; Accepted 5 February 2017; Published 26 April 2017

Academic Editor: Zofia Stasicka

Copyright © 2017 Chaoxu Mu et al. This is an open access article distributed under the Creative Commons Attribution License, which permits unrestricted use, distribution, and reproduction in any medium, provided the original work is properly cited.

As renewable energy is widely integrated into the power system, the stochastic and intermittent power generation from renewable energy may cause system frequency deviating from the prescribed level, especially for a microgrid. In this paper, the load frequency control (LFC) of an island microgrid with photovoltaic (PV) power and electric vehicles (EVs) is investigated, where the EVs can be treated as distributed energy storages. Considering the disturbances from load change and PV power, an observer-based integral sliding mode (OISM) controller is designed to regulate the frequency back to the prescribed value, where the neural network observer is used to online estimate the PV power. Simulation studies on a benchmark microgrid system are presented to illustrate the effectiveness of OISM controller, and comparative results also demonstrate that the proposed method has a superior performance for stabilizing the frequency over the PID control.

## 1. Introduction

With the technological innovation of modern power systems, renewable energy has been widely incorporated to the power system, such as wind energy and solar energy. Although renewable energy causes less pollution and is energy saving, the large-scale integration of renewable energy would have a significant impact on the power system since renewable energy is not ideal for power generation [1–3].

Load frequency stability is regarded as an indispensable factor when considering the stability of power systems [4]. For a microgrid system, if the imbalance between load consumption and power generation frequently happens, then a load frequency controller is required to have an adequate ability to quickly damp the frequency oscillation [5, 6]. The traditional load frequency model for the power system is approximated as a linear model near an operation point without the generator dynamics being involved, and the most

commonly used frequency control strategy for this kind of linear model is the PID control, as reported in [7]. After the offline tuning of parameters, the PID controller can have a good frequency damping performance within a certain range around the designed operation point [8]. With the nonlinear characteristics of power generation for renewable energy, it may be less effective to the microgrid system, especially when the microgrid system is far away from the set operation point. Besides, several advanced control methods have been used to the LFC problem in the last decade, such as fuzzy logic control [9–11], adaptive control [12, 13], and robust control [14]. Although the design of nonlinear control approaches is relatively complex, the research of advanced nonlinear control approaches on smart grid has been paid great attention since nonlinear control is more close to the characteristics of a power system itself [3, 15–18].

In this paper, we investigate the integral sliding mode (ISM) control method for load frequency control of an island

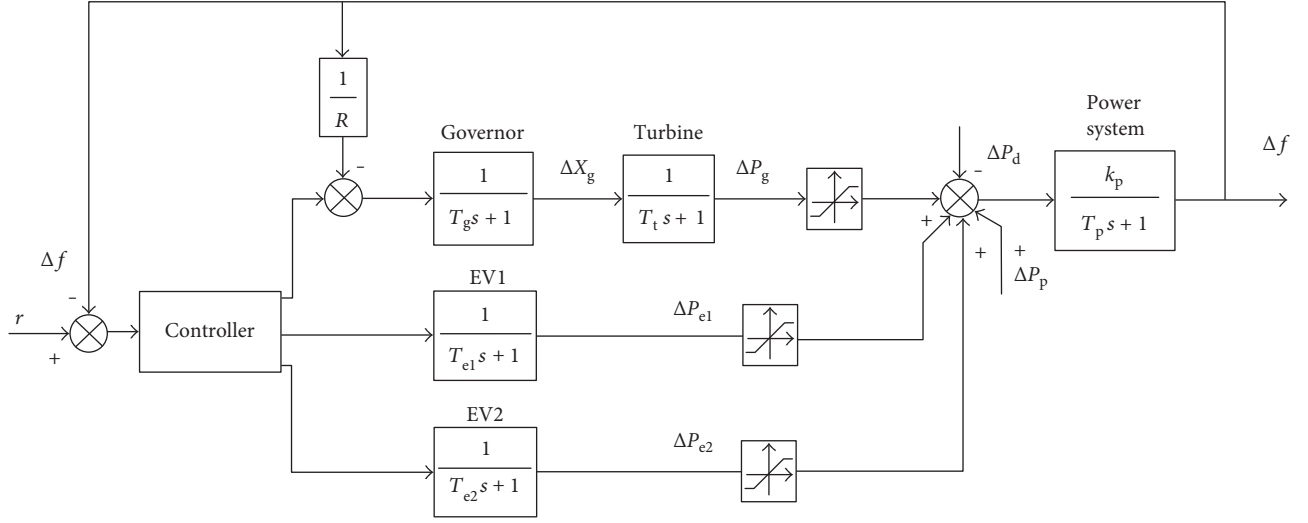


FIGURE 1: The schematic diagram of the benchmark system.

microgrid system with PV power integration, and a neural network observer is designed for an online observation of the PV power generation. Meanwhile, with the improvement of vehicle-to-grid (V2G) technique, EVs are also integrated into the microgrid as distributed storage devices to support the frequency regulation. The major contribution of this paper is as follows. First, an ISM controller for the microgrid with EVs is designed. Concerning the distinguished pattern of PV power generation, an online OISM controller is proposed to regulate the frequency of the microgrid, and the relevant stability proof is rigorously analyzed. Second, the robustness of the proposed controller against system parameter uncertainties are verified, where the control performance of this proposed method is compared with the traditional PID control.

This paper is organized as follows. Section 2 introduces the studied microgrid system and formulates the frequency control problem. Section 3 designs the neural network observer and further presents the OISM controller method. Simulation is carried out on the benchmark microgrid, and all the results are presented and analyzed in Section 4. Section 5 concludes this paper.

## 2. Problem Formulation

In this paper, the studied benchmark system includes the following general parts: an equivalent microturbine (MT), PV arrays, two equivalent EV models with battery banks, and a demand side such as smart homes and loads. Both island mode and grid-connected mode are the possible operation modes [19]. In this paper, this benchmark power system is considered as a microgrid and operated in an island mode, where the system power flow is balanced by local loads and local power generation. It means that MTs and PV arrays provide active power to balance all local loads, and EV stations can be considered as distributed battery energy storages to compensate the unbalance between power generation and load demand.

The power system is usually considered to be nonlinear and dynamic, but there only exists small load change during its normal operation. As EVs integrated into the benchmark system, the schematic diagram of the benchmark system is presented in Figure 1.

Since the microgrid is in the island operating mode, the LFC capacity is required to be adequate to quickly damp the frequency oscillation. By incorporating the EVs into the microgrid, the system inertia can be increased and the frequency stability can be improved [20, 21]. To demonstrate the benefit from the technology of V2G, an active power disturbance is added; the frequency dynamics with EVs and without EVs is shown in Figure 2.

The load frequency controller is expected to maintain the command frequency level when the load disturbances appear and renewable energy is incorporated into the grid. In order to formulate the LFC control problem of this microgrid, some mathematical notations are defined as follows:  $\Delta f$ ,  $\Delta P_t$ ,  $\Delta X_g$ ,  $\Delta P_{e1}$ , and  $\Delta P_{e2}$  are the change of the frequency, the turbine power, the governor position valve, the first EV power, and the second EV power, respectively.  $T_t$ ,  $T_g$ ,  $T_{e1}$ ,  $T_{e2}$ , and  $T_p$  are the time constants of the turbine, the governor, the first EV, the second EV, and the power system, respectively.  $k_p$  and  $R$  are the gain of the power system and the speed regulation coefficient, respectively.

Based on Figure 1, the state vector  $x(t)$  of the system is defined as

$$x(t) = [\Delta f(t), \Delta P_t(t), \Delta X_g(t), \Delta P_{e1}(t), \Delta P_{e2}(t)]^T, \quad (1)$$

and the LFC model is formulated by the following differential equation:

$$\dot{x}(t) = Ax(t) + Bu(t) + F(\Delta P_p(t) + \Delta P_d(t)). \quad (2)$$

The system matrix  $A$ , the control matrix  $B$ , and the disturbance matrix  $F$  can be expressed as

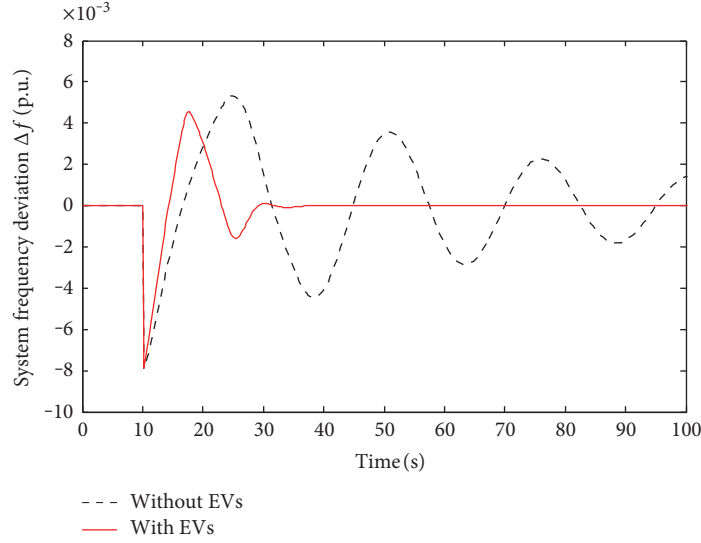


FIGURE 2: The frequency deviation with and without EVs.

$$A = \begin{bmatrix} -\frac{1}{T_p} & \frac{k_p}{T_p} & 0 & \frac{k_p}{T_p} & \frac{k_p}{T_p} \\ 0 & -\frac{1}{T_t} & \frac{1}{T_t} & 0 & 0 \\ -\frac{1}{RT_g} & 0 & -\frac{1}{T_g} & 0 & 0 \\ 0 & 0 & 0 & -\frac{1}{T_{e1}} & 0 \\ 0 & 0 & 0 & 0 & -\frac{1}{T_{e2}} \end{bmatrix},$$

$$B = \begin{bmatrix} 0 & 0 & 0 \\ 0 & 0 & 0 \\ \frac{1}{T_g} & 0 & 0 \\ 0 & \frac{1}{T_{e1}} & 0 \\ 0 & 0 & \frac{1}{T_{e2}} \end{bmatrix},$$

$$F = \begin{bmatrix} -\frac{k_p}{T_p} \\ 0 \\ 0 \\ 0 \\ 0 \end{bmatrix}.$$

$u(t)$  is the control vector,  $u(t) = [\Delta u_1(t), \Delta u_2(t), \Delta u_3(t)]^T$ , and  $\Delta P_d(t)$  and  $\Delta P_p(t)$  are the integrated disturbance from load change and the PV power, respectively. The following assumption is applied on the benchmark system.

*Assumption 1.* The induced norms of PV power disturbances and load change satisfy  $\|\Delta P_p(t)\| \leq \alpha_1$  and  $\|\Delta P_d(t)\| \leq \alpha_2$ , respectively, where  $\alpha_1 \geq 0$  and  $\alpha_2 \geq 0$  represent upper bounds.

### 3. Controller Design

*3.1. Integral Sliding Mode Controller.* Compared with a large interconnected system, the microgrid system is more unstable and easy to cause serious damage under parameter uncertainties and disturbances. Therefore, a controller with excellent robustness to maintain the microgrid system stable is required.

Sliding mode control is robust and systematic for matched disturbances and parameter variations [22–25]. To keep the frequency in the required level, ISM control is selected as the fundamental control method for the LFC problem of the benchmark system. For the microgrid system presented in (2), an ISM variable is designed as

$$s(t) = C_1 x(t) + \int_0^t C_2 x(t) dt, \quad (4)$$

where  $C_1 = [c_1, c_2, c_3, c_4, c_5]$  and  $C_2 = [c_6, c_7, c_8, c_9, c_{10}]$  are the coefficient vectors, and  $c_i$  meets that the two polynomials  $c_5 p^4 + c_4 p^3 + c_3 p^2 + c_2 p + c_1$  and  $c_{10} p^4 + c_9 p^3 + c_8 p^2 + c_7 p + c_6$  are Hurwitz.

The ISM controller is designed by adopting the reaching law  $\dot{s}(x) = -\varepsilon \text{sat}(s)$ . With the idea of equivalent control, the ISM frequency controller is constituted as

$$u(t) = -(C_1 B)^{-1} (C_1 A x(t) + C_2 x(t) + \varepsilon \text{sat}(s)), \quad (5)$$

where  $\varepsilon$  is the control gain and satisfies  $\varepsilon > |C_1 F(\alpha_1 + \alpha_2)|$  and  $\text{sat}(s) = s(t)/\rho$  is the saturation function to eliminate the chattering in the control signal by setting a reasonable width  $\rho$ .

*3.2. Neural Network Observer.* In this subsection, the data of the PV power is measured by specific sensors and is stored in the control unit. Recently, intelligent algorithms have been developed for obtaining information from data [26–31]. Therefore, these data are available to design an observer to forecast the future PV power. In this paper, a three-layer neural

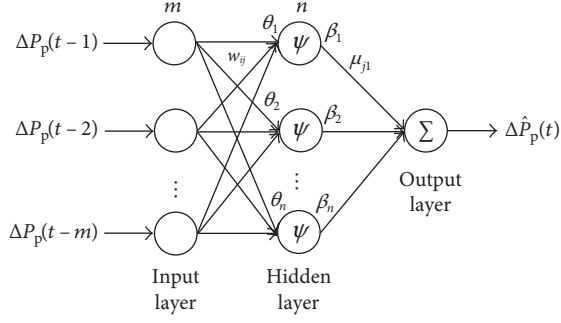


FIGURE 3: The structure of the neural network observer.

network with a hidden layer is used to realize the online observation of PV power, whose structure is shown in Figure 3.

From Figure 3, we can know that the neural network observer for the PV power is with  $m$  input-layer neurons,  $n$  hidden-layer neurons, and one output-layer neuron. Therefore, the inputs of the observer are  $m$  PV power values before time  $t$ , recorded as  $I_t \in R^{1 \times m}$ . The output  $\Delta P_p(t)$  is the PV power value at time  $t$ . The rest of the variables in Figure 3 can be defined as

$$\theta_j(t) = \sum_{i=1}^m w_{ij}(t) \Delta P_p(t-i), \quad (6)$$

$$\beta_j(t) = \psi(\theta_j(t)) = \frac{1 - e^{-\theta_j(t)}}{1 + e^{-\theta_j(t)}}, \quad (7)$$

$$\Delta \hat{P}_p(t) = \sum_{j=1}^n \mu_{j1}(t) \beta_j(t), \quad (8)$$

where  $i$  and  $j$  satisfy  $i = 1, \dots, m$  and  $j = 1, \dots, n$ , respectively.  $\theta_j(t)$  and  $\beta_j(t)$  are input and output values of the  $j$ th hidden neuron, respectively.  $w_{ij}(t)$  is the weight from the  $i$ th input neuron to the  $j$ th hidden neuron, and  $\mu_{j1}(t)$  is the weights from the  $j$ th hidden node to the output node.  $\psi(z) = (1 - e^{-z}) / (1 + e^{-z})$  is used as the activation function.

The weight vectors  $w_{ij}(t)$  and  $\mu_{j1}(t)$  are randomly initialized in  $[-1, 1]$ . According to the calculation of forward propagation, the neural network outputs  $\Delta \hat{P}_p(t)$  as the estimation value of PV power at time  $t$ .

The weights of the neural network are updated by the error back-propagation algorithm. The difference between  $\Delta \hat{P}_p(t)$  and the measured real value of PV power is defined as the network error, which is

$$e_p(t) = \Delta P_p(t) - \Delta \hat{P}_p(t). \quad (9)$$

If  $e_p(t) = 0$ , it represents the estimated PV power value which is completely equal to the real PV power value. In the back-propagation process, the aim is to minimize the objective function  $E(t)$  associated with  $e_p(t)$ ; that is,

$$E(t) = \frac{1}{2} e_p^2(t). \quad (10)$$

TABLE 1: The system parameters of the benchmark system.

Parameters	$T_t$	$T_g$	$T_{e1}$	$T_{e2}$	$T_p$	$k_p$	$R$
Values	10	0.1	1	1	10	1	0.5

TABLE 2: The disturbance from load change.

Time (s)	15	60	100	150
Disturbance (p.u.)	+0.2	-0.2	-0.4	+0.4

The gradient descent method is used to update the weights of the neural network observer in the back-propagation [26–28, 32]. Define the input-to-hidden weight vector  $w_1(t)$  and the hidden-to-output weight vector  $w_2(t)$  as

$$\begin{aligned} w_1(t) &= \{w_{ij}(t) | i = 1, 2, \dots, m, j = 1, 2, \dots, n\}, \\ w_2(t) &= \{\mu_{j1}(t) | j = 1, 2, \dots, n\}, \end{aligned} \quad (11)$$

where  $w_1(t) \in R^{m \times n}$  and  $w_2(t) \in R^{n \times 1}$ , respectively. Then (8) can be further simplified as

$$\Delta \hat{P}_p(t) = \sum_{j=1}^n \mu_{j1}(t) \psi \left( \sum_{i=1}^m w_{ij}(t) \Delta P_p(t-i) \right) = w_2(t) \psi(w_1). \quad (12)$$

According to the chain derivation rule, the weights of the neural network observer are updated by

$$\dot{w}_2(t) = -\tau \frac{\partial E(t)}{\partial \Delta \hat{P}_p(t)} \frac{\partial \Delta \hat{P}_p(t)}{\partial w_2(t)} = \tau e_p(t) \psi(w_1). \quad (13)$$

Specifically, the weights  $w_{ij}(t)$  and  $\mu_{j1}(t)$  are regulated by

$$\dot{w}_{ij}(t) = -\tau \frac{\partial E(t)}{\partial \Delta \hat{P}_p(t)} \frac{\partial \Delta \hat{P}_p(t)}{\partial \alpha_j(t)} \frac{\partial \alpha_j(t)}{\partial \theta_j(t)} \frac{\partial \theta_j(t)}{\partial w_{ij}(t)}, \quad (14)$$

$$\dot{\mu}_{j1}(t) = -\tau \frac{\partial E(t)}{\partial \Delta \hat{P}_p(t)} \frac{\partial \Delta \hat{P}_p(t)}{\partial \mu_{j1}(t)}, \quad (15)$$

where  $\tau > 0$  is the learning rate. The estimated PV power can be used as an input signal into the ISM controller to eliminate the influence of integrated PV power.

**3.3. Observer-Based Integral Sliding Mode Controller.** According to the universal approximation property of neural networks [32, 33], the output of the observer can approximate the real PV power with an allowable error. In other words, there exists a weight vector  $w$  to make the error  $e_p(t)$  reach the minimum, which is

$$|e_p(t)| \leq \xi, \quad (16)$$

where  $\xi$  is an arbitrary enough small positive constant. It represents the maximal absolute difference between the

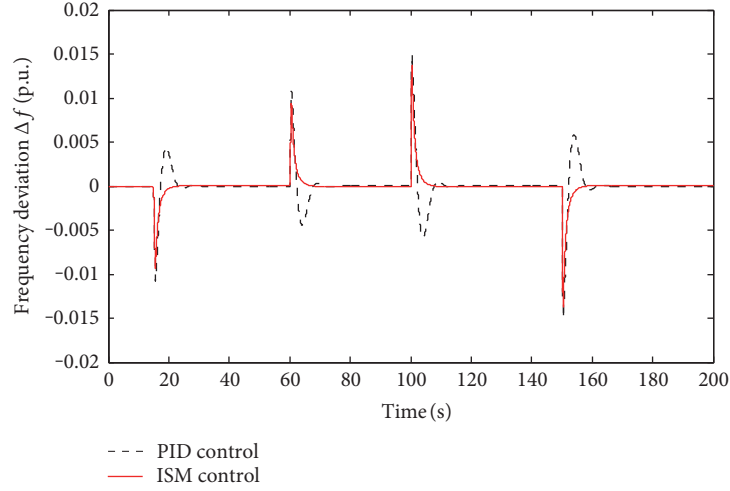


FIGURE 4: The frequency deviation without power output constraints.

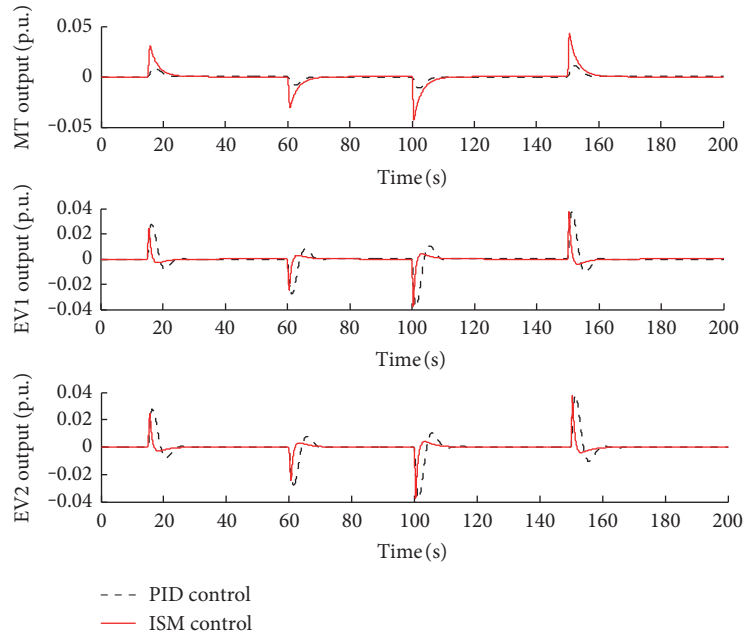


FIGURE 5: The output power of MT and EVs without power output constraints.

estimated value and the real PV power. By introducing the neural network observer, the OISM controller is constructed for the microgrid system with PV power integration. Thus, we have the following theorem.

**Theorem 1.** For system (1), if the weights of the neural network observer are updated by (13), and the OISM controller is designed as

$$\mu(t) = -(C_1 B)^{-1} (C_1 A x(t) + C_2 x(t) + \varepsilon \text{sat}(s) + C_1 F \Delta \hat{P}_p(t)), \quad (17)$$

then the microgrid system is asymptotically stable.

*Proof.* We define the Lyapunov function for system (1) with control law (17) as

$$V(t) = \frac{1}{2} s^2(t) + \frac{1}{2\tau} \tilde{w}_2^2(t). \quad (18)$$

It is obvious that  $V(t) \geq 0$ . Set the weight error vector as

$$\tilde{w}_2(t) = w_2^*(t) - w_2(t), \quad (19)$$

where  $w_2^*(t)$  is the ideal weight vector and  $w_2(t)$  is actually weight vector in the observer. By differentiating  $\tilde{w}_2(t)$  with respect to time  $t$ , we could obtain

$$\dot{\tilde{w}}_2(t) = -\dot{w}_2(t). \quad (20)$$

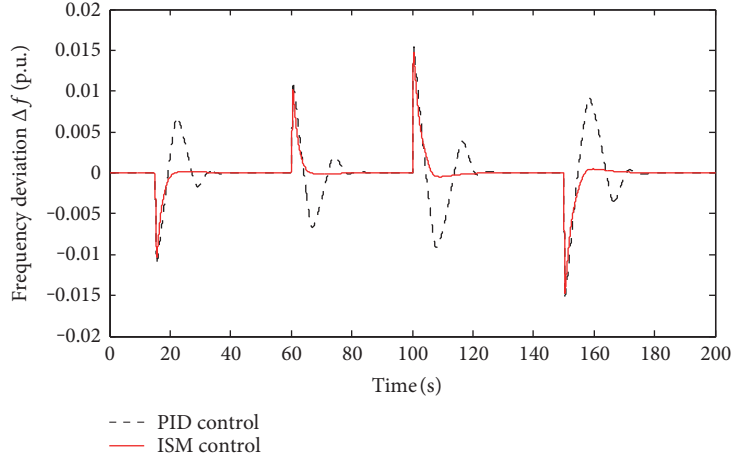


FIGURE 6: The frequency deviation with power output constraints.

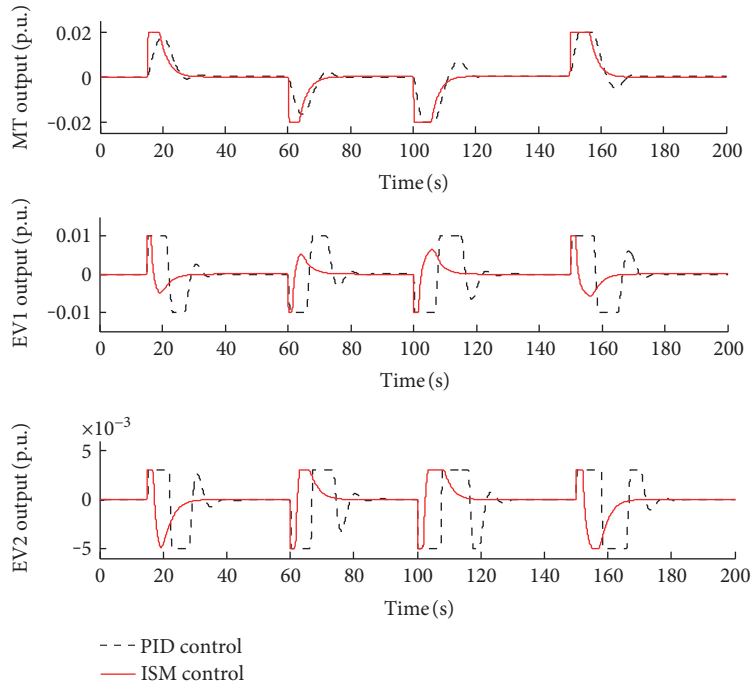


FIGURE 7: The output power of MT and EVs with power output constraints.

TABLE 3: The sum of frequency deviation.

Condition	PID	ISM	PID + constraints	ISM + constraints
$E_{iae}$	0.1309	0.066	0.3251	0.1212

By combining with (20), the derivative of  $V(t)$  can be obtained as

$$\begin{aligned}\dot{V}(t) &= s(t)\dot{s}(t) + \tau^{-1}\tilde{w}_2(t)\dot{\tilde{w}}_2(t) \\ &= s(t)\dot{s}(t) - \tau^{-1}\tilde{w}_2(t)\dot{w}_2(t).\end{aligned}\quad (21)$$

According to (2) and (4), then  $\dot{V}(t)$  can be deduced as

$$\dot{V}(t) = s(t)(C_1\dot{x}(t) + C_2x(t)) - \tau^{-1}\tilde{w}_2(t)\dot{w}_2(t). \quad (22)$$

The weights of the neural network observer are updated according to (13); then  $\dot{V}(t)$  can be derived as

$$\begin{aligned}\dot{V}(t) &= s(t)(C_1Ax(t) + (-C_1Ax(t) - C_2x(t) - \varepsilon\text{sat}(s) - C_1F\Delta\hat{P}_s(t)) \\ &\quad + C_1F(\Delta P_s(t) + \Delta P_d(t)) + C_2x(t)) \\ &\quad + \tau^{-1}\tilde{w}_2(t)\dot{w}_2(t).\end{aligned}\quad (23)$$

We simplify (23) and substitute  $\tilde{w}_2(t) = w_2^*(t) - w_2(t)$ ; then  $\dot{V}(t)$  becomes

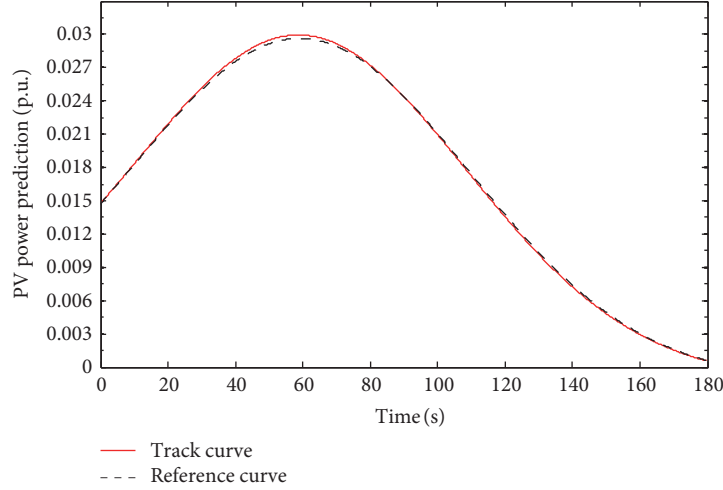


FIGURE 8: The predictive PV power by the neural network observer.

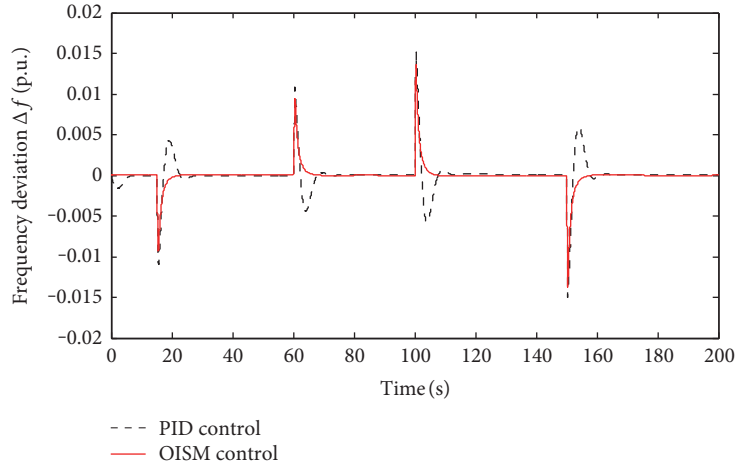


FIGURE 9: The frequency performance without power output constraints.

$$\begin{aligned} \dot{V}(t) = & s(t)(-\varepsilon \text{sat}(s) + C_1 F(e_p(t) + \Delta P_d(t))) \\ & - (w_2^* - w_2)(t) \psi(w_1(t) I_t) e_p(t). \end{aligned} \quad (24)$$

According to the universal approximation property of neural network and *Assumption 1*, that is,  $|e_p(t)| < \xi$ ,  $|\Delta P_p(t)| \leq \alpha_1$ , and  $|\Delta P_d(t)| \leq \alpha_2$ , then we can obtain that the sliding mode gain  $\varepsilon$  is required to satisfy

$$\varepsilon \geq |C_1 F(\alpha_1 + \alpha_2)|. \quad (25)$$

After a sufficient learning, the error of the neural network observer is reasonable to be small enough, which means  $\xi \leq \alpha_1$ . Therefore, it is easy to deduce

$$-\varepsilon \leq C_1 F(e_p(t) + \Delta P_d(t)) \leq \varepsilon. \quad (26)$$

With  $w_2^* \psi(w_1) = \Delta P_p(t)$  and  $w_2 \psi(w_1) = \Delta \hat{P}_p(t)$ , therefore we have the following:

$$\dot{V}(t) = s(t)(-\varepsilon \text{sat}(s) + C_1 F(e_p(t) + \Delta P_d(t))) - e_p^2(t). \quad (27)$$

It means

$$\dot{V}(t) \leq -e_p^2(t) \quad (28)$$

for both  $s(t) > 0$  and  $s(t) < 0$ .

Observing inequalities (18) and (28), controller (17) can ensure  $V(t) \geq 0$  and  $\dot{V}(t) \leq 0$  for system (1). According to the Lyapunov stability theorem, system (1) is asymptotically stable. It means the frequency derivation of system (1) is regulated to zero under the designed OISM controller.

#### 4. Simulation and Analysis

In this section, we apply the proposed frequency control method to the studied benchmark microgrid, which is a typical benchmark system. The parameters of a benchmark

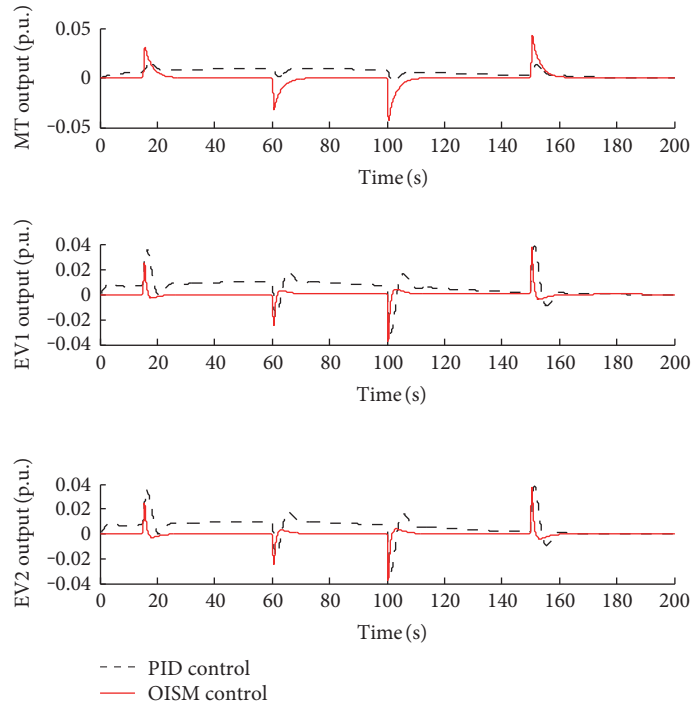


FIGURE 10: The output power of MT and EVs without power output constraints.

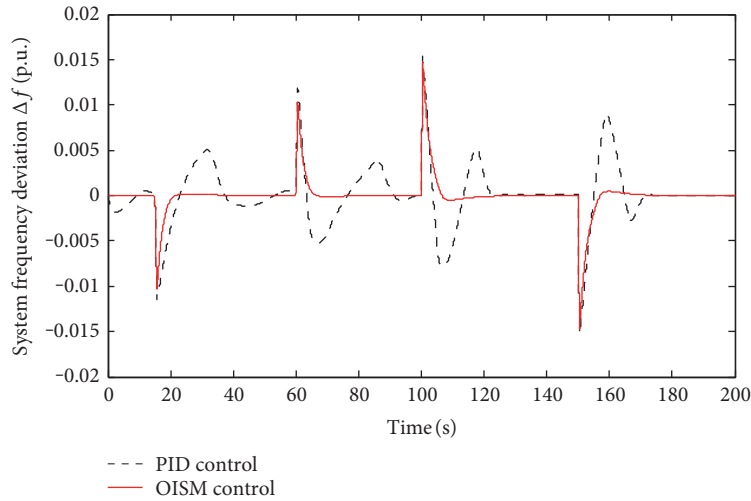


FIGURE 11: The frequency performance with power output constraints.

microgrid system are given in Table 1 by referring to [19, 34, 35]. The PID controller is also used to damp the frequency deviation of the benchmark system as a competitive method.

In the PID controller, it takes the frequency deviation  $\Delta f(t)$  as the input, and the parameters of proportional, integral, and derivative gains are set as  $K_p = 4$ ,  $K_i = 1$ , and  $K_d = 0.6$ , respectively. For the proposed ISM control method, the control gain is  $\varepsilon = 10$ , and the coefficient vectors  $C_1$  and  $C_2$  are defined as  $C_1 = [0.65, 0.05, 0.05, 0.05, 0.05]$  and  $C_2 = [0.15, 0.01, 0.01, 0.01, 0.01]$ , respectively. In order to

validate the performance of designed controllers, we have the following cases.

*4.1. Dynamic Response for Load Change.* In this case, the frequency of the microgrid system is initially stable; four sequential active power disturbances caused by load change are applied to the microgrid system, which is shown in Table 2. Without integrating the PV power, the ISM controller in (5) is used to suppress the frequency oscillation.

When these sequential disturbances are added on the system, the performance of the integral sliding mode controller

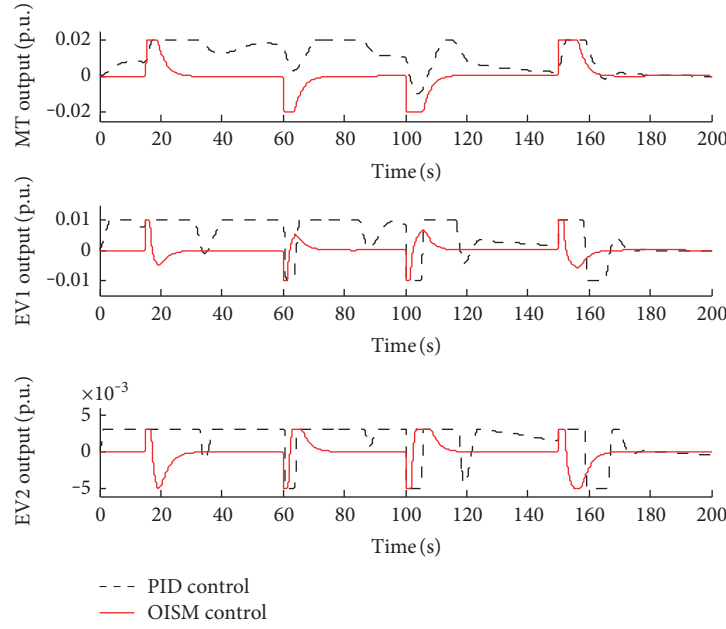


FIGURE 12: The frequency performance with power output constraints.

TABLE 4: The sum of frequency deviation.

	PID	OISM	PID + constraints	OISM + constraints
$E_{iae}$	0.1459	0.0679	0.4102	0.1230

is presented in Figure 4. As a competitive result, the regulation result of PID controller is also presented in Figure 4. The power outputs of MT and EVs are shown in Figure 5.

**4.2. Dynamic Response to Load Disturbances and Power Output Constraints.** Consider the output power limits of MT and two EVs as [36]. The output power values of MT and two EVs have output limits which are  $[-0.02, +0.02]$ ,  $[-0.01, +0.01]$ , and  $[-0.005, +0.003]$  for the output power ranges of MT, EV1, and EV2, respectively. The same disturbances given in Table 2 are added on this benchmark system. In this case, the performance of system frequency deviation is shown in Figure 6, including the PID control and the ISM control. The outputs of MT and EVs are shown in Figure 7.

From Figures 4 and 6, we can observe that every disturbance generates an obvious frequency deviation from the prescribed value, and the deviation depends on the amplitude of disturbance. Compared with the PID controller, the ISM controller has a faster response ability as well as smaller transient amplitudes. Moreover, without the power output constraints, the regulation of both PID and ISM controller has better performance than the two controllers under the condition of power output constraints. Figures 5 and 7 show the power outputs of MT and EVs without and with constraints.

The performance index based on the integral value of total frequency deviation in the whole regulation process is defined as

$$E_{iae} = \int_0^t |\Delta f| dt. \quad (29)$$

For the above two cases, the performance indexes of two controllers are presented in Table 3. Comparatively speaking, the ISM controller has a better regulation ability than the PID control.

**4.3. Dynamic Response to Both Load Disturbances and PV Power.** In this case, the PV power is integrated into the microgrid system based on case 1. The PV power and four sequential power disturbances are all applied to the microgrid. Specifically, four sequential power disturbances from load changes are given in Table 2.

The parameters of PID controller and ISM controller are the same as the values in case 1. In order to eliminate the impact of PV power, we change the ISM controller to the OISM controller, which is designed in (17). The parameters of the neural network observer are set as follows: input layer nodes  $m = 35$ , hidden layer nodes  $n = 6$ , and the learning rate  $\tau = 0.01$ . It means that the neural network learns from 35 previous values before time  $t$  and then estimates the PV power at time  $t$ . The output of the neural network observer is shown in Figure 8, compared with the real PV power. From Figure 8, we can know that the neural network observer is able to predict the PV power well by learning the previous PV power data.

After integrating the PV power into the system and applying these sequential disturbances, the system frequency deviation curves with PID controller and OISM controller are presented in Figure 9, and the output power of MT and EVs are shown in Figure 10.

*4.4. Dynamic Response to Load Disturbances, PV Power, and Power Output Constraints.* Considering the output power limits of MT and two EVs, the output constraints of MT and EVs use the same settings as case 2. The applied disturbances are also shown in Table 2. By using the OISM controller, the system frequency deviation is shown in Figure 11, and the outputs of MT and EVs are shown in Figure 12. The performance of PID controller has been provided as the comparison.

From Figures 9 and 11, the frequency deviates from the command value under the disturbances from PV power and load change. However, the OISM controller is more effective than the PID controller, which can provide the control performance with faster regulation and smaller oscillation in the whole regulation process. From Figures 10 and 12, we can know that the PID controller hardly adjusts the deviation of the output power to zero; it means that the frequency is difficult to be regulated to the specified value. Comparing the control performance with the PID controller, the OISM controller still keeps fast regulation and strong robustness with an observed PV power. Similar to case 2, the performance of the PID controller becomes worse when the output power is constrained. From Figures 11 and 12, we can observe that it is hard for the PID controller to regulate the frequency to the required value under disturbances. On the contrary, the OISM controller still has a superior damping performance.

The performance index  $E_{iae}$  is also used to evaluate the control performance. The index values of the controllers are presented in Table 4. It can be seen that the performance of the OISM controller is obviously better than that of the PID controller for the whole regulation process.

## 5. Conclusions

This paper has addressed the LFC problem for the island microgrid with EVs and PV power integration. The OISM control strategy is adopted to regulate the frequency derivation, where the neural network observer is designed to predict the PV power disturbance. The theoretical analysis is presented for the OISM system in the sense of Lyapunov stability. Simulations have been executed on a benchmark system with different conditions, including load change, PV disturbances, and power output limits. Comparative studies with the PID controller are provided to demonstrate the superior performance of the OISM controller. In the future work, there are several significant topics that need to be intensively addressed. For example, integrating the diversified sources of energy into the island microgrid will be considered. Also, we will consider the coordination control of diversified energies and the frequency stability of interconnected microgrids.

## Conflicts of Interest

The authors declare that they have no conflicts of interest.

## Acknowledgments

This work was supported in part by the National Natural Science Foundation under Grants 51377065, 61304018, 61301035, and 6141130160, in part by Hubei Province Science and Technology Supporting Program under Grant 2014BAA035, and in part by Tianjin Natural Science Foundation under Grant 14JCQNJC05400.

## References

- [1] J. A. P. Lopes, F. J. Soares, and P. M. R. Almeida, "Integration of electric vehicles in the electric power system," *Proceedings of the IEEE*, vol. 99, no. 1, pp. 168–183, 2011.
- [2] Y. Lei, W. Xu, C. Mu, Z. Zhao, H. Li, and Z. Li, "New hybrid damping strategy for grid-connected photovoltaic inverter with LCL filter," *IEEE Transactions on Applied Superconductivity*, vol. 24, no. 5, pp. 1–8, 2014.
- [3] C. Mu, Y. Tang, and H. He, "Observer-based sliding mode frequency control for micro-grid with photovoltaic energy integration," *2016 IEEE Power and Energy Society General Meeting (PESGM)*, pp. 1–5, 2016.
- [4] C. T. Pan and C. M. Liaw, "An adaptive controller for power system load-frequency control," *IEEE Transactions on Power Systems*, vol. 4, no. 1, pp. 122–128, 1989.
- [5] X. Li, Y.-J. Song, and S.-B. Han, "Frequency control in micro-grid power system combined with electrolyzer system and fuzzy PI controller," *Journal of Power Sources*, vol. 180, no. 1, pp. 468–475, 2008.
- [6] I. Kamwa, R. Grondin, and Y. Hebert, "Wide-area measurement based stabilizing control of large power systems—a decentralized/hierarchical approach," *IEEE Transactions on Power Systems*, vol. 16, no. 1, pp. 136–153, 2001.
- [7] P. Kundur, *Power System Stability and Control*, McGraw-Hill Education, New York, 1st edition, 1994.
- [8] Y. Tang, J. Yang, J. Yan, and H. He, "Intelligent load frequency controller using GrADP for island smart grid with electric vehicles and renewable resources," *Neurocomputing*, vol. 170, pp. 406–416, 2015.
- [9] M. H. Ali, T. Murata, and J. Tamura, "Transient stability enhancement by fuzzy logic-controlled SMES considering coordination with optimal reclosing of circuit breakers," *IEEE Transactions on Power Systems*, vol. 23, no. 2, pp. 631–640, 2008.
- [10] E. Cam and I. Kocaarslan, "Load frequency control in two area power systems using fuzzy logic controller," *Energy Conversion and Management*, vol. 46, no. 2, pp. 233–243, 2005.
- [11] I. Kocaarslan and E. Cam, "Fuzzy logic controller in interconnected electrical power systems for load-frequency control," *International Journal of Electrical Power & Energy Systems*, vol. 27, no. 8, pp. 542–549, 2005.
- [12] M. Zribi, M. Al-Rashed, and M. Alrifai, "Adaptive decentralized load frequency control of multi-area power systems," *International Journal of Electrical Power & Energy Systems*, vol. 27, no. 8, pp. 575–583, 2005.
- [13] A. Rubaai and V. Udo, "An adaptive control scheme for load-frequency control of multiarea power systems part I.

- Identification and functional design,” *Electric Power Systems Research*, vol. 24, no. 3, pp. 183–188, 1992.
- [14] S. Vachirasricirikul and I. Ngamroo, “Robust LFC in a smart grid with wind power penetration by coordinated V2G control and frequency controller,” *IEEE Transactions on Smart Grid*, vol. 5, no. 1, pp. 371–380, 2014.
- [15] S. Saxena and Y. V. Hote, “Load frequency control in power systems via internal model control scheme and model-order reduction,” *IEEE Transactions on Power Systems*, vol. 28, no. 3, pp. 2749–2757, 2013.
- [16] X. Liu, X. Kong, and K. Y. Lee, “Distributed model predictive control for load frequency control with dynamic fuzzy valve position modelling for hydro-thermal power system,” *IET Control Theory and Applications*, vol. 10, no. 14, pp. 1653–1664, 2016.
- [17] K. Vrdoljak, N. Peric, and I. Petrovic, “Sliding mode based load-frequency control in power systems,” *Electric Power Systems Research*, vol. 80, no. 5, pp. 514–527, 2010.
- [18] Y. Tang, C. Mu, and H. He, “SMES-based damping controller design using fuzzy-GrHDP considering transmission delay,” *IEEE Transactions on Applied Superconductivity*, vol. 26, no. 7, pp. 1–6, 2016.
- [19] D. Qian, S. Tong, H. Liu, and X. Liu, “Load frequency control by neural-network-based integral sliding mode for nonlinear power systems with wind turbines,” *Neurocomputing*, vol. 173, Part 3, pp. 875–885, 2016.
- [20] S. D. G. Jayasinghe, D. M. Vilathgamuwa, and U. K. Madawala, “Direct integration of battery energy storage systems in distributed power generation,” *IEEE Transactions on Energy Conversion*, vol. 26, no. 2, pp. 677–685, 2011.
- [21] L. A. de Souza Ribeiro, O. R. Saavedra, S. L. de Lima, and J. G. de Matos, “Isolated microgrids with renewable hybrid generation: the case of Lencois Island,” *IEEE Transactions on Sustainable Energy*, vol. 2, no. 1, pp. 1–11, 2011.
- [22] B. Bandyopadhyay, F. Deepak, and K.-S. Kim, *Sliding Mode Control Using Novel Sliding Surfaces*, Springer-Verlag, Berlin Heidelberg, 2009.
- [23] V. I. Utkin, *Sliding Modes in Control and Optimization*, Springer-Verlag, Berlin Heidelberg, 1992.
- [24] C. Mu, W. Xu, and C. Sun, “On switching manifold design for terminal sliding mode control,” *Journal of the Franklin Institute*, vol. 353, no. 7, pp. 1553–1572, 2016.
- [25] C. Mu, Z. Ni, C. Sun, and H. He, “Air-breathing hypersonic vehicle tracking control based on adaptive dynamic programming,” *IEEE Transactions on Neural Networks and Learning Systems*, vol. 28, no. 3, pp. 584–598, 2017.
- [26] L. Cheng, Z.-G. Hou, and M. Tan, “Adaptive neural network tracking control for manipulators with uncertain kinematics, dynamics and actuator model,” *Automatica*, vol. 45, no. 10, pp. 2312–2318, 2009.
- [27] D. Wang, D. Liu, C. Mu, and H. Ma, “Decentralized guaranteed cost control of interconnected systems with uncertainties: a learning-based optimal control strategy,” *Neurocomputing*, vol. 214, pp. 297–306, 2016.
- [28] D. Wang, C. Li, D. Liu, and C. Mu, “Data-based robust optimal control of continuous-time affine nonlinear systems with matched uncertainties,” *Information Sciences*, vol. 366, pp. 121–133, 2016.
- [29] B. Gu, V. S. Sheng, K. Y. Tay, W. Romano, and S. Li, “Incremental support vector learning for ordinal regression,” *IEEE Transactions on Neural Networks and Learning Systems*, vol. 26, no. 7, pp. 1403–1416, 2015.
- [30] B. Gu, V. S. Sheng, Z. Wang, D. Ho, S. Osman, and S. Li, “Incremental learning for v-support vector regression,” *Neural Networks*, vol. 67, pp. 140–150, 2015.
- [31] B. Gu, X. Sun, and V. S. Sheng, “Structural minimax probability machine,” *IEEE Transactions on Neural Networks and Learning Systems*, 2016, in press.
- [32] D. Wang, C. Mu, and D. Liu, “Data-driven nonlinear near-optimal regulation based on iterative neural dynamic programming,” *Acta Automatica Sinica*, vol. 43, no. 3, pp. 366–375, 2017.
- [33] K. Hornik, “Approximation capabilities of multilayer feedforward networks,” *Neural Networks*, vol. 4, no. 2, pp. 251–257, 1991.
- [34] Y. Mi, Y. Fu, C. Wang, and P. Wang, “Decentralized sliding mode load frequency control for multi-area power systems,” *IEEE Transactions on Power Systems*, vol. 28, no. 4, pp. 4301–4309, 2013.
- [35] C. Wang, Y. Mi, Y. Fu, and P. Wang, “Frequency control of an isolated micro-grid using double sliding mode controllers and disturbance observer,” *IEEE Transactions on Smart Grid*, 2016, in press.
- [36] J. Yang, Z. Zeng, Y. Tang, J. Yan, H. He, and Y. Wu, “Load frequency control in isolated micro-grids with electrical vehicles based on multivariable generalized predictive theory,” *Energies*, vol. 8, no. 3, pp. 2145–2164, 2015.

## Research Article

# PV-Powered CoMP-Based Green Cellular Networks with a Standby Grid Supply

Abu Jahid,<sup>1</sup> Abdullah Bin Shams,<sup>2</sup> and Md. Farhad Hossain<sup>3</sup>

<sup>1</sup>Department of Electrical, Electronic and Communication Engineering, Military Institute of Science and Technology, Dhaka 1216, Bangladesh

<sup>2</sup>Department of Electrical and Electronic Engineering, Islamic University of Technology, Gazipur 1704, Bangladesh

<sup>3</sup>Department of Electrical and Electronic Engineering, Bangladesh University of Engineering and Technology, Dhaka 1000, Bangladesh

Correspondence should be addressed to Md. Farhad Hossain; mfarhadhossain@eee.buet.ac.bd

Received 14 December 2016; Accepted 13 February 2017; Published 4 April 2017

Academic Editor: Md. Rabiul Islam

Copyright © 2017 Abu Jahid et al. This is an open access article distributed under the Creative Commons Attribution License, which permits unrestricted use, distribution, and reproduction in any medium, provided the original work is properly cited.

This paper proposes a novel framework for PV-powered cellular networks with a standby grid supply and an essential energy management technique for achieving envisaged green networks. The proposal considers an emerging cellular network architecture employing two types of coordinated multipoint (CoMP) transmission techniques for serving the subscribers. Under the proposed framework, each base station (BS) is powered by an individual PV solar energy module having an independent storage device. BSs are also connected to the conventional grid supply for meeting additional energy demand. We also propose a dynamic inter-BS solar energy sharing policy through a transmission line for further greening the proposed network by minimizing the consumption from the grid supply. An extensive simulation-based study in the downlink of a Long-Term Evolution (LTE) cellular system is carried out for evaluating the energy efficiency performance of the proposed framework. System performance is also investigated for identifying the impact of various system parameters including storage factor, storage capacity, solar generation capacity, transmission line loss, and different CoMP techniques.

## 1. Introduction

Due to the recent unprecedented growth in the number of subscribers and diverse data applications, mobile cellular network operators are deploying a higher number of BS in their infrastructure resulting in an exponential increase in energy consumption. Such growth of energy demand in the cellular network industry is exerting enormous detrimental effect on both the economical and the environmental aspects [1–3]. Recent studies suggest that around 50% of the operating expenditure (OPEX) of a cellular system attributes to the energy cost for running the network. On the other hand, it has been reported that the information and communication technology (ICT) industry contributes about 2–2.5% of total carbon emissions and this is expected to increase every year

with the exponential growth of mobile traffic [4, 5]. Moreover, this increased energy consumption in cellular networks places heavy burden on the electric grid. Therefore, with the escalating awareness of global warming and energy costs for operating cellular networks, green communications have received considerable attention among the telecommunication researchers and have led to an emerging trend to improve the energy efficiency (EE) of the overall system [4, 6]. Powering the cellular networks as much as possible by renewable energy sources is potentially the best alternative for reducing and even completely phasing out the consumption from the conventional grid supply leading to improved EE and decreased carbon footprint. The most popular among the renewable energy sources are solar, wind, and hydropower. A step towards green communication requires the renewable

energy source to be easily integratable with the existing cellular networks. It must also be economical, widely available, and modular and should occupy a smaller area so that it can easily be installed at the vicinity of the BSs. From this perspective, the most feasible and lucrative renewable energy source is photovoltaic (PV) cells.

*1.1. Photovoltaic Power Plants.* As an efficient way to utilize solar energy, PV power plant has received increased attention all over the world due to the fossil fuel crisis and its associated environmental pollution. The tremendous growth of energy consumption around the world has led to an increase in operating cost and global warming. Solar energy offers attractive solutions to reduce carbon footprints and mitigate the global climate change. Burning of nonrenewable energy sources like fossil fuel produces greenhouse gases, whereas PV-based power plants and industries have no such detrimental effect on the environment. Since renewable solar energy is derived from resources which are regenerative, it does not emit carbon. In accordance with the growing trend of PV power plant, solar energy can also be used for a variety of purposes, such as solar-powered BSs for green communications, solar irrigation, solar cold storage, and solar boat systems [7]. Many emerging economies [7–9] have an excellent solar resource and have adopted policies to encourage the development of the solar industry to realize the benefits of PV technology. This can generate positive impact on their economies, as well as on the local and global environment, and improve energy security. Chandel et al. [8] analyzed the potential and cost-effectiveness of solar PV power plant of 2.5 MW for meeting the energy demand of the garment zone in India. A viability analysis [9] of 1 MW PV power plants was conducted in Serbia by taking different types of solar modules to find out the best possibilities of generating high electricity.

*1.2. PV Solar Energy for Green Communications.* BSs in the radio access network (RAN) of cellular mobile networks are the most energy hungry equipment amounting around 60%–80% of the total consumption [10–12], whereas the accumulated energy requirement for user equipment (UE) is around 1% [13]. On the other hand, cellular network data traffic is expected to increase approximately by a factor of ten every five years resulting in a tremendous pressure on energy demand [14]. Thus, this unprecedented growth in energy consumption exerts a detrimental impact on the environment in terms of carbon footprints [4, 5, 15]. Therefore, energy-efficient resource management system in RANs has become the center of focus of the researchers from both academia and industry. This trend has motivated the interest of researchers in an innovative research area called “green communications” concentrating on the environmental effects of cellular networks.

Being inspired for curving down the energy costs, telecom operators have started the deployment of renewable energy sources, such as solar panels, for improving EE of RAN infrastructure. The objective of green cellular communications is to reduce the overall nonrenewable energy consumption leading to improved EE and higher economic benefits.

Conventional design approaches focus on optimizing the quality of service (QoS) parameters such as cell coverage, capacity, and throughput with no consideration on the EE aspect of cellular networks. However, with the introduction of green communication paradigm, designed networks must also maintain the same level of QoS while improving EE [11, 16]. On the other hand, the intermittency and spatial randomness of renewable energy generation can severely degrade the system performance of large-scale cellular networks, and hence, it is a fundamental design issue to utilize the harvested energy to sustain traffic demands of users in the network [17]. As a consequence, though renewable energy sources are being deployed in BSs, a provision of conventional grid energy is still required to mitigate for the variability of the renewable energy generation.

Considering the aforementioned concerns, envisioning BSs to be powered by hybrid supplies combining solar energy sources with on-grid sources has become a promising alternative stimulating the proposed work in this paper. In such cellular networks, the primary energy source for BSs is the solar energy. If enough green energy is not available, BSs draw energy from the grid supply for serving its associated UEs. The focus of such green networking is to maximize the usage of solar energy while minimizing the conventional grid energy utilization. The optimal use of solar energy over a period of time depends on the proper energy management techniques integrated into the network operation.

*1.3. Coordinated Multipoint (CoMP) Transmission Technique.* Spectral efficiency (SE) and EE are considered as the prime performance metrics for planning and operation of next-generation cellular networks. SE is a key performance parameter defined as the overall throughput per unit bandwidth. On the other hand, coordinated multipoint (CoMP) transmission has been widely discussed as a promising candidate for future LTE-Advanced (LTE-A) cellular systems [18, 19]. In a cellular network with CoMP, multiple BSs coordinate among themselves for serving a UE in the best possible way. Thus, CoMP has the potential to improve the network performance in terms of interference management, cell-edge throughput, and overall SE as well as EE [20–22]. The downlink CoMP can be categorized into three types based on data availability at multipoint: joint transmission (JT), dynamic point selection (DPS), and coordinated scheduling/coordinated beamforming (CS/CB), which are outlined by 3GPP [20, 23]. In the DPS technique, BS offering the highest SINR is dynamically selected for serving a UE. In contrast, under the JT technique, multiple coordinating BSs transmit data simultaneously to a UE. On the other hand, in the CS/CB technique, signal is transmitted from only one BS by employing beamforming, which is achieved through proper scheduling among the coordinated BSs for avoiding intercell interference.

*1.4. Contributions.* This paper proposes and explores the potential of different approaches for improving the EE

of CoMP transmission-based future cellular networks. The main contributions of this paper can be summarized as follows:

- (i) This paper proposes a novel framework for improving the EE of the CoMP-based next-generation cellular networks by employing a hybrid power supply for BSs. Under the proposed framework, PV solar modules work as the primary energy source, while conventional grid power is proposed as the standby source for running BSs in case of insufficient solar energy for serving the UEs with no interruption. The proposed hybrid energy usage scheme is then investigated for both DPS and JT CoMP transmission technique-based cellular networks, which has not been reported yet in literature.
- (ii) Then, a technique for maximizing the green energy utilization (i.e., minimizing the consumption from a conventional grid supply) is developed, while BSs are still powered by hybrid sources with the proposed energy usage scheme as outlined above. Therefore, a heuristic policy for sharing green energy (i.e., solar) among the BSs is proposed. For enabling the inter-BS energy transfer, neighboring BSs are proposed to be connected through a resistive lossy transmission line. The proposed energy sharing scheme is also integrated in and investigated for both the DPS and the JT CoMP-based cellular networks. To the best of our knowledge, we are the first to propose a green energy sharing technique for CoMP-based cellular systems.
- (iii) Tempo-spatial cellular traffic diversity as well as solar energy generation variability plays a significant role in developing effective green networking techniques. On the other hand, intercell interference, wireless channel propagation model including shadow fading, and BS power consumption model are the other major factors that can affect any system performance. All these factors are taken into consideration in this proposed research and thus makes the network scenario near realistic.
- (iv) Extensive simulations are carried out for investigating the energy usage analysis of the proposed framework in terms of various performance metrics such as EE, energy consumption indicator (ECI), and on-grid energy savings. Simulations are carried out considering both temporal traffic diversity over 24 hours and spatial traffic diversity over the entire network area.
- (v) The impact of various system parameters including solar storage capacity, storage factor, transmission line loss, solar generation capacity, and CoMP techniques on the performance metrics is demonstrated and critically analyzed. Furthermore, system performance is also compared with that of the existing hybrid non-CoMP-based cellular system having no energy sharing.

The rest of the paper is organized as follows. Section 2 presents a thorough study on the related works. A detailed discussion of the system model along with the network layout and green energy model is outlined in Section 3. In addition, the energy consumption model for macrocell BS and the formulation of performance metrics are also presented in the same section. Section 4 presents the user association policy and the proposed algorithms. Section 5 shows the simulation results with insightful analysis, and finally, Section 6 concludes the paper summarizing the key findings.

## 2. Related Works

Over the last decades, the ever-increasing energy consumption in cellular networks has received intensive attention from regulatory bodies and mobile operators. With the growing awareness of global warming and financial consequences, both researchers and industries have initiated projects to reduce the increasing trend of energy consumption [2, 24, 25]. Switching off some BSs during the low traffic period is the most popular technique for minimizing energy consumption in RAN infrastructure [26–28]. Moreover, the concept of dynamic sectorization of BSs [29] and the traffic-aware intelligent cooperation among BSs [30] have shown remarkable aptitude for improving EE.

In recent years, comprehensive surveys on green cellular networks using various energy saving methods are presented in [4, 12, 31]. Hasan et al. [4] categorized energy saving mechanisms as cooperative networks, adoption of renewable energy resources, deployment of heterogeneous networks, and efficient usage of spectrum. In [31], Xu et al. outlined various distinctive approaches to reduce grid energy consumption in modern cellular networks. The strategies can be broadly classified into energy-efficient hardware design, selectively turning off some components during low-traffic period, optimizing radio transmission process in a physical layer, and powering RANs by renewable energy resources. On the other hand, several research works presented in [13, 32–34] were carried out to improve the EE of the cellular networks with hybrid power supplies. In [13], Peng et al. proposed an energy management technique for cellular networks with the provision of a hybrid energy supply and BS sleep mode. Han and Ansari [33] investigated the optimization of green energy utilization resulting in a significant reduction of conventional grid energy consumption during peak traffic periods. This work did not consider green energy sharing among the BSs. On the other hand, Chia et al. [32] proposed a model for energy sharing between two BSs through a resistive power line, whereas Xu et al. [34] focused on energy harvesting and coordinate transmission-enabled wireless communication by investigating a joint energy and communication cooperative approach. In the proposed paradigm, energy cooperation was implemented by the cellular network operators via signing a contract with the grid operator so that BSs can exchange green energy via the existing grid infrastructure. Besides, the system model has not discussed energy saving issues in this paper. However, none of these papers in [13, 32–34] considered either the JT or the DPS CoMP-based cellular networks for

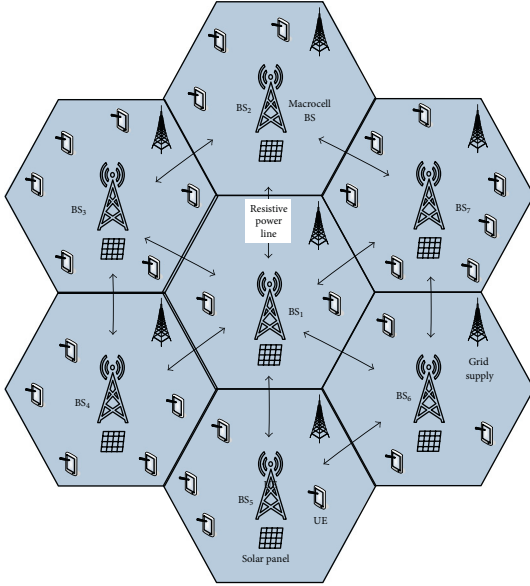


FIGURE 1: A section of the proposed network model with a hybrid energy supply.

investigating the EE performance or developing energy sharing mechanisms.

### 3. System Model

This section presents the proposed network model and other system components in the context of orthogonal frequency division multiple access- (OFDMA-) based LTE-A cellular systems, which can also be adopted to other standards.

**3.1. Network Layout.** The downlink of a multi-cell cellular network having a set of  $N$  BSs  $\mathcal{B} = \{\mathcal{B}_1, \mathcal{B}_2, \dots, \mathcal{B}_N\}$  and covering an area  $\mathcal{A} = \{\mathcal{A}_1 \cup \mathcal{A}_2 \cup \dots \cup \mathcal{A}_N\} \subset \mathbb{R}^2$  is considered. Here,  $\mathcal{A}_n$  is the coverage area of BS  $\mathcal{B}_n$ ,  $n = 1, 2, \dots, N$ . BSs are assumed to be deployed using omnidirectional antennas in a hexagonal grid layout and orthogonal frequency bands are allocated in a BS resulting in zero intracell interference. On the other hand, universal frequency reuse is considered resulting in intercell interference when same frequency band is allocated in two BSs.

All the BSs in the considered LTE-A cellular network are powered by hybrid supplies, namely, PV solar energy and commercial on-grid energy. PV solar energy is the primary energy source, while the grid supply is the standby one. Each BS has an independent on-site solar energy harvester and energy storage device such as a battery bank. For sharing green solar energy among the BSs, each BS is connected with its neighboring BSs through resistive power lines. A segment of the network layout with seven macrocells is depicted in Figure 1. It is also considered that the proposed network is deployed using either the DPS or the JT CoMP transmission technique. On the other hand, UEs are assumed to be distributed uniformly throughout the network. Furthermore, any BS having no user to serve are switched into low power sleep mode for saving energy.

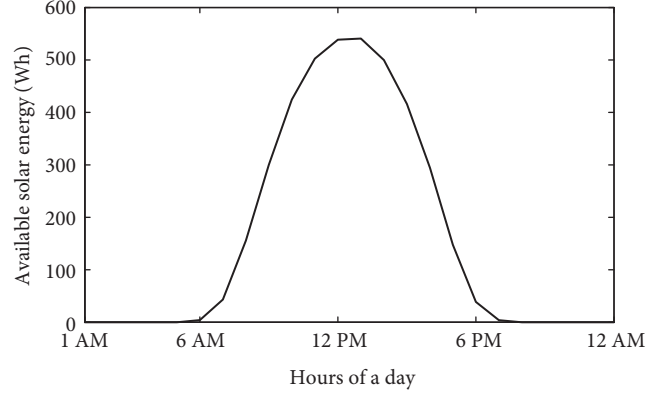


FIGURE 2: Average hourly solar energy generation.

**3.2. Link Model.** This paper considers a channel model with log-normally distributed shadow fading. For a separation  $d$  between transmitter and receiver, path loss in dB can be expressed as

$$PL(d) = PL(d_0) + 10n \log \left( \frac{d}{d_0} \right), \quad (1)$$

where  $PL(d_0)$  is the path loss in dB at a reference distance  $d_0$  and  $n$  is the path loss exponent.  $PL(d_0)$  can be calculated using the free-space path loss equation.

Thus, the received power in dBm for  $j$ th UE at a distance  $d = d^{n,j}$  from  $n$ th BS  $\mathcal{B}_n$  is given by

$$P_r^{n,j} = P_t^{n,j} - PL + X_\sigma, \quad (2)$$

where  $P_t^{n,j}$  is the transmitted power in dBm and  $X_\sigma$  is the amount of shadow fading modeled as a zero-mean Gaussian random variable with a standard deviation  $\sigma$  dB. Then the received SINR  $\gamma_{n,j}$  at  $j$ th UE from  $\mathcal{B}_n$  can be given by

$$\gamma_{n,j} = \frac{P_r^{n,j}}{\mathcal{I}_{j,inter} + \mathcal{I}_{j,intra} + \mathcal{P}_N}, \quad (3)$$

where  $\mathcal{I}_{j,inter}$  is the intercell interference,  $\mathcal{I}_{j,intra}$  is the intracell interference, and  $\mathcal{P}_N$  is the additive white Gaussian noise (AWGN) power given by  $\mathcal{P}_N = -174 + 10 \log_{10}(\Delta f)$  in dBm with  $\Delta f$  as the bandwidth in Hz.

**3.3. Solar Energy Generation Model.** This paper considers the PV solar panel as the on-site green energy harvester. The solar energy generation profile is nondeterministic and depends on some factors, such as temperature, solar light intensity, panel materials, generation technology, and the geographic location of the solar panel. The daily solar energy generation thus shows temporal dynamics over a period of a day in the given area and exhibits spatial variations with geographical location [7]. Due to the tempo-spatial diversity, the available solar energy may not guarantee the adequate energy supplies for a BS to run for a whole day.

Average hourly solar energy generation profile for a full year in Dhaka city of Bangladesh is shown in Figure 2. Here, the solar energy profile for a particular region is estimated by

adopting the System Advisor Model (SAM) [35]. The curve indicates that the green energy generation starts from around 6:00 AM, reaches peak value at noon, and stops at about 6:00 PM. SAM supports various solar power generation technologies. However, without losing the generality, distributed type concentrated solar power (CSP) PV technology with 1 kW solar panel is used for generating the shown curve. On the other hand, though solar batteries such as Ni-Cd, NiMH, Li-ion, and sodium nickel chloride are available for using in solar systems, lead-acid batteries are commonly used in solar-powered BSs. The parameters of the solar generation and storage systems for the considered 1 kW solar panel are summarized in Table 1.

**3.4. Solar Energy Storage Model.** For the proposed system, the green energy storage of the  $n$ th BS  $\mathcal{B}_n$  at time  $t$  can be given by

$$s_n(t) = \mu s_n(t-1) + r_n(t) - d_n(t), \quad (4)$$

where  $s_n$  is the green energy storage,  $r_n$  is the incoming energy from PV solar panel,  $d_n$  is the energy demand of the BS, and  $0 \leq \mu \leq 1$  is the storage factor, that is, the percentage of storage energy retained after a unit period of time. For example,  $\mu = 0.9$  indicates that 10% of energy will be lost in the storage during the time interval. It is to be noted that the stored energy cannot exceed the maximum storage capacity. Therefore, if the generation is higher than the storage capacity, that amount of energy is considered as wastage.

**3.5. BS Power Consumption Model.** It is important to investigate the traffic demand to be served by the BSs in order to analyze the energy consumption of the network. The mobile traffic volume exhibits both temporal and spatial diversity. Mobile users are assumed randomly distributed. It is also assumed that BSs transmit data to all users with the same data rate. Based on internal surveys on operator traffic data within the EARTH project and the Sandvine report [36], the daily traffic demand in the network is characterized by the normalized traffic profile illustrated in Figure 3.

The BSs energy consumption is directly related to the traffic volumes [37]. The energy consumption of BSs can be subdivided into two parts: the static energy consumption and the dynamic energy consumption. Holtkamp et al. [38] approximated the operating power of a BS as a linear function of RF output power  $P_{\text{MAX}}$  and BS loading parameter  $x$ , which can be given by [38]

$$P_{\text{in}} = \begin{cases} M_{\text{sec}}[P_1 + \Delta_p P_{\text{MAX}}(x-1)], & \text{if } 0 < x \leq 1 \\ M_{\text{sec}} P_{\text{sleep}}, & \text{if } x = 0 \end{cases}, \quad (5)$$

where the expression in the square brackets represents the total power requirement for a transceiver (TRX) chain,  $M_{\text{sec}}$  is the number of sectors in a BS, and  $P_1$  is the maximum power consumption in a sector. The load dependency is accounted for by the power gradient,  $\Delta_p$ . The loading parameter  $x = 1$  indicates a fully loaded system, that is, BS transmitting at full power with all of their LTE resource blocks (RBs)

TABLE 1: Solar panel and storage device parameters.

Parameters	Type (value)
Solar module type	Photovoltaic (distributed)
Generation technology	CSP PV cell
Solar panel capacity	1 kWdc
DC-to-AC ratio	0.9
Array type	Fixed roof mount
Tilt	20 degrees
Azimuth	180 degrees
Storage type	Lead-acid battery
Storage capacity	2000 Wh
Storage factor	0.96

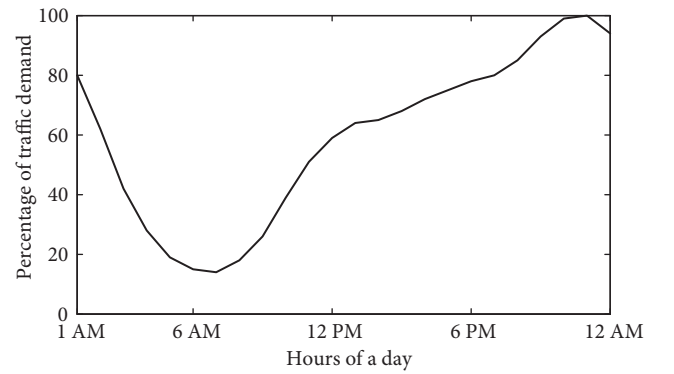


FIGURE 3: Daily traffic profile of a residential area.

occupied, and  $x = 0$  indicates idle state. Furthermore, a BS without any traffic load enters into sleep mode with lowered consumption,  $P_{\text{sleep}}$ . Now  $P_1$  can be expressed as follows [38]:

$$P_1 = \frac{P_{\text{BB}} + P_{\text{RF}} + P_{\text{PA}}}{(1 - \sigma_{\text{DC}})(1 - \sigma_{\text{MS}})(1 - \sigma_{\text{cool}})}, \quad (6)$$

where  $P_{\text{BB}}$  and  $P_{\text{RF}}$  are the power consumption of baseband unit and radio frequency transceiver, respectively. Losses incurred by DC-DC power supply, main supply, and active cooling can be approximated by the loss factors  $\sigma_{\text{DC}}$ ,  $\sigma_{\text{MS}}$ , and  $\sigma_{\text{cool}}$ , respectively. However, power consumption in the power amplifiers is represented by  $P_{\text{PA}}$  which depends on the maximum transmission power and power amplifier efficiency  $\eta_{\text{PA}}$  and can be given as follows [38]:

$$P_{\text{PA}} = \frac{P_{\text{MAX}}}{\eta_{\text{PA}}(1 - \sigma_{\text{feed}})}. \quad (7)$$

BS power consumption model parameters used in this paper are summarized in Table 2.

**3.6. Performance Metrics.** This paper evaluates the on-grid energy savings offered by the proposed network models compared to that of the conventional networks powered by grid supply only (i.e., no solar power). The average on-grid energy savings at time  $t$  denoted by  $E_s(t)$  can be written as

TABLE 2: BS power consumption model parameters [38].

Parameters	Value
BS type	Macro
$\eta_{PA}$	0.306
$\gamma$	0.15
$P_{BB}$ (W)	29.4
$P_{RF}$ (W)	12.9
$\sigma_{feed}$	0.5
$\sigma_{DC}$	0.075
$\sigma_{MS}$	0.09
$\sigma_{cool}$	0.1
Number of sectors, $M_{sec}$	1
Maximum transmit power, $P_{MAX}$ (dBm)	43
$\Delta_p$	4.2
$P_{sleep}$ (W)	54

$$E_s(t) = \frac{\sum_{n=1}^N P_s(n, t)}{\sum_{n=1}^N P_{in}(n, t)} \times 100\%, \quad (8)$$

where  $P_{in}(n, t) = d_n(t)$  is the required total power in BS  $\mathcal{B}_n$  at time  $t$  and  $P_s(n, t)$  is the green solar power utilized by the BS  $\mathcal{B}_n$  for serving its UEs.

On the other hand, EE performance metric of a network given in terms of bits per joule can be defined as the ratio of the total throughput to the total power required for running the network. In this paper, we define the EE metric of the proposed network models with CoMP techniques and hybrid power supply as the ratio of the aggregate throughput of the network to that of the net on-grid power consumed by the network. Total achievable throughput in a network at time  $t$  can be calculated by Shanon's capacity formula as follows:

$$R_{total}(t) = \sum_{j=1}^U \sum_{n=1}^{N_j} \Delta f \log_2(1 + \gamma_{n,j}), \text{ bps}, \quad (9)$$

where  $N_j$  is the number of transmitting BSs for serving  $j$ th UE and  $U$  is the total number of UEs in the network. Thus, the EE metric denoted as  $\eta_{EE}$  for time  $t$  can be written as follows:

$$\eta_{EE}(t) = \frac{R_{total}(t)}{\sum_{n=1}^N P_g(n, t)}, \text{ bits/joule}, \quad (10)$$

where  $P_g(n, t) = P_{in}(n, t) - P_s(n, t)$  is the on-grid energy consumption in BS  $\mathcal{B}_n$  at time  $t$ .

An alternative performance metric for evaluating the EE of a BS is the Energy Consumption Index (ECI) defined in [39], which can be given by

$$ECI = \frac{P_{in}}{KPI}, \quad (11)$$

where  $P_{in}$  refers to the total input power of a BS, whereas KPI (key performance indicator) indicates the total throughput of the BS. In other words, ECI is the reciprocal of EE, and hence, for the proposed networks, it can be evaluated by taking the inverse of (10), while a lower value of ECI implies better EE and vice versa. ECI is more suitable for better visualization of network behavior when the denominator of (10) becomes zero.

## 4. User Association and Algorithm

*4.1. User Association Policy.* The term user association means assigning a UE with a BS for receiving service. Associating users with the closest BS does not always ensure the best SINR due to the randomness of shadow fading. Therefore, user association policy based on the better signal quality (i.e., higher SINR) can support better performance. Therefore, this paper proposes SINR-based user association policy, which is presented for the DPS and JT CoMP-based networks as follows:

- (i) *Network with DPS CoMP.* In a network deployed with the DPS CoMP-based transmission technique, one of the available BSs is dynamically selected for serving a UE in the best way. Thus, under the proposed network models with DPS, the BS which provides the highest SINR is selected for associating a UE.
- (ii) *Network with JT CoMP.* In JT CoMP-based networks, multiple BSs are dynamically selected for serving a UE. For instance, in a network with 2-BS JT system, two BSs providing the top two SINR values are selected for associating a UE, which jointly transmits data to the particular UE.

*4.2. Energy Sharing Algorithm.* This section presents the proposed energy management scheme with the provision of green energy sharing. Under the proposed network model, each BS is equipped with a PV solar module with a storage facility, which acts as the primary energy source and can be shared among the neighboring BSs. In case there is not adequate energy stored in the storage of a BS, it seeks solar green energy from the neighboring BSs for supporting continuous service for its users. While seeking solar energy, a BS aims to share through the feasible shortest path for minimizing the power loss in the interconnecting resistive transmission line. This implies that a BS can share solar energy only from the six neighboring BSs placed in the first-tier surrounding it as illustrated in Figure 1. Furthermore, a BS aims to share from the BSs having higher solar energy stored.

On the other hand, a neighboring BS shares the surplus energy from its storage only after fulfilling its own demand. If solar energy is not available from the neighboring BSs, only then energy from the standby grid supply is used. Thus, there can arise two different cases for using energy in the BSs, which are presented as below with respect to the  $n$ th BS  $\mathcal{B}_n$ .

**4.2.1. Case I: Sufficient Green Energy in Storage.** If  $s_n(t) \geq d_n(t)$ , then the  $n$ th BS  $\mathcal{B}_n$  has sufficient solar energy for serving its UEs, and hence, the BS will be powered using its own stored energy. Thus, there is no need of green energy sharing from other BSs as well as no on-grid energy is consumed. The remaining solar energy in the storage after fulfilling the demand denoted by  $g_n(t)$  can be expressed as

$$g_n(t) = s_n(t) - d_n(t). \quad (12)$$

Therefore, after meeting the demand of time  $t$ , the available solar energy in the storage of  $\mathcal{B}_n$  for the time slot  $(t + 1)$  can be written as

$$s_n(t + 1) = \mu g_n(t) + r_n(t + 1) - d_n(t + 1), \quad (13)$$

where  $r_n(t + 1)$  and  $d_n(t + 1)$  are the generation of solar energy and the total energy demand for time  $(t + 1)$ , respectively.

**4.2.2. Case II: Insufficient Green Energy in Storage.** The scenario with  $s_n(t) < d_n(t)$  implies that there is not sufficient solar energy stored for powering the BS  $\mathcal{B}_n$ , and hence, solar energy sharing is required. Hence,  $\mathcal{B}_n$  seeks for the additional solar energy from its neighbors, which is the difference between the total energy demand and the solar energy remaining in its own storage. Therefore, the total green energy required to be shared by  $\mathcal{B}_n$  at time  $t$  denoted by  $g_{n,s}(t)$  can be expressed as

$$g_{n,s}(t) = d_n(t) - s_n(t). \quad (14)$$

For sharing solar energy, BS  $\mathcal{B}_n$  sorts its neighbors in a descending order of the available solar energy in their respective storages. Let the set of sorted BSs be given by  $\mathbb{B}_n = \{\mathcal{B}_{n,1}, \mathcal{B}_{n,2}, \dots, \mathcal{B}_{n,M}\}$ , where  $M$  is the number of neighboring BSs of  $\mathcal{B}_n$  for sharing energy and  $\mathcal{B}_{n,p}$  has higher storage than  $\mathcal{B}_{n,q}$  for  $p < q$ . Now, if the neighboring BS  $\mathcal{B}_{n,1}$  has a shareable solar energy  $\geq g_{n,s}(t)$ , BS  $\mathcal{B}_n$  accepts this amount from  $\mathcal{B}_{n,1}$  that fulfills its demand. The sharable solar energy of a BS is the amount that can be shared after fulfilling its own demand. If the sharable energy of  $\mathcal{B}_{n,1}$  is  $< g_{n,s}(t)$ , BS  $\mathcal{B}_n$  accepts the amount from  $\mathcal{B}_{n,1}$  that it can share.

For the remaining amount of required energy, BS  $\mathcal{B}_n$  seeks to share from  $\mathcal{B}_{n,2}$  and continues to the next BSs in  $\mathbb{B}_n$ . Let  $\varepsilon_{n,m}$  be the amount of solar energy shared by  $\mathcal{B}_n$  from the neighboring BS  $\mathcal{B}_{n,m}$ . Then the total solar energy received by  $\mathcal{B}_n$  from the neighboring BSs can be given by

$$\varepsilon_n(t) = \sum_{m=1}^M \alpha_{n,m} \varepsilon_{n,m}(t), \quad (15)$$

where  $0 \leq \alpha_{n,m} \leq 1$  is the utilization factor representing the line loss between BS  $\mathcal{B}_n$  and its neighbor  $\mathcal{B}_{n,m}$ , that is, while sharing  $\alpha_{n,m} \times 100\%$  of the energy is dissipated as line loss.

If  $\varepsilon_n(t) = g_{n,s}(t)$ , no on-grid energy is used by BS  $\mathcal{B}_n$  at time  $t$ . Otherwise, on-grid energy is consumed for powering BS  $\mathcal{B}_n$  for serving its UEs. Thus, the conventional grid energy consumption denoted by  $c_n(t)$  by  $\mathcal{B}_n$  at time  $t$  can be given by

TABLE 3: Pseudo code of the proposed energy sharing algorithm for  $n$ th BS  $\mathcal{B}_n$ .

---

```

1: Initialize:  $s_n(t), d_n(t), \mu, \alpha_{n,m}, \varepsilon_{n,m} = 0, \forall n = 1, 2, \dots, N;$ 
    $\forall m = 1, 2, \dots, M$ 
2: If  $s_n(t) \geq d_n(t)$ 
3:    $P_s(n, t) = d_n(t)$  and  $P_g(n, t) = 0$ 
4:    $g_n(t) = s_n(t) - d_n(t)$ 
5:   Else
6:     Coordinate with other BSs for sharing solar energy
     Sort the neighboring  $M$  BSs with respect to stored energy
     i.e., find the set  $\mathbb{B}_n = \{\mathcal{B}_{n,1}, \mathcal{B}_{n,2}, \dots, \mathcal{B}_{n,M}\},$ 
      $s.t., s_{n,p}(t) \geq s_{n,q}(t)$  for  $p < q$ 
7:     For  $m = 1 : M$ 
8:       Calculate  $r_{n,s}(t) = g_{n,s}(t) - \sum_{k=0}^{m-1} \alpha_{n,k} \varepsilon_{n,k}(t),$ 
          $\varepsilon_{n,k}(t) = 0$  for  $k < 1$ 
9:       If  $s_{n,m}(t) - d_{n,m}(t) \geq r_{n,s}(t)$ 
10:        Share solar energy  $\varepsilon_{n,m}(t) = r_{n,s}(t)$  from  $\mathcal{B}_{n,m}$ 
11:       Else
12:        Share solar energy  $\varepsilon_{n,m}(t) = s_{n,m}(t) - d_{n,m}(t)$ 
         from  $\mathcal{B}_{n,m}$ 
13:       If  $\sum_{k=1}^m \alpha_{n,k} \varepsilon_{n,k}(t) = g_{n,s}(t)$ 
14:        Stop the algorithm and Go to Step 21
15:       Else
16:         $m = m + 1$  and Go to Step 8
17:       End If
18:     End If
19:   End For
20:   If  $\sum_{m=1}^M \alpha_{n,m} \varepsilon_{n,m}(t) = g_{n,s}(t)$ 
21:      $P_s(n, t) = d_n(t)$  and  $P_g(n, t) = 0$ 
22:     Stop the algorithm
23:   Else
24:      $P_s(n, t) = \varepsilon_n(t) = \sum_{m=1}^M \alpha_{n,m} \varepsilon_{n,m}(t)$ 
25:      $P_g(n, t) = d_n(t) - \varepsilon_n(t)$ 
26:   End If
27: End If

```

---

$$P_g(n, t) = d_n(t) - \varepsilon_n(t). \quad (16)$$

Pseudo codes of the energy sharing algorithm with respect to the  $n$ th BS  $\mathcal{B}_n$  is presented in Table 3. In the pseudo code,  $d_{n,m}(t)$  and  $s_{n,m}(t)$  are the total energy demand and the stored solar energy of the  $m$ th BS  $\mathcal{B}_{n,m} \in \mathbb{B}_n$ .

## 5. Performance Analysis

**5.1. Simulation Setup.** This section analyzes the performance of the proposed cellular network framework with BSs powered by PV solar energy and standby grid supply. A MATLAB-based Monte Carlo simulation platform is developed for carrying out extensive simulations. For each data point, results are calculated by averaging over 10,000

independent iterations each with a simulation time of seven days. The network is deployed using a hexagonal grid layout with a cell radius of 1000 m. For comprehensive performance evaluation, intercell interference contributions by the 18 BSs placed in the two surround tiers are taken into consideration. On the other hand, UEs are considered uniformly distributed over the geographical area. Performance of the proposed network model for any nonuniform UE distribution can also be evaluated in a similar way. It is assumed that one UE occupies one RB and equal transmit power over all RBs. Furthermore, under the JT CoMP-based network, it is considered that the top two BSs providing the best SINR values serve a UE simultaneously. A summary of the system parameters of the simulated network are set in reference to the LTE standard [18] as summarized in Table 4. On the other hand, unless otherwise specified, the proposed network models are simulated considering  $x$  as a uniform random variable in [0,1] for modeling the spatial variation in traffic generation among the BSs, while equal solar generation is assumed in all the BSs having the solar module parameters as presented in Table 1.

## 5.2. Result Analysis

**5.2.1. SINR and Throughput Analysis.** Figure 4 demonstrates the empirical cumulative distribution function (CDF) of received SINR at UEs located throughout the considered network model. The network is considered with fully loaded (i.e.,  $x = 1$ ) BSs, which are supplied with hybrid supply with no inter-BS energy sharing. From the figure, a clear distinction in SINR distribution is observed among the JT CoMP-, DPS CoMP-, and non-CoMP-based hybrid systems. The JT CoMP-enabled hybrid system keeps its optimistic nature achieving comparatively stronger SINR among UEs, which ranges around  $-2$  dB to 60 dB. This is because the two BSs offering the highest SINR values simultaneously serve a UE resulting in significantly better signal quality. In contrast, a non-CoMP-based hybrid scheme has the worst SINR performance as it spreads out over a larger range compared to that of the other techniques. SINR performance of the DPS CoMP-based system lies in between the JT and the non-CoMP-based systems as it selects the BS supporting the best signal quality. Thus, from the view point of SINR, the JT CoMP-based hybrid model is a preferred choice compared to the others.

On the other hand, a comparison of the throughput performance over a day among the different hybrid schemes is shown in Figure 5. As seen from the figure, throughput curves clearly follows the given traffic pattern (Figure 3). Also, a clear distinction is observed between the low traffic and the peak traffic times. This is because higher traffic means the allocation of higher number of RBs to the users resulting in higher throughput. Further, during peak traffic arrivals, throughput gap is more significant among the different hybrid systems. On the other hand, it is observed that the JT CoMP-based hybrid system outperforms others in terms of throughput. As throughput is directly related to the signal quality, superior SINR performance of the JT CoMP-based

TABLE 4: Simulation parameters.

Parameters	Value
Resource block (RB) bandwidth	180 kHz
System bandwidth, BW	10 MHz (50 RBs), 600 subcarriers
Carrier frequency, $f_c$	2 GHz
Duplex mode	FDD
Cell radius	1000 m
BS transmission power	43 dBm
Noise power density	$-174$ dBm/Hz
Number of antennas	1
Reference distance, $d_0$	100 m
Path loss exponent, $n$	3.574
Shadow fading, $\sigma$	8 dB
Access technique, DL	OFDMA
Traffic model	Randomly distributed

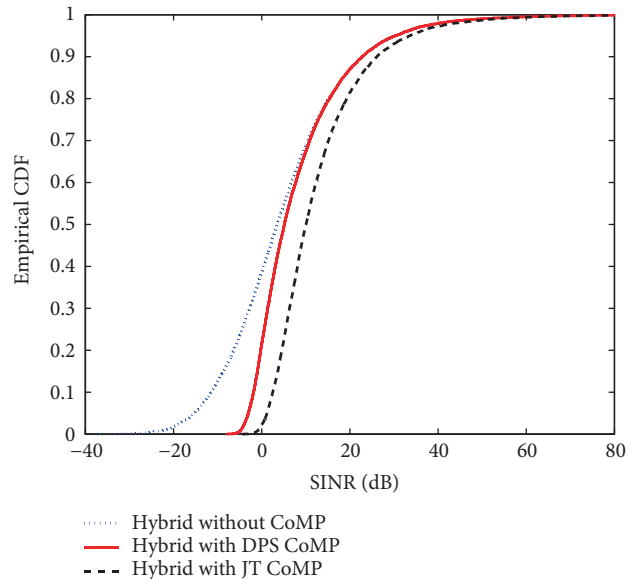


FIGURE 4: Empirical CDF of received SINR among the different hybrid systems for  $x = 1$ .

model as observed in Figure 4 ensures its relatively higher throughput.

**5.2.2. Energy Analysis with Hybrid Supply under No Energy Sharing.** Figure 6 compares the temporal variation of energy consumption by a BS in a conventional cellular system to that in the proposed network model with hybrid energy supply without energy sharing option. Here, the conventional scheme implies a cellular system powered by only grid energy with no energy sharing option and no CoMP transmission mechanism. As seen from the figure, on-grid consumption of a BS in the conventional system follows traffic distribution, reaches at peak when traffic demand is the highest, and goes down as the traffic decreases. Use of solar energy in BSs and sharing this energy among BSs is to minimize this grid energy usage. The energy consumption curve for the hybrid model

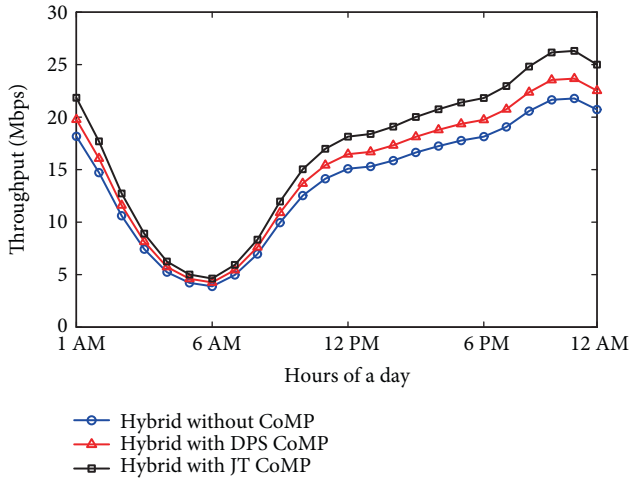


FIGURE 5: Throughput comparison of a single BS among the different hybrid models.

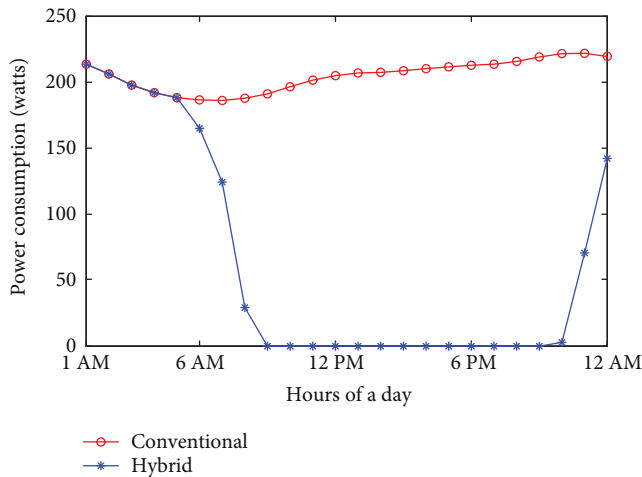


FIGURE 6: Comparison of on-grid power consumption in a single BS between the existing hybrid energy model (no sharing) and the conventional scheme with grid supply only. No CoMP technique is implemented in the network models.

with no sharing option is also presented assuming a storage capacity of 2kWh. As seen, up to around 5 AM, a BS is completely run by on-grid supply as solar energy is unavailable during this period. After this, on-grid energy consumption gradually decreases with the increase of solar energy availability and becomes zero at 9 AM. Between 9 AM and 9 PM, there is adequate solar energy available for running the BS, and hence, no consumption of conventional energy. During this period, a BS fulfill its demand from its own solar energy storage and stores the surplus energy for future use. As time goes, stored solar energy decreases gradually with the decrease of solar light intensity, and once again, on-grid energy is required to serve its associated users after 9 PM. Thus, due to this temporal dynamics of solar energy generation, the available solar energy is not always sufficient for supplying the BS, and hence, on-grid energy is still required to fully meet the BS demand.

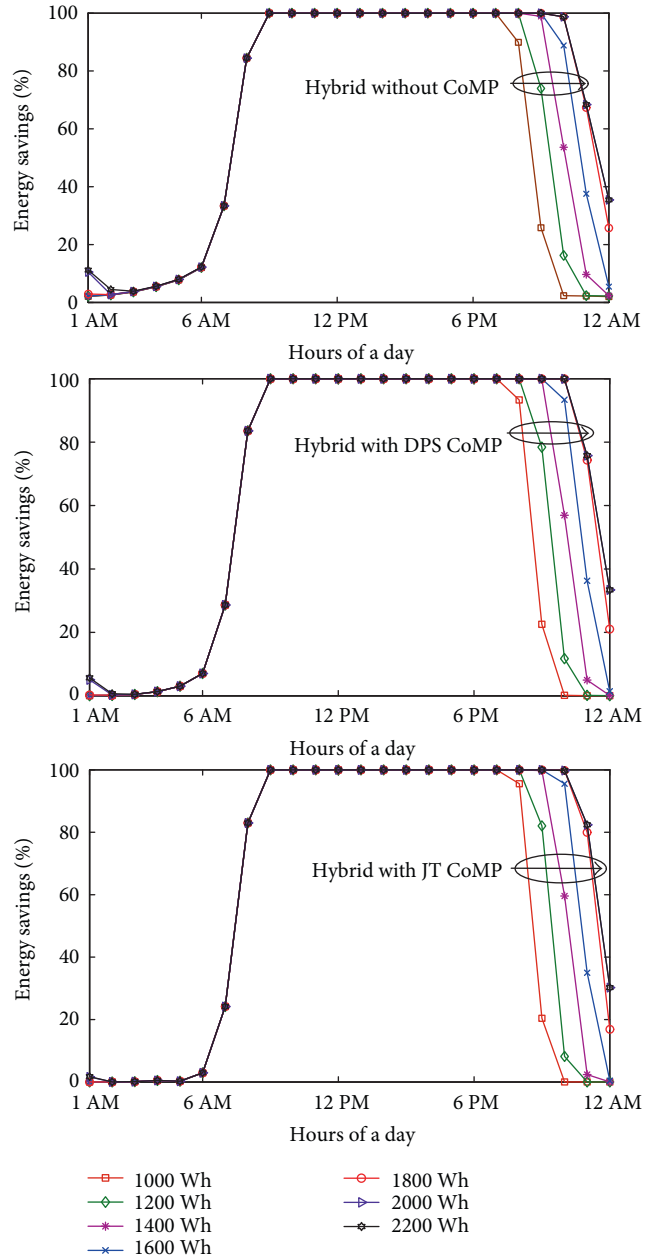


FIGURE 7: Average on-grid savings of a BS for different storage capacities with 1 kW solar module and no energy sharing.

Percentage of energy savings under the different network models with hybrid power supply for various solar storage capacity is demonstrated in Figure 7. Here the network model having hybrid energy supply with no energy sharing and non-CoMP transmission refers to the existing hybrid system. As seen from the figure, during 12 AM to 6 AM, the BSs are mainly run by grid energy, and hence the savings in this period are mainly due to the switching of some BSs having no traffic into sleep mode. Under JT CoMP, energy savings in this period are found almost zero as the probability of BSs to enter into sleep mode is negligible. As the time proceed from 6 AM, solar energy generation increases leading to higher on-grid energy savings, which eventually reaches the

peak around noon and following a gradual decrease around the evening. Thus, the hybrid scheme has the potential to reduce the on-grid energy consumption up to 100% for a prolonged period of time as evident from the figure. On the other hand, a significant impact of storage capacity on the energy savings is observed. As seen from the figure, the energy savings region is expanded with the increase of storage capacity resulting in higher savings. For example, energy savings curve for 2 kWh storage capacity lasts longer compared to that for a capacity of 1 kWh. Furthermore, the saving curves for 2 kWh is fully overlapped with that of 2.2 kWh and further increases in the storage capacity have no impact on energy savings as evident from the figure. Thus, the optimal value of storage capacity is 2 kWh. Notably, the energy saving performance follows similar fashion for all the three hybrid models having no significant variation due to CoMP techniques. This implies that for the particular network setting, savings is dependent predominantly on the solar energy generation and storage capacity.

A comparison of ECI performance metric with the three hybrid models is presented in Figure 8. During the low traffic periods in the morning, ECI increases rapidly up to a certain point and then starts to fall beyond that point. The upward trending nature of ECI implies the relatively higher on-grid energy consumption as the available solar energy is almost negligible. With the increase of solar energy generation, the ECI curve is pushed downward. It can be seen that during 9 AM to 9 PM, the ECI curve falls to zero indicating no on-grid energy consumption, that is, maximum EE. With the diminishing sunlight, stored energy also runs out by powering the BSs, and once again after 9 PM, on-grid energy is required to supply the BSs resulting in an upward trend of the ECI curve. On the other hand, since throughput performance of JT CoMP is better than that of DPS CoMP as observed in Figure 5, the JT CoMP-based hybrid system provides superior ECI performance. It can also be seen that the proposed network models have better ECI performance compared to that of the existing hybrid system.

Figure 9 illustrates the variation of average EE and the average on-grid power consumption in a BS under different hybrid schemes with the solar storage capacity. The network is simulated over a period of a week considering 1 kW solar panel in each BS as a green energy harvester. The three power consumption curves decrease in a similar fashion. The tendency of the down trending of the energy consumption curves indicates that the energy drawn from the grid decreases with the increment of storage capacity. The curves eventually reach to their respective constant values, which is also supported by Figure 7. This is because the storage limit reached optimum value for the given solar panel capacity and further increase in storage capacity does not make any significant improvement in reducing on-grid consumption. It is also observed that the grid power consumption is slightly higher under the JT CoMP-based hybrid system as two BSs simultaneously serve a particular UE. On the other hand, the EE curves demonstrate the opposite trend with the increment of storage capacity. However, the JT-based hybrid model shows superior EE performance compared to the DPS-based and the existing non-CoMP-based hybrid model

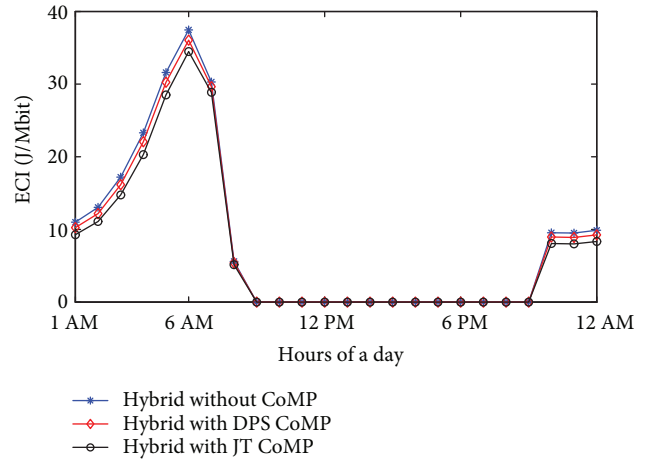


FIGURE 8: ECI comparison among the different hybrid models without sharing.

due to its significantly higher throughput. As expected, EE metric also eventually reaches its peak and remains constant after the optimal storage capacity, which is found equal to 2 kWh.

### 5.2.3. Energy Analysis with Hybrid Supply under Energy Sharing

(1) *Equal Solar Generation Capacity.* Figure 10 presents the impact of the resistive loss in the green energy transmission lines on the EE metric under different hybrid models evaluated over a period of one week. The systems are simulated assuming that each BS has an equal solar panel capacity of 1 kW with the optimal storage capacity of 2 kWh. Results for the three different scenarios, namely, hybrid only with no CoMP, hybrid with DPS CoMP, and hybrid with JT CoMP, are shown. From the figure, a clear difference is noticed in the EE metric performance with energy sharing and no sharing techniques of the respective hybrid models. The figure depicts that the EE performance has a decreasing trend with the increase of line loss. For the case of the hybrid model with no CoMP system, up to a certain percentage of line loss (around 55%), the EE performance with energy cooperation among BSs remains better than that of the corresponding non-cooperation-based scheme. Beyond this amount of line loss, energy cooperation degrades the network EE. Further analysis of the figure identifies that the concept of solar energy sharing can improve the EE of the DPS-based CoMP scheme if the line loss is less than 15%, while apparently no positive impact of such cooperation is observed for the JT-based CoMP scheme.

Dependency of EE on the storage factor of batteries over a period of a week is illustrated in Figure 11. The solar panel capacity and the storage capacity are same as those of Figure 10. As shown, all of the curves have a similar pattern reaching their respective peak values at a storage factor of 1. Storage factor indicates percentage of storage energy retained after unit period of time and the higher value of  $\mu$  provides better EE. For the hybrid case with no CoMP mechanism,

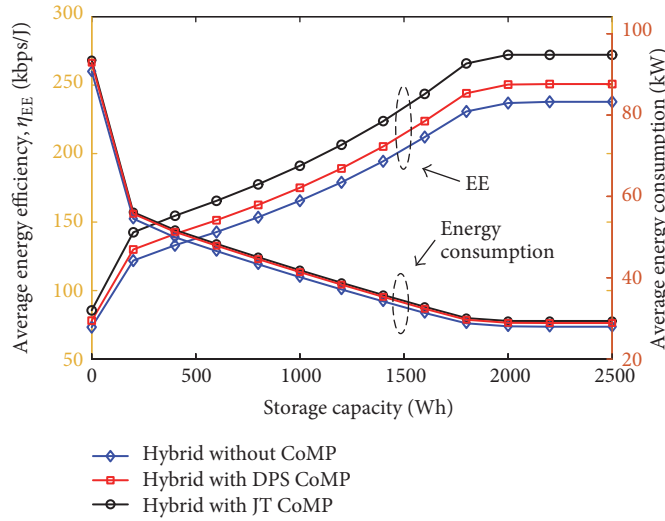


FIGURE 9: Comparison of EE and on-grid power consumption for the three different hybrid schemes without sharing.

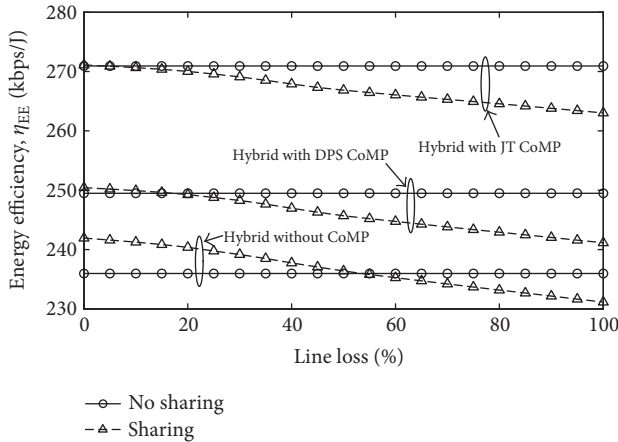


FIGURE 10: EE variation with line loss under the different hybrid scenarios with energy sharing considering equal solar capacity.

energy sharing demonstrates a positive impact on EE with the increase of storage factor  $\mu$ . However, the best EE is found for the JT-based hybrid model in which the curves of sharing and no sharing are fully overlapping with each other, whereas the EE curves of DPS CoMP lie in between the former two hybrid models.

On the other hand, Figure 12 illustrates the impact of solar panel capacity on the EE performance of the proposed models. With the increase of solar panel capacity, storage capacity is also linearly scaled for guaranteeing no wastage of generated solar energy. As evident from the figure, with the increase of solar capacity (i.e., higher available solar energy), EE of the proposed network models substantially improves, which is mainly due to the increasing use of solar energy for running the BSs. From the figure, we can also determine the minimum solar capacity required for running the BSs 24 hours from solar energy. This is the capacity beyond which EE becomes infinity implying that no on-grid energy is required. As seen in the figure, this capacity is found around 1800 W and 1700 W for no sharing and

sharing schemes, respectively. Once again, the difference between the energy sharing models and the corresponding no sharing models is not that much significant as also observed in Figures 10 and 11. Furthermore, comparison of Figures 10–12 clearly demonstrates that the proposed hybrid models with CoMP techniques and energy sharing mechanism has superior EE performance compared to that of the existing hybrid system.

(2) *Spatial Diversity in Solar Energy Generation.* On top of the temporal diversity in solar generation in a BS as considered in the previous simulations, this section presents the results by introducing the spatial diversity as well. This phenomenon of spatial diversity in solar energy generation among the BSs is modeled as a uniform random variable distributed in  $[0,1]$  multiplied by a constant  $c_s$ . Unless otherwise specified,  $c_s = 1$  kW is used for the simulations.

Under such scenario, comparison of EE with the resistive line loss evaluated over one week is illustrated in Figure 13. The figure follows the similar fashion of Figure 10. However, the figure depicts significant performance gap between the energy sharing and the corresponding no energy sharing based schemes. As the solar generation now varies from BS to BS, energy cooperation becomes more effective for improving EE by sharing surplus solar energy of some BSs with other BSs having lower amount. For the same reasons, compared to Figure 11, Figure 14 demonstrates a clear impact of energy sharing on the EE with varying storage factor  $\mu$ . Furthermore, EE gap between the energy sharing and the corresponding no sharing cases is found higher for lower values of  $\mu$ , which diminishes as  $\mu$  increases to 1. The lower storage factor indicates lower amount of useful energy stored in the batteries, which stimulates the necessity of sharing solar energy from the neighboring BSs leading to higher gap and vice versa.

Figure 15 presents the variation of EE with the solar module capacity demonstrating the impact of energy sharing and no sharing operation for a network with spatial diversity of

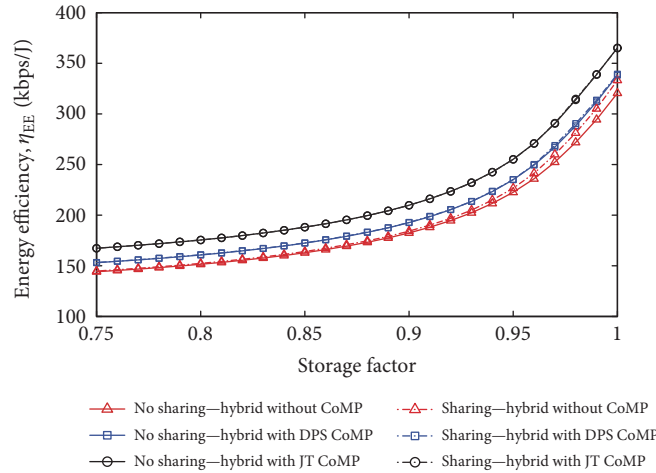


FIGURE 11: Variation of EE with storage factor with energy sharing considering equal solar capacity.

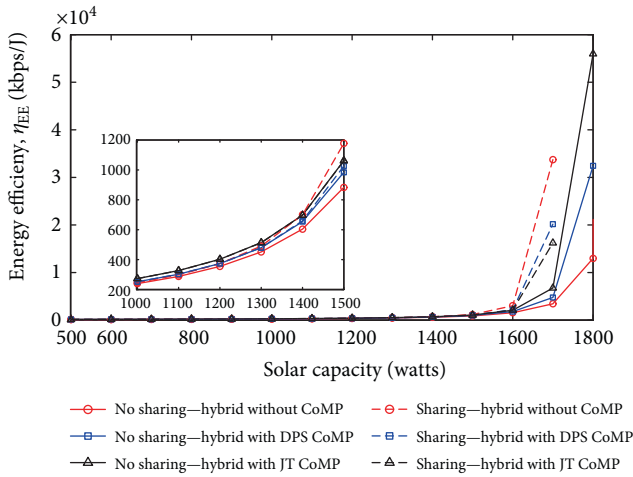


FIGURE 12: EE of the different hybrid schemes with energy sharing under equal solar capacity.

solar energy generation. Any capacity shown in the  $x$ -axis, for instance, 1 kW, implies that the solar energy generation varies among the BSs according to a uniform random variable distributed in  $[0,1]$  with  $c_s = 1$  kW. As expected, EE of the proposed networks improves with the increase of solar capacity. Furthermore, comparison with the Figure 12 identifies that the positive impact of energy sharing on the EE is more apparent under the case of varying solar energy generation, which can be explained in the same way as presented for Figures 13 and 14. Once again, EE performance of the proposed CoMP-based systems are found significantly better than that of the existing hybrid system as illustrated in Figures 13–15.

### 6. Conclusion

This paper have proposed a framework for an energy efficient cellular network with hybrid-powered BSs, where a PV solar module acts as the main energy source for a BS and the grid

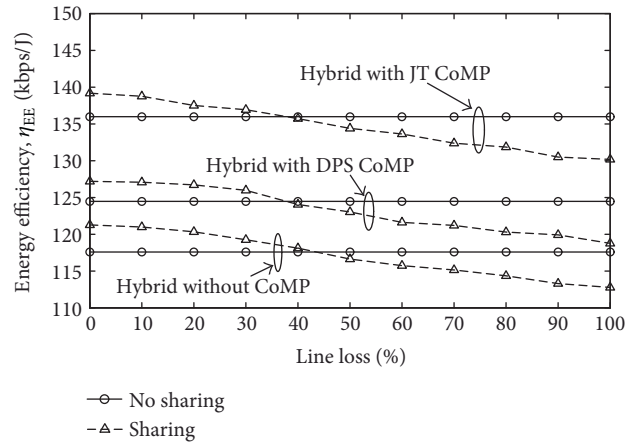


FIGURE 13: EE with line loss for different hybrid scenarios with energy sharing under varying solar capacity.

remains as the standby. A solar energy sharing algorithm among the BSs has also been proposed for further greening the cellular networks by minimizing on-grid energy consumption. The proposed framework has been analyzed for both the DPS and the JT CoMP transmission techniques based on future cellular networks. System performance has been evaluated in terms of EE, energy savings, and throughput by comprehensive Monte Carlo simulations under varying system parameters, such as storage capacity, resistive line loss, storage factor, solar generation capacity, and CoMP techniques. Simulation results have shown that EE and energy savings of the proposed hybrid system increase with the increase in the storage capacity but approach to a peak value after a certain optimum capacity beyond which no further improvement is inflicted. Moreover, a continuous increase in EE has been observed for better storage factors, whereas the resistive loss in the transmission lines has been found to have significant deteriorating impact resulting in reduced improvement in EE. On the other hand, the proposed solar energy cooperation among the neighboring BSs

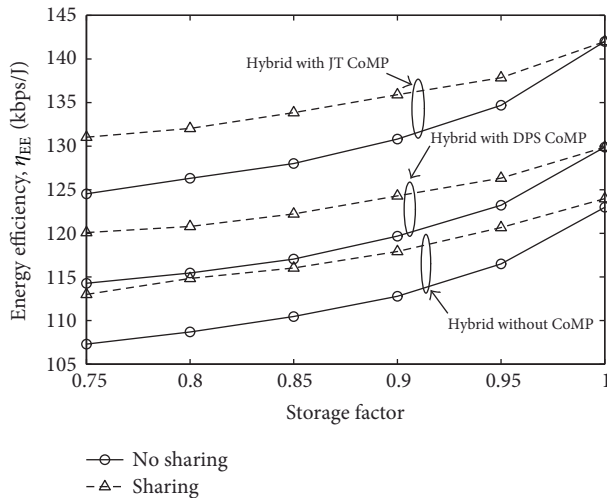


FIGURE 14: EE with storage factor for different hybrid scenarios with energy sharing under varying solar capacity.

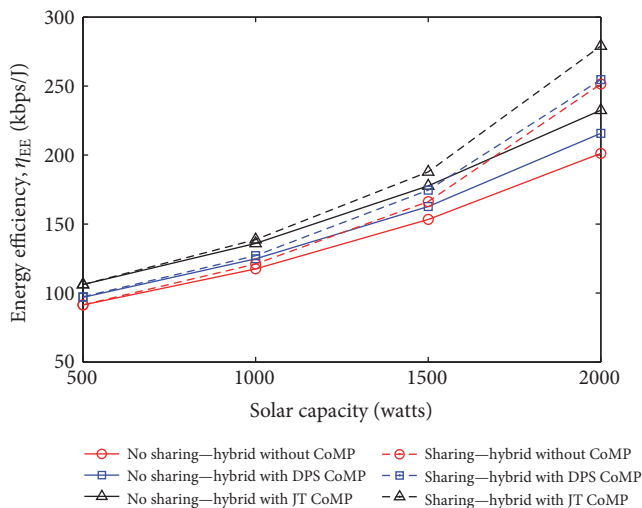


FIGURE 15: EE for different hybrid schemes with energy sharing under varying solar capacity.

have demonstrated a significant improvement in network EE for all the CoMP- and non-CoMP-based networks. It has also been identified that the JT CoMP hybrid system has the best EE performance compared to the DPS CoMP scheme. Moreover, the proposed network models have always been found higher energy efficient than the existing hybrid scheme with no energy sharing and non-CoMP transmission. Furthermore, energy sharing has been figured out more effective for improving EE in networks having spatial diversity in solar energy generation. In summary, the degree of improvement in EE of the proposed hybrid-powered network models with and without the proposed energy sharing mechanism has been found highly dependent on the network scenarios.

## Conflicts of Interest

The authors declare that there is no conflict of interest regarding the publication of this paper.

## References

- [1] K. A. Adamson and C. Wheelock, "Off-Grid Power for Mobile Base Stations," *Technical Report, Navigant Research*, 2013.
- [2] A. Feshke, G. Fettweis, J. Malmudin, and G. Biczok, "The global footprint of mobile communications: the ecological and economic perspective," *IEEE Communications Magazine*, vol. 49, no. 8, pp. 55–62, 2011.
- [3] R. Mahapatra, Y. Nijsure, G. Kaddoum, N. Ul Hassan, and C. Yuen, "Energy efficiency tradeoff mechanism towards wireless green communications: a survey," *IEEE Communication Surveys and Tutorials*, vol. 18, no. 1, pp. 686–705, 2016.
- [4] Z. Hasan, H. Boostanimehr, and V. K. Bhargava, "Green cellular networks: a survey, some, research issues and challenges," *IEEE Communication Surveys and Tutorials*, vol. 13, no. 4, pp. 524–540, 2011.
- [5] J. Xu, C. Liu, Y. Yang, X. Ge, and T. Chen, "An overview of energy efficiency analytical models in communication networks," in *IEEE International Conference on Wireless Communications and Signal Processing (WCSP)*, pp. 1–6, Suzhou, China, October 2010.
- [6] A. P. Blanzino, C. Chaudet, D. Rossi, and J. Rougier, "A survey of green networking research," *IEEE Communication Surveys and Tutorials*, vol. 14, no. 1, pp. 3–20, 2012.
- [7] M. R. Islam, M. R. Islam, and M. R. A. Beg, "Renewable energy resources and technologies practice in Bangladesh," *Renewable and Sustainable Energy Reviews*, vol. 12, no. 2, pp. 299–343, 2008.
- [8] M. Chandel, G. D. Agrawal, S. Mathur, and A. Mathur, "Techno-economic analysis of solar photovoltaic power plant for garment zone of Jaipur city," *Elsevier Journal of Case Studies in Thermal Engineering*, vol. 2, no. 1, pp. 1–7, 2013.
- [9] T. Pavlovic, D. Milosavljevic, I. Radonjic, L. Pantic, A. Radivojevic, and M. Pavlovic, "Possibility of electricity generation using PV solar plants in Serbia," *Elsevier Journal of Renewable and Sustainable Energy Reviews*, vol. 20, no. 1, pp. 201–218, 2013.
- [10] K. Son, H. Kim, Y. Yi, and B. Krishnamachari, "Base station operation and user association mechanisms for energy-delay tradeoffs in green cellular networks," *IEEE Journal on Selected Areas in Communications*, vol. 29, no. 8, pp. 1525–1536, 2011.
- [11] R. Bolla, R. Bruschi, F. Davoli, and F. Gucciatti, "Energy efficiency in the future internet: a survey of existing approaches and trends in energy aware fixed network infrastructure," *IEEE Communication Surveys and Tutorials*, vol. 13, no. 2, pp. 223–244, 2011.
- [12] M. Ismail, W. Zhuang, E. Serpedin, and K. Qaraqe, "A survey of green mobile networking: from the perspectives of network operators and mobile users," *IEEE Communication Surveys and Tutorials*, vol. 17, no. 3, pp. 1535–1556, 2015.
- [13] C. Peng, S. B. Lee, S. Lu, H. Luo, and H. Li, "Traffic-driven power saving in operational 3G cellular networks," in *ACM International Conference on Mobile Computing and Networking (MobiCom)*, pp. 121–132, 2011.
- [14] T. Chen, H. Kin, and Y. Yang, "Energy efficiency metrics for green wireless communications," in *IEEE International Conference on Wireless Communications and Signal Processing (WCSP)*, pp. 1–6, Suzhou, China, October 2010.
- [15] G. Auer, I. Godor, L. Hevizi et al., "Enablers for energy efficient wireless networks," in *IEEE Vehicular Technology Conference (VTC)—Fall*, pp. 1–5, Ottawa, Canada, September 2010.

- [16] Y. Zhang, P. Chowdhury, M. Tornatore, and B. Mukherjee, "Energy efficiency in telecom optical networks," *IEEE Communication Surveys and Tutorials*, vol. 12, no. 4, pp. 441–458, 2010.
- [17] L. Cai, H. Poor, Y. Liu, T. Luan, X. Shen, and J. Mark, "Dimensioning network deployment and resource management in green mesh networks," *IEEE Wireless Communications*, vol. 18, no. 5, pp. 58–65, 2011.
- [18] 3GPP TR 36.913, "LTE; Requirements for further advancements for evolved universal terrestrial radio access (E-UTRA) (LTE-advanced)," *Technical Report*, Version 10.0.0, Release 10, 2011.
- [19] I. F. Akyildiz, D. M. G. Estevez, and E. C. Reyes, "The evolution of 4G cellular systems: LTE-advanced," *Physical Communication*, vol. 3, no. 4, pp. 217–244, 2010.
- [20] J. Lee, Y. Kim, H. Lee et al., "Coordinated multipoint transmission and reception in LTE-Advanced systems," *IEEE Communications Magazine*, vol. 50, no. 11, pp. 44–50, 2012.
- [21] R. Irmer, H. Droste, P. Marsch et al., "Coordinated multipoint: concepts, performance and field trial results," *IEEE Communications Magazine*, vol. 49, no. 2, pp. 102–111, 2011.
- [22] A. Jahid, A. B. Shams, and M. F. Hossain, "Energy cooperation among BS with hybrid power supply for DPS CoMP based cellular networks," in *IEEE Conference on Electrical, Computer and Telecommunication Engineering (ICECTE)*, pp. 1–4, Rajshahi, Bangladesh, 2016.
- [23] D. Lee, H. Seo, B. Clerckx et al., "Coordinated multipoint transmission and reception in LTE-Advanced: deployment scenarios and operational challenges," *IEEE Communications Magazine*, vol. 50, no. 2, pp. 148–155, 2012.
- [24] White Paper, "Improving energy efficiency, lower CO<sub>2</sub> emission and TCO," *Huawei Energy Efficiency Solution*, Huawei Technologies Co. Ltd., pp. 1–13, 2011.
- [25] Vodafone, "Carbon and energy," <http://www.vodafone.com/content/index/ukcorporateresponsibility/greener/carbon+energy.html>.
- [26] 3GPP TR 36.902 ver. 9.3.1 Rel. 9, "Evolved universal terrestrial radio access network (E-UTRAN); self-configuring and self-optimizing network (SON): use cases and solutions," 2011.
- [27] H. Tabassum, U. Siddique, E. Hossain, and M. J. Hossain, "Downlink performance of cellular systems with base station sleeping, user association, and scheduling," *IEEE Transactions on Wireless Communications*, vol. 13, no. 10, pp. 5752–5767, 2014.
- [28] G. Cili, H. Yanikomeroglu, and F. R. Yu, "Cell switch off technique combined with coordinated multi-point transmission for energy efficiency in beyond LTE cellular networks," in *IEEE ICC Workshop on Green Communications and Networking*, pp. 5931–5935, Ottawa, Canada, June 2012.
- [29] M. F. Hossain, K. S. Munasinghe, and A. Jamalipour, "Energy-aware dynamic sectorization of base stations in multi-cell OFDMA networks," *IEEE Wireless Communications Letters*, vol. 2, no. 6, pp. 587–590, 2013.
- [30] M. F. Hossain, K. S. Munasinghe, and A. Jamalipour, "Distributed inter-BS cooperation aided energy efficient load balancing for cellular networks," *IEEE Transactions on Wireless Communications*, vol. 12, no. 11, pp. 5929–5939, 2013.
- [31] J. Xu, Y. Zhang, M. Zukerman, and E. K.-N. Yung, "Energy-efficient base stations sleep mode techniques in green cellular networks: a survey," *IEEE Communication Surveys and Tutorials*, vol. 17, no. 2, pp. 803–826, 2015.
- [32] Y. K. Chia, S. Sun, and R. Zhang, "Energy cooperation in cellular networks with renewable powered base stations," *IEEE Transactions on Wireless Communications*, vol. 13, no. 12, pp. 6996–7010, 2014.
- [33] T. Han and N. Ansari, "On optimizing green energy utilization for cellular networks with hybrid supplies," *IEEE Transactions on Wireless Communications*, vol. 12, no. 8, pp. 3872–3882, 2013.
- [34] J. Xu, Y. Guo, and R. Zhang, "CoMP meets energy harvesting: a new communication and energy cooperation paradigm," in *IEEE Global Communications Conference (GLOBECOM)*, pp. 2508–2513, Atlanta, GA, USA, December 2013.
- [35] "System advisor model (SAM)," *National Renewable Energy Laboratory (NREL), U.S. Department of Energy*, <https://sam.nrel.gov/>.
- [36] "Mobile internet phenomena report," 2010, <http://www.sandvine.com/downloads/documents/2010GlobalInternetPhenomenaReport.pdf>.
- [37] J. Lorincz, T. Garma, and G. Petrovic, "Measurements and modeling of base station power consumption under real traffic loads," *Sensors*, vol. 12, no. 4, pp. 4281–4310, 2012.
- [38] H. Holtkamp, G. Auer, V. Giannini, and H. Hass, "A parameterized base station power model," *IEEE Communications Letters*, vol. 17, no. 11, pp. 2033–2035, 2013.
- [39] EARTH, "EARTH deliverable D2.4, most suitable efficiency metrics and utility functions," 2012, [https://bscw.ict-earth.eu/pub/bscw.cgi/d70454/EARTH\\_WP2\\_D2.4.pdf](https://bscw.ict-earth.eu/pub/bscw.cgi/d70454/EARTH_WP2_D2.4.pdf).

## Research Article

# Synergetic Control of Grid-Connected Photovoltaic Systems

**Junjie Qian, Kaiting Li, Huaren Wu, Jianfei Yang, and Xiaohui Li**

*School of Electrical and Automation Engineering, Nanjing Normal University, Nanjing 210042, China*

Correspondence should be addressed to Xiaohui Li; 61011@njnu.edu.cn

Received 8 October 2016; Revised 26 November 2016; Accepted 16 January 2017; Published 29 March 2017

Academic Editor: Md. Rabiul Islam

Copyright © 2017 Junjie Qian et al. This is an open access article distributed under the Creative Commons Attribution License, which permits unrestricted use, distribution, and reproduction in any medium, provided the original work is properly cited.

It is important to improve the dynamic performance and the low-voltage ride-through (LVRT) capability of a grid-connected photovoltaic (PV) system. This paper presents synergetic control for the control of a grid-connected PV system. Modeling of a grid-connected PV system is described, and differential-algebra equations are obtained. Two control strategies are used in normal operation and during LVRT of a PV system. Practical synergetic controllers with two control strategies are synthesized. The mathematical expressions are derived for computing control variables. The design of the synergetic controllers does not require the linearization of the grid-connected PV system. A grid-connected PV system with synergetic controllers is simulated in Simulink surroundings. The control performance is studied in normal operation and during LVRT. Simulation results show that the synergetic controllers are robust and have good dynamic characteristics under different operation states.

## 1. Introduction

The world is faced with serious problems of energy depletion and environmental pollution. The research and development of photovoltaic (PV) technologies have become a hot topic in the world [1]. Solar PV is now used around the world as an important technology for the conversion of solar energy because of its cleanliness and security. The solar PV capacity increased 25% over 2014 to a record 50 GW, lifting the global total to 227 GW. The solar PV industry is one of the fastest growing high-tech industries [2].

The control of a PV system is an important and difficult task. A grid-connected PV system mainly includes maximum power point tracking (MPPT) and the control of the DC-AC converter. Much research on MPPT has been conducted, and various MPPT algorithms have been proposed. The maximum power point (MPP) may be located by the perturbation and observation (P&O) algorithms [3], the incremental conductance (InC) algorithm [4], and the artificial neural network algorithm [5].

Reference [6] proposes a modified InC algorithm. The algorithm eliminates the division calculations involved in its structure and improves the variable step size, which only depends on the PV power change. Reference [7] improves P&O algorithm. This approach combines ant

colony optimization with the traditional P&O method to yield faster and efficient convergence. This improved P&O algorithm can recognize global MPP under partially shaded conditions. A new MPPT algorithm is proposed in [8]. This scheme uses a gray wolf optimization technique to track the global peak of a PV array under partial shading conditions. It can solve the problems such as lower tracking efficiency, steady-state oscillations, and transients as encountered in P&O.

A two-stage three-phase grid-connected PV system in [9] contains a DC-DC boost converter and a DC-AC VSC converter. Pulse width modulator (PWM) signals fire the converters. The DC-AC VSC control system has an external voltage control loop and an internal current control loop. The external control loop regulates the DC link voltage, and the internal control loop regulates grid currents. The grid currents are transformed into  $d$ -axis and  $q$ -axis currents to accomplish vector control. Two control loops adopt the proportional-integral (PI) algorithm. Reference [10] presents a novel sliding-mode (SM) control for grid-connected PV systems. A systematic adaptive procedure to calculate the band of the hysteresis comparators is developed to improve the performance of the SM controller. A vector controller can keep the maximum power delivery of the PV system. Reference [11] uses a probabilistic wavelet fuzzy neural

network (PWFNN) to structure the reactive power controller for a grid-connected PV system. The balance of the active power between the PV array and the DC-AC converter during grid faults is controlled by the DC link voltage. The controller can improve the operation of the grid-connected PV system during LVRT. Reference [12] suggests injecting the maximum rated current to maximize the inverter power capability during LVRT. The strategy combines a proper balance between positive- and negative-current sequences. High- and low-power production scenarios limit the inverter output current to the maximum rated value and avoid active power oscillations. Reference [13] presents a new adaptive PI controller using the continuous mixed p-norm (CMPN) algorithm for enhancing the LVRT capability of grid-connected PV systems. The adaptive PI controller is used to control the DC-AC converter. The gains of the PI controller are changed by the CMPN algorithm online without the need to fine-tune or optimize.

Reference [14] reviews the general synergetic control design procedure. Synergetic control is applied to a DC-DC boost converter, deriving a basic control law. An adaptive control strategy gives better trade-off between large-signal stability and load step response time. Reference [15] introduces a practical synergetic controller to regulate the buck converters that coordinate pulse current charging of batteries. Simulation and experiment results show that the synergetic controller is robust for such nonlinear dynamic systems and achieves better performance than the standard PI controller.

This paper presents a design for the synergetic controllers for an internal current control loop of a three-phase grid-connected PV system. The theory of synergetic control is first described. Modeling of a grid-connected PV system is introduced, and differential-algebra equations are obtained. Synergetic controllers are derived in detail for normal operation and during LVRT of a PV system. Two control strategies are used during normal and LVRT operations of PV systems. The design of a synergetic controller does not require linearization of the PV system. The parameters  $T_1$  and  $T_2$  of the two synergetic controllers are the same, and  $T_1$  equals  $T_2$ . The parameters of the synergetic controllers are easy to determine, and the proposed control schemes are easy to achieve. An example given in Matlab is adapted according to the synergetic controllers for assessing the performance of synergetic control of the grid-connected PV system. The synergetic control is chatter-free, and the simulation results demonstrate the effectiveness of the proposed control schemes.

## 2. Synergetic Control Theory

Synergetic control is a state space control method based on modern mathematics. Synergetic control is applicable to the control of nonlinear, dynamic, and high-dimensional systems. It can be perfectly analyzed by mathematical expressions.

The nonlinear state equation of a controlled system is

$$\dot{x} = f(x, u, t), \quad (1)$$

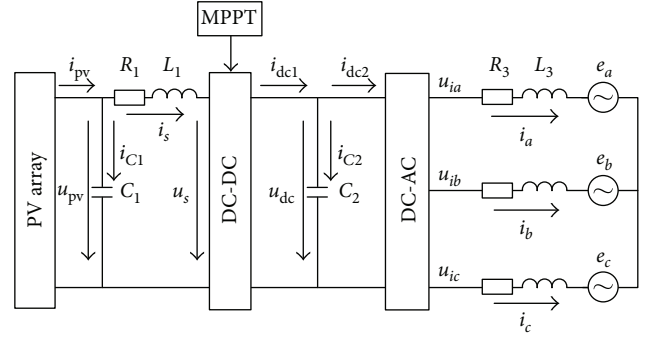


FIGURE 1: Main circuit of a grid-connected PV system.

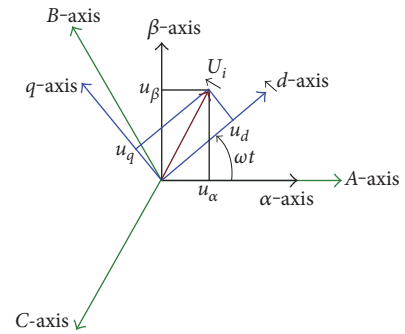


FIGURE 2: Reference frames.

where  $x$  is the state vector of the controlled system  $\mathfrak{R}^n$ ,  $f(\cdot)$  is a continuous nonlinear function, and  $u$  is the control vector of  $\mathfrak{R}^m$  ( $m \leq n$ ).

The macrovariables are defined for each input channel as a function of the state variables. The synergetic controller directs the system to move into the manifold from any initial motion point

$$\psi(x, t) = 0, \quad (2)$$

where  $\psi$  is the macrovector of  $\mathfrak{R}^k$  ( $0 < k \leq m$ ).

The dynamic evolution of the macrovariable towards the manifolds is defined as follows [14]:

$$T \dot{\psi} + \psi = 0, \quad (3)$$

where  $T$  defines the rate of convergence of the system.

Substituting from (2) into (3) yields

$$T \frac{\partial \psi}{\partial x} \dot{x} + \psi = 0. \quad (4)$$

The control vector  $u$  can be acquired by substituting (1) into (4). The system can be controlled to stay in the desired manifold.

## 3. Modeling of the Grid-Connected PV System

The main circuit of the two-stage grid-connected PV system is described in Figure 1. A PV array is connected to a power

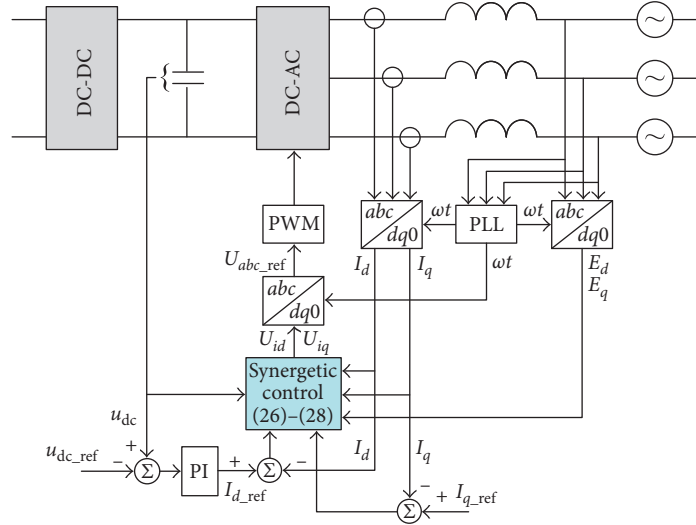


FIGURE 3: Synergetic control scheme of the PV system in normal operation.

grid via a DC boost converter and a three-phase voltage source converter (VSC) [9].

The differential equations (5), (6), (7), and (8) can be written according to Figure 1.

$$C_1 \frac{du_{pv}}{dt} = i_{pv} - i_s, \quad (5)$$

$$u_{pv} = R_1 i_s + L_1 \frac{di_s}{dt} + u_s, \quad (6)$$

$$C_2 \frac{du_{dc}}{dt} = i_{dc1} - i_{dc2}, \quad (7)$$

$$U_{iabc} - E_{abc} = R_3 I_{abc} + L_3 \frac{dI_{abc}}{dt}, \quad (8)$$

where

$$\begin{aligned} U_{iabc} &= \begin{bmatrix} u_{ia} \\ u_{ib} \\ u_{ic} \end{bmatrix}, \\ E_{abc} &= \begin{bmatrix} e_a \\ e_b \\ e_c \end{bmatrix}, \\ I_{abc} &= \begin{bmatrix} i_a \\ i_b \\ i_c \end{bmatrix}, \end{aligned} \quad (9)$$

$E_{abc}$  is the grid voltage,  $U_{iabc}$  is the output voltage of the DC-AC VSC converter, and  $I_{abc}$  is the alternating current.

Equation (8) is based on a three-phase ( $abc$ ) reference frame.  $abc$ ,  $\alpha\beta 0$ , and  $dq0$  reference frames are shown in Figure 2 [16].

Equation (8) is transformed into (10) from the  $abc$  reference frame to the  $dq0$  rotating reference frame using the sinus-based Park transformation.

$$U_{idq0} - E_{dq0} = R_3 I_{dq0} + L_3 \frac{dI_{dq0}}{dt} + L_3 \begin{bmatrix} -\omega I_q \\ \omega I_d \\ 0 \end{bmatrix}, \quad (10)$$

where  $U_{idq0} = PU_{iabc}$ ,  $E_{dq0} = PE_{abc}$ ,  $I_{dq0} = PI_{abc}$ , and  $P$  is the Park transformation matrix given in (11). Consider

$$P = \frac{2}{3} \begin{bmatrix} \sin(\omega t) & \sin\left(\omega t - \frac{2\pi}{3}\right) & \sin\left(\omega t + \frac{2\pi}{3}\right) \\ \cos(\omega t) & \cos\left(\omega t - \frac{2\pi}{3}\right) & \cos\left(\omega t + \frac{2\pi}{3}\right) \\ \frac{1}{2} & \frac{1}{2} & \frac{1}{2} \end{bmatrix}. \quad (11)$$

Equation (10) may be written in (12) and (13). Consider

$$L_3 \frac{dI_d}{dt} = -R_3 I_d + \omega L_3 I_q - E_d + U_{id} = U_{3d} + U_{id}, \quad (12)$$

$$L_3 \frac{dI_q}{dt} = -R_3 I_q - \omega L_3 I_d - E_q + U_{iq} = U_{3q} + U_{iq}, \quad (13)$$

where

$$U_{3d} = -R_3 I_d + \omega L_3 I_q - E_d, \quad (14)$$

$$U_{3q} = -R_3 I_q - \omega L_3 I_d - E_q. \quad (15)$$

$U_{id}$  and  $U_{iq}$  in (12) and (13) are control variables that control the DC-AC VSC converter.

The MPPT algorithm computes the duty cycle to control the DC boost converter. The relationship of inputs and outputs of the DC boost converter is depicted by (16) and (17). Consider

$$i_{dc1} = (1 - D)i_s, \quad (16)$$

$$u_s = (1 - D)u_{dc}, \quad (17)$$

where  $D$  is the duty cycle of the DC boost converter.

The instantaneous active and reactive powers are defined by (18) and (19). Consider

$$p = E_d I_d + E_q I_q, \quad (18)$$

$$q = -E_d I_q + E_q I_d. \quad (19)$$

Selecting  $E_q = 0$ , (18) and (19) change into the two following equations:

$$p = E_d I_d, \quad (20)$$

$$q = -E_d I_q. \quad (21)$$

The model above can be used to design the synergetic control of the grid-connected PV system.

#### 4. Synergetic Control of a Grid-Connected PV System in Normal Operation

Control strategies of the DC boost converter and the DC-AC VSC converter in the grid-connected PV system must be made. MPPT is implemented in the DC boost converter in normal operation. There are a number of MPPT algorithms; however, this paper does not analyze them.

The DC-AC VSC converter is controlled using the synergetic control presented in this paper. The control variables  $U_{id}$  and  $U_{iq}$  in (12) and (13) are derived by synergetic control theory.

The reference value of  $I_d$  may be obtained from the external voltage control loop.

$$I_{d\_ref} = \left( K_P + \frac{K_i}{s} \right) (u_{dc} - u_{dc\_ref}) = K_P (u_{dc} - u_{dc\_ref}) + I_u, \quad (22)$$

where  $I_u = K_i/s(u_{dc} - u_{dc\_ref})$ ; that is,

$$\frac{dI_u}{dt} = K_i (u_{dc} - u_{dc\_ref}), \quad (23)$$

where  $K_P$  is the gain of the proportional term,  $K_i$  is the gain of the integral term,  $u_{dc\_ref}$  is the reference value of the DC voltage  $u_{dc}$ , and subscript ref denotes a reference value.

There are 2 control variables, and therefore, 2 macrovariables must be selected. The first macrovariable is

$$\psi_1 = I_{d\_ref} - I_d = K_P (u_{dc} - u_{dc\_ref}) + I_u - I_d. \quad (24)$$

Substituting (24) into (4), (25) is obtained:

$$T_1 \left( K_P \frac{du_{dc}}{dt} + \frac{dI_u}{dt} - \frac{dI_d}{dt} \right) + \psi_1 = 0. \quad (25)$$

Substituting (12), (23), and (24) into (25), the first control variable is computed by (26) as follows:

$$U_{id} = K_P L_3 \frac{du_{dc}}{dt} + K_i L_3 (u_{dc} - u_{dc\_ref}) + \frac{L_3}{T_1} (I_{d\_ref} - I_d) - U_{3d}. \quad (26)$$

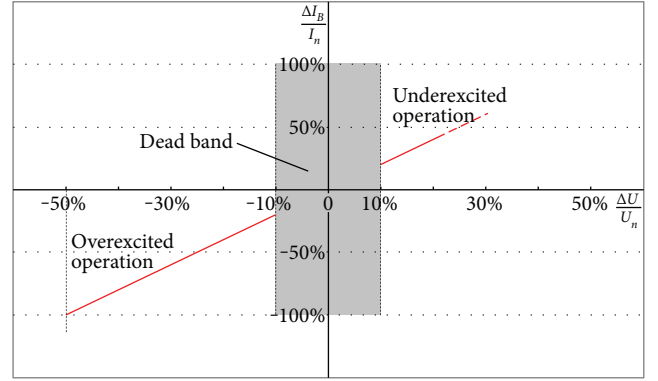


FIGURE 4: Principle of voltage support in the event of grid faults.

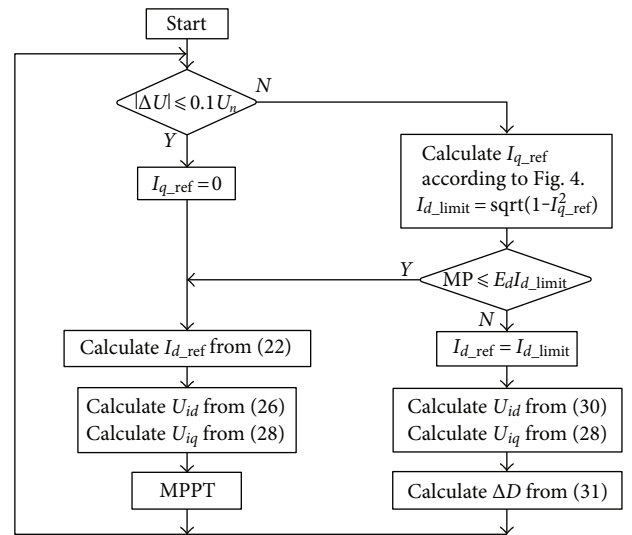


FIGURE 5: Synergetic control strategies of the PV system.

The second macrovariable is selected

$$\psi_2 = I_{q\_ref} - I_q, \quad (27)$$

where  $I_{q\_ref}$  is a constant.

Substituting (27) into (4) and considering (13), the second control variable is as follows:

$$U_{iq} = \frac{L_3}{T_2} (I_{q\_ref} - I_q) - U_{3q}. \quad (28)$$

The control variables  $U_{id}$  and  $U_{iq}$  are computed by (26) and (28), respectively, to guarantee system stability in normal operation. The synergetic control scheme of the grid-connected PV system is shown in Figure 3.

#### 5. Synergetic Control during LVRT

The PV system should stay connected and support the grid with reactive power during the voltage dip. Therefore, the reference value of  $I_q$  is  $I_{q\_ref} = \text{const.}$ , depending on the voltage magnitude. Figure 4 depicts the principle of voltage support in the event of grid faults [17].

The abscissa in Figure 4 stands for  $\Delta U/U_n$ , and the ordinate is  $\Delta I_B/I_n$ .  $\Delta U = U - U_0$  and  $\Delta I_B = I_B - I_{B0}$ , where  $U$

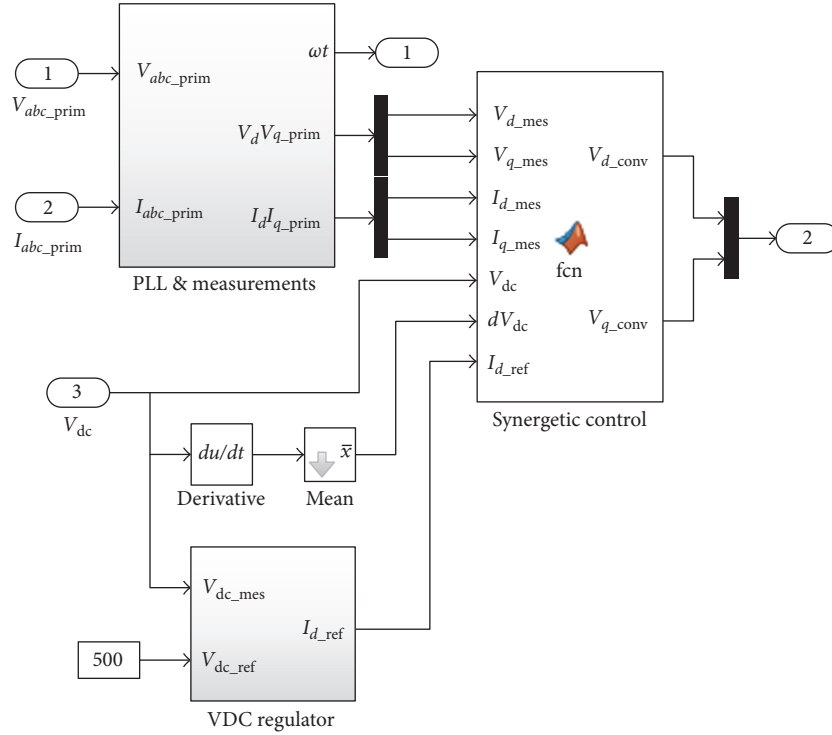


FIGURE 6: VSC main controller.

is the present voltage during the fault,  $U_n$  is the rated voltage,  $U_0$  is voltage before the fault,  $I_B$  is the reactive current,  $I_n$  is the rated current, and  $I_{B0}$  is the reactive current before the fault. If a voltage dip is more than 10% of the rated voltage, the generator should provide a reactive current amounting to at least 2% of the rated current for each percent of the voltage dip within 20 ms after fault recognition [17]. If a voltage dip is more than 50% of the rated voltage, the generator must inject the grid with a reactive power of 100% of the rated current.

The limitation of  $I_d$  is  $I_{d\_limit} = \sqrt{1 - I_{q\_ref}^2}$  pu, so the current will not be greater than the rated current.

If the maximum power of the PV array at MPP is less than the power  $E_d I_{d\_limit}$ , the maximum power can be injected into the grid with  $I_d < I_{d\_limit}$ . A MPPT is used during LVRT to obtain the maximum power and economic benefits, and the control strategies are the same as those in normal operation.

If the maximum power of the PV array at MPP is more than the power  $E_d I_{d\_limit}$ ,  $I_{d\_ref} = I_{d\_limit}$  is set, and the power output of the PV array equals  $E_d I_{d\_limit}$  for the power balance. The following control strategies are used:

The first macrovariable is selected as

$$\psi_1 = I_{d\_ref} - I_d. \quad (29)$$

Substituting (29) into (4) and considering (12), the first control variable is computed as follows:

$$U_{id} = \frac{L_3}{T_1} (I_{d\_ref} - I_d) - U_{3d}. \quad (30)$$

Equation (28) is also used for the second control variable during LVRT.

A MPPT is not used, and the duty cycle  $D$  is determined by a PI controller to regulate the DC link voltage.

$$\Delta D = \left( K_{PD} + \frac{K_{ID}}{s} \right) (u_{dc\_ref} - u_{dc}), \quad (31)$$

$$D = D_0 + \Delta D, \quad (32)$$

where  $D_0$  is the initial value of  $D$ .

The duty cycle of the DC boost converter is determined by (31) and (32) during LVRT. The DC-AC VSC converter is controlled on the basis of (28) and (30).

The control strategies described above are shown in Figure 5.

Equations (26) and (30) are derived according to the synergetic control algorithm.  $I_{d\_ref}$  is variable and is computed by (22) in normal operation. Consequently, (26) is obtained for the control of the PV system in normal operation.  $I_{d\_ref}$  is a constant, and (30) is derived for the second control strategy during LVRT. Equations (26) and (30) are used under different operating conditions of the grid-connected PV system.

The DC link voltage  $u_{dc}$  should remain stable to maintain good operation of the PV system. This requires a power balance in the PV system. If the power injected into the grid by the DC-AC converter is less than the output power of the PV array,  $u_{dc}$  will increase. If the output power of the converter is the same as the output power of the PV array,  $u_{dc}$  will not change. The two control strategies can satisfy

the power balance in the PV system in normal operation and during a LVRT.

The PV array works at the MPP because of the MPPT in normal operation. If the output power of the converter is less than the output power of the PV array and  $u_{dc}$  increases, the DC voltage regulator will generate greater  $I_{d\_ref}$  on the basis of (22). The synergetic control will result in more output power of the converter and achieve a power balance in the PV system after the regulation process.

The synergetic control maintains the output power  $E_d I_{d\_limit}$  of the converter for the second control strategy during LVRT. If the output power of the PV array is greater than  $E_d I_{d\_limit}$  and  $u_{dc}$  increases, the DC voltage regulator will give a smaller  $D$  according to (31) and (32). The voltage of the PV array will increase according to (17), and its output power will decrease due to the power-voltage characteristics of the PV array. The power balance in the PV system will be achieved once more, and  $u_{dc}$  will return to its reference value.

The DC-AC converter may be damaged due to the large current that passes through it. The two control strategies can prevent the converter from overcurrent in normal operation and during LVRT.

## 6. Case Studies

Matlab software provides an example titled *Detailed Model of a 100-kW Grid-Connected PV Array* [9]. The controllers of the example are adapted to assess the performance of synergetic control of the grid-connected PV system.

The example includes a PV array with an open-circuit voltage of 321 V.  $u_{dc\_ref}$  is 500 V, and the rated AC voltage is 260 V. A distribution transformer has a voltage ratio of 25 kV/260 V.

**6.1. Normal Operation Simulation.** MPPT used in the case study is based on incremental conductance with an integral controller that can ensure that the system operates in MPP when the radiation intensity and temperature change rapidly.

The DC-AC converter is controlled using a synergetic control scheme. Equations (26) and (28) are rewritten according to the symbols in the Matlab example [9]:

$$V_{d\_conv} = K_p L_3 \frac{dV_{dc}}{dt} + K_i L_3 (V_{dc} - V_{dc\_ref}) + \frac{L_3}{T_1} (I_{d\_ref} - I_d) + R_3 I_{d\_ref} - \omega L_3 I_{q\_ref} + V_{d\_mes}, \quad (33)$$

$$V_{q\_conv} = \frac{L_3}{T_2} (I_{q\_ref} - I_q) + R_3 I_{q\_ref} + \omega L_3 I_{d\_ref} + V_{q\_mes}. \quad (34)$$

Figure 6 shows the VSC main controller containing synergetic control.

The VDC regulator in Figure 6 is constructed on the basis of (22). The inputs of the PLL and measurements block are primary voltages  $V_{abc\_prim}$  and currents  $I_{abc\_prim}$  of the distribution transformer. This block tracks the frequency

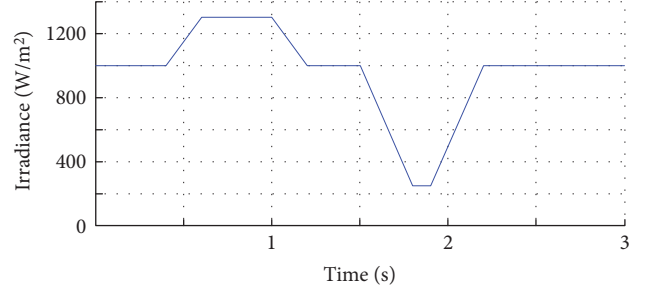


FIGURE 7: Sun irradiance.

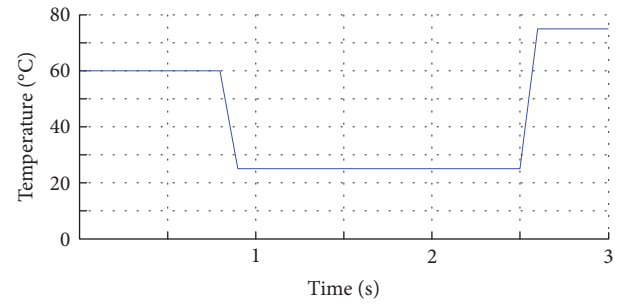


FIGURE 8: Temperature.

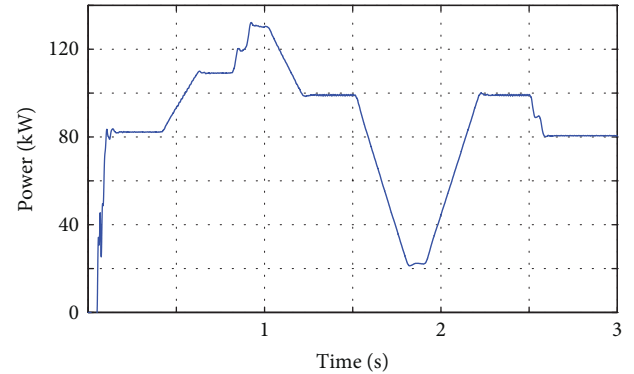


FIGURE 9: PV array output power.

and phase of a sinusoidal three-phase signal and performs Park transformation from a three-phase ( $abc$ ) reference frame to a  $dq0$  reference frame. The synergetic control block in Figure 6 is a Matlab function block. It includes Matlab code. The code computes 2 control variables,  $V_{d\_conv}$  and  $V_{q\_conv}$ , with (33) and (34). The control variables are transformed into the reference values of three-phase voltages to generate PWM and control the VSC converters.

The parameters  $K_p = 0.2$ ,  $K_i = 150$ ,  $T_1 = 0.01$ , and  $T_2 = 0.01$  are selected and applied in (22), (33), and (34). The settings are  $V_{d\_ref} = 500$  V and  $I_{q\_ref} = 0$  for the simulation in normal operation. The standard test conditions are  $1000$  W/m<sup>2</sup> irradiance and  $25^\circ\text{C}$  temperature. The change of sun irradiance is shown in Figure 7. Figure 8 describes the change of temperature for the simulation.

The MPPT regulator changes the duty cycle to regulate the PV voltage for tracking maximum power. At  $t = 0.1$  s,

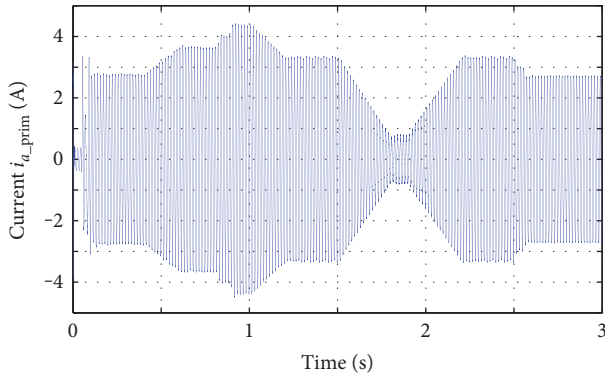
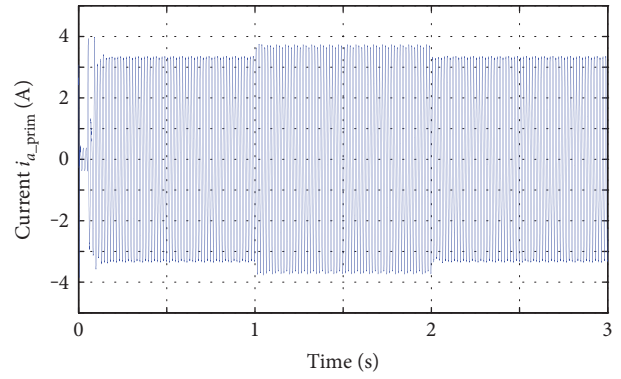
FIGURE 10: Primary current  $i_{a\_prim}$ .

FIGURE 12: Current increase.

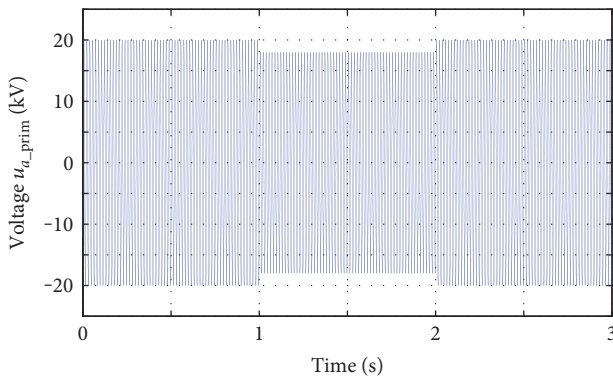


FIGURE 11: Bus voltage decrease.

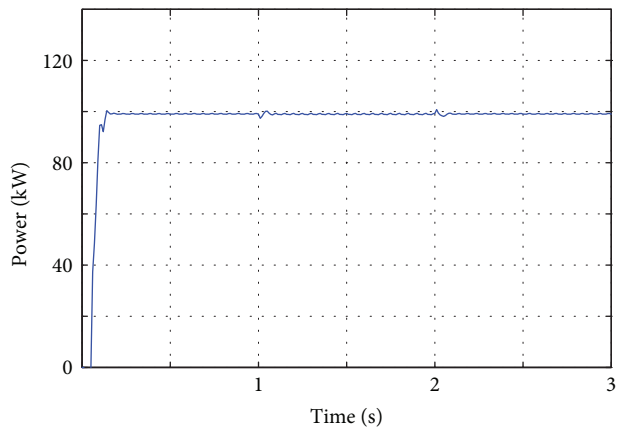


FIGURE 13: Power invariance.

the MPPT is enabled, and Figure 9 shows the PV array output power. Maximum power is 100.4 kW at the standard test conditions. VSC converters deliver the power to the grid by synergetic control.

The root mean square (RMS) of the primary voltage  $v_{a\_prim}$  of the distribution transformer is constant. The RMS of the current  $i_{a\_prim}$  is directly proportional to the power. Figure 10 shows the primary current  $i_{a\_prim}$  of the distribution transformer.

Figures 9 and 10 indicate that the grid-connected PV system can track maximum power and deliver the power to the grid when the radiation and temperature change rapidly. The system operates stably.

The bus voltage may change in normal operation. Simulation of voltage fluctuation is performed at the standard test conditions. Figure 11 depicts a 25 kV bus voltage  $v_{a\_prim}$ . The RMS of  $v_{a\_prim}$  decreases by 10% at  $t = 1$  sec.

The current  $i_{a\_prim}$  is shown in Figure 12.  $i_{a\_prim}$  increases when the bus voltage decreases.

The maximum power does not change because sun irradiance and temperature are constant at the standard test conditions. Figure 13 demonstrates that the power injected into the grid is almost constant during the grid voltage fluctuation. This means that the synergetic control performs well in normal operation.

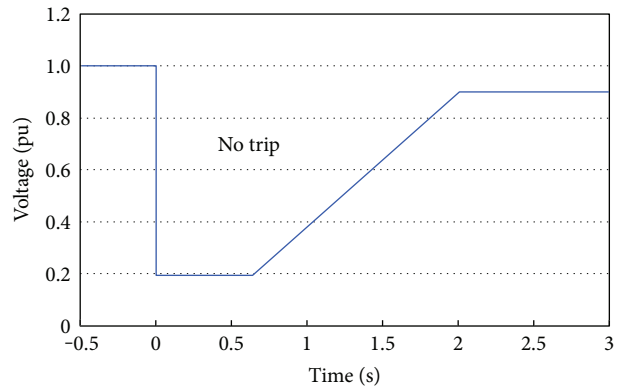


FIGURE 14: LVRT requirement.

**6.2. LVRT Simulation.** LVRT is the capability of electric generators to stay connected to the grid during short periods of voltage dip. LVRT is an important feature of the generator control system. There are several standards for LVRT requirements [17, 18]. Figure 14 shows the LVRT requirement in [19]. These requirements may be used for large solar power installations.

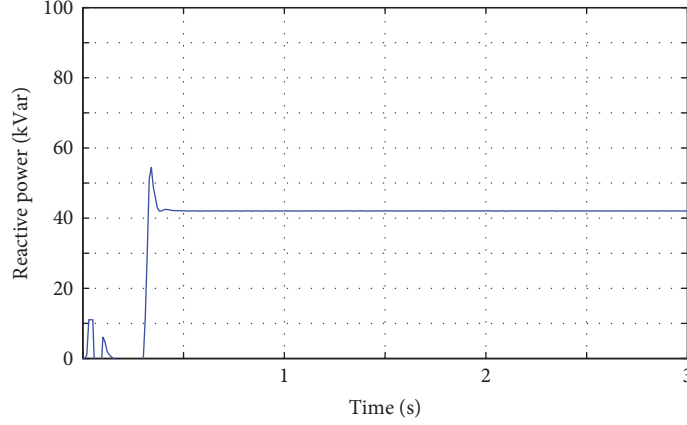


FIGURE 15: Reactive power injected into the grid at a 30% decrease of the bus voltage.

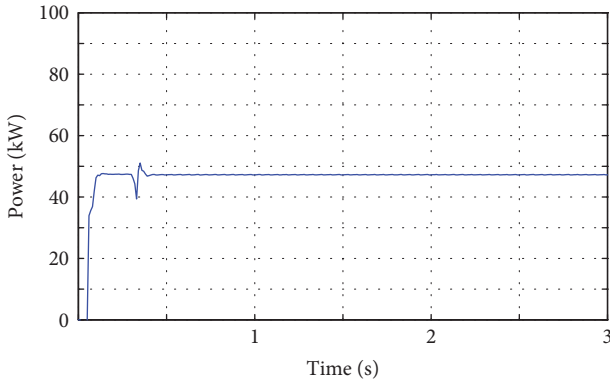


FIGURE 16: Active power injected into the grid at a 30% decrease of grid voltage.

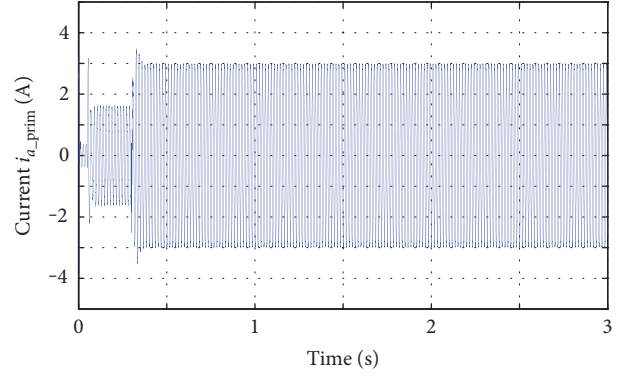


FIGURE 17: Primary current at a 30% decrease of grid voltage.

Three cases are used to test the performances of the synergetic control during a LVRT. The three-phase fault block in Simulink is connected in utility grid to simulate a three-phase short circuit with arc resistances.

The feature of the PV system is tested first when the bus voltage decreases by 30% due to a grid fault. The reference value of the reactive current  $I_q$  is  $I_{q\_ref} = -0.6$  pu on the basis of Figure 4. The limitation of  $I_d$  is  $I_{d\_limit} = 0.8$ , and the power is  $E_d I_{d\_limit} = 0.56$  pu. The maximum power of the PV array at MPP is 0.48 pu when it is simulated at an irradiance of  $500 \text{ W/m}^2$  and a temperature of  $25^\circ\text{C}$ . The first control strategy is used because the maximum power of the PV array at MPP is less than  $E_d I_{d\_limit}$ .  $I_{q\_ref} = -0.6$  is set; the other settings are equivalent to those used in the normal operation simulation. Equations (22), (33), and (34) and MPPT are used. The RMS of the voltage  $v_{a\_prim}$  decreases by 30% at  $t = 0.3$  s, and the simulation results are shown in Figures 15–17.

Figure 15 depicts the reactive power injected into the grid. The PV system provides the grid with a reactive power of 42 kVar during the LVRT.

The active power injected into the grid is shown in Figure 16. The injected active power is 47.2 kW when the reactive power injected into the grid is 42 kVar at a 30% decrease of the grid voltage. The maximum power of the

PV array at MPP is delivered to the grid, and the solar energy is fully utilized.

The rated primary current is 3.3 A. Figure 17 shows that the primary current is less than its rated value. Therefore, the PV system may stay connected to the grid and provide the grid with 47.2 kW and 42 kVar at a 30% decrease of the grid voltage due to grid fault.

Then, simulations will test the performances of the synergetic control when the grid voltage decreases to 0.2 pu. The second control strategy is used because  $I_{q\_ref} = -1$  according to Figure 4 and  $I_{d\_limit} = 0$ . The duty cycle  $D$  is computed according to (31) and (32). Equation (30) is rewritten using the symbols in [9]:

$$V_{d\_conv} = \frac{L_3}{T_1} (I_{d\_ref} - I_d) + R_3 I_{d\_ref} - \omega L_3 I_{q\_ref} + V_{d\_mes}. \quad (35)$$

Equations (31), (32), (34), and (35) are used to compute the control variables for controlling the DC boost converter and the VSC converters during LVRT. The parameters are  $K_{PD} = 0.01$ ,  $K_{iD} = 0.1$ ,  $T_1 = 0.01$ , and  $T_2 = 0.01$ . The settings are  $V_{d\_ref} = 500 \text{ V}$ ,  $I_{q\_ref} = -1$ , and  $I_{d\_ref} = 0$  pu.

A three-phase short circuit occurs in the power distribution system at  $t = 0.3$  sec for the LVRT simulation. The bus voltage decreases to 0.2 pu during short circuit.  $v_{a\_prim}$  and

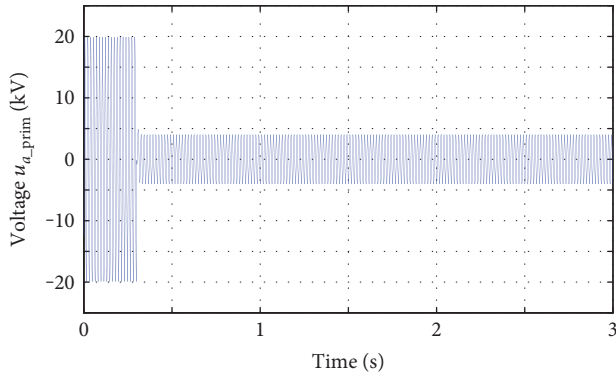


FIGURE 18: 25 kV bus voltage during LVRT.

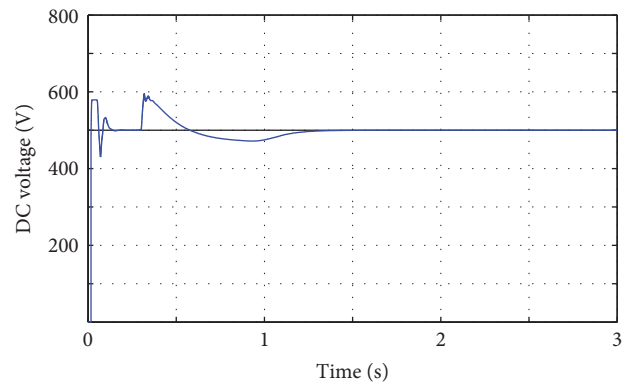


FIGURE 21: DC link voltage  $V_{dc}$ .

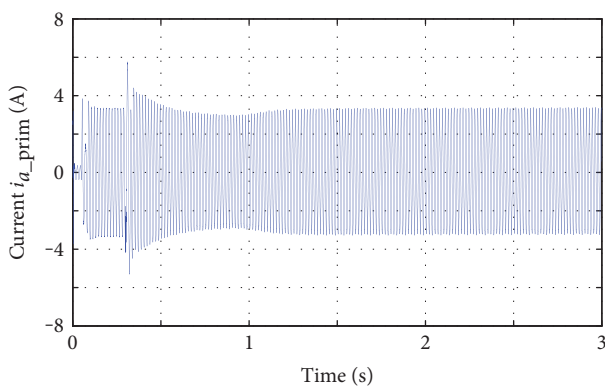


FIGURE 19: Primary current during LVRT.

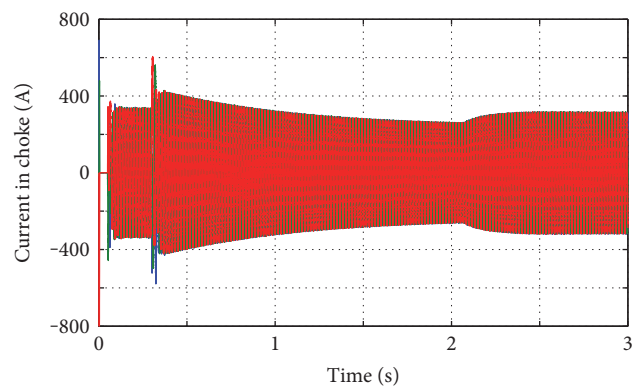


FIGURE 22: Three-phase currents flowing in the choke.

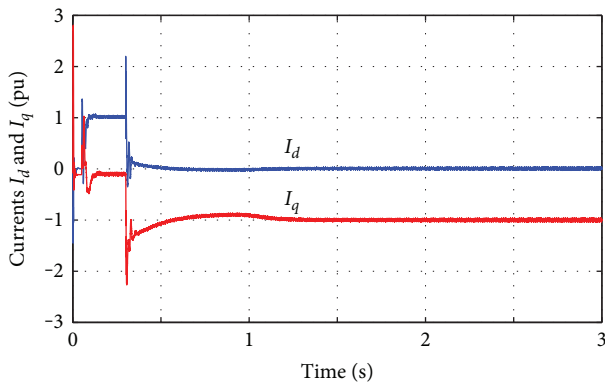


FIGURE 20: Currents  $I_d$  and  $I_q$  during LVRT.

$i_{a\_prim}$  are shown in Figures 18 and 19, respectively. The 25 kV bus voltage in Figure 18 decreases to 0.2 pu after  $t = 0.3$  sec.

Small fluctuations of primary current arise after the voltage dip. The peak value of  $i_{a\_prim}$  during LVRT is less than double of that in normal operation.

Currents  $I_d$  and  $I_q$  are depicted in Figure 20.  $I_d$  and  $I_q$  are regulated to 0 and  $-1$  pu, respectively, after the dip. The PV system stays connected and supports the grid with reactive power.

The DC link voltage  $V_{dc}$  is shown in Figure 21. It fluctuates slightly and then remains at 500 V after the dip.

Another simulation is made for testing the performance of the synergetic control at a bus voltage of 0.05 pu. The second control strategy is used. A three-phase short circuit is applied in the bus at  $t = 0.3$  sec, and the bus voltage decreases to 0.05 pu to simulate the voltage of the fault arc. The current settings are  $I_{d\_ref} = 0$  and  $I_{q\_ref} = -0.9$  pu, to avoid a large current. The reference value of current  $I_q$  is  $I_{q\_ref} = -1$  pu, to provide the grid with reactive power after  $t = 0.35$  sec. Figure 22 shows three-phase currents flowing in the choke. The maximum value of the current is less than 2.0 pu. Synergetic control can limit the current peak during LVRT.

The example in [9] has the current regulator with PI control and simulates only the normal operation of the PV system. The regulator from (31) and (32) is added to the example to simulate the LVRT of the PV system.  $I_{d\_ref} = 0$  and  $I_{q\_ref} = -1$  pu are fixed. Two parameters of the current regulator with PI control are changed from 0.3 and 20 (for normal operation) to 0.03 and 0.002, respectively, for LVRT. Therefore, parameter tuning of the current regulator with PI control is difficult. Chatter has been the main obstacle for sliding-mode control systems [10]. Probabilistic wavelet fuzzy neural networks (PWFNNs) include a membership layer, probabilistic layer, wavelet layer, and rule layer [11]. PWFNNs are very complicated, such that it is difficult to

determine the PWFNN parameters. The gains of the PI controller in [13] must be changed online using the CMPN algorithm for improving the LVRT capability of grid-connected PV systems.

The parameters of the synergetic controller described in this paper are invariant during normal operations and during LVRT, and parameter  $T_1$  equals  $T_2$ . There is no need to change the parameters of the synergetic controller with a complicated algorithm. Therefore, parameter tuning of the synergetic controller is easy, and the controller is sufficiently robust for use in the PV system. The design of the synergetic controller is simple and does not require linearization of the PV system. In addition, the proposed control schemes are easy to realize. The synergetic control is chatter-free and displays good static and dynamic performance.

Asymmetric short circuit faults may occur in power systems. Unbalanced grid voltages are comprised of positive, negative, and zero sequence voltage components. The zero sequence is not considered here because of three-wire systems. Unbalanced grid voltage sags will cause performance deterioration of the converter. Negative sequences result in DC-link voltage ripples and harmonic power. The positive and negative sequence currents should be controlled simultaneously to improve control performance. Reference [20] used separate current controllers for positive and negative sequences. Synergetic control may be used in two current controllers to control positive and negative sequence currents separately. It is possible to use synergetic control for improving the performance of PV systems during unbalanced voltage sags.

## 7. Conclusions

Solar PV is an important renewable energy technology and does not generate pollution. PV systems are developing rapidly, and most PV systems are grid-connected. Research on the control of grid-connected PV systems contributes to the improvement of the operation of the distribution network and the PV system.

Synergetic control can be used for the control of a grid-connected PV system. The design of a synergetic controller does not require the linearization of the PV system. The mathematical expressions for computing control variables can be derived according to the synergetic control algorithm and the mathematical model of a grid-connected PV system. Two control strategies are used in normal operation and during LVRT. The parameters  $T_1$  and  $T_2$  of the two synergetic controllers are the same. The parameters of the synergetic controllers are easy to determine, and results indicate that the synergetic controllers are robust. The grid-connected PV system can obtain a maximum power point and inject the power into the grid when the radiation and temperature change rapidly. The DC link voltage and AC currents are limited, and the DC-AC VSC converters are not damaged during LVRT. The PV system can run with  $I_q = -1$  pu continuously and supply reactive power to the grid when the grid voltage decreases to 0.05 pu.

Synergetic control has good dynamic characteristics in normal operation and during LVRT and is the alternative solution for grid-connected PV systems.

## Conflicts of Interest

The authors declare that there is no conflict of interests regarding the publication of this paper.

## Acknowledgments

This work was financially supported by the National Natural Science Foundation of China (51177074, 51407095) and the Jiangsu Province Natural Science Foundation (BK20151548).

## References

- [1] A. Rosa, *Fundamentals of Renewable Energy Processes*, Academic Press, Boston, MA, USA, 2012.
- [2] REN21, *Renewables 2016 Global Status Report*, REN21 Secretariat, Paris, France, 2016, [http://www.ren21.net/wp-content/uploads/2016/06/GSR\\_2016\\_Full\\_Report\\_REN21.pdf](http://www.ren21.net/wp-content/uploads/2016/06/GSR_2016_Full_Report_REN21.pdf).
- [3] N. Femia, G. Petrone, G. Spagnuolo, and M. Vitelli, "Optimization of perturb and observe maximum power point tracking method," *IEEE Transactions on Power Electronics*, vol. 20, no. 4, pp. 963–973, 2005.
- [4] K. H. Hussein, I. Muta, T. Hoshino, and M. Osakada, "Maximum photovoltaic power tracking: an algorithm for rapidly changing atmospheric conditions," *IEE Proceedings-Generation, Transmission and Distribution*, vol. 142, no. 1, pp. 59–64, 1995.
- [5] P. Q. Dzung, L. D. Khoa, H. H. Lee, L. M. Phuong, and N. T. D. Vu, "The new MPPT algorithm using ANN based PV," in *Proceedings of the International Forum on Strategic Technology*, pp. 402–407, Ulsan, South Korea, 13–15 October 2010.
- [6] N. Zakzouk, M. Elsharty, A. Abdelsalam, A. Helal, and B. Williams, "Improved performance low-cost incremental conductance PV MPPT technique," *IET Renewable Power Generation*, vol. 10, no. 4, pp. 561–574, 2016.
- [7] K. Sundareswaran, V. Vigneshkumar, P. Sankar, S. Simon, P. Nayak, and S. Palani, "Development of an improved P&O algorithm assisted through a colony of foraging ants for MPPT in PV system," *IEEE Transactions on Industrial Informatics*, vol. 12, no. 1, pp. 187–200, 2016.
- [8] S. Mohanty, B. Subudhi, and P. Ray, "A new MPPT design using grey wolf optimization technique for photovoltaic system under partial shading conditions," *IEEE Transactions on Sustainable Energy*, vol. 7, no. 1, pp. 181–188, 2016.
- [9] MathWorks, *Detailed Model of a 100-kW Grid-Connected PV Array*, MathWorks, Natick, MA 01760-2098, USA, 2015, [http://www.mathworks.com/examples/simpower/mw/sps\\_product-power\\_PVarray\\_grid\\_det-detailed-model-of-a-100-kw-grid-connected-pv-array](http://www.mathworks.com/examples/simpower/mw/sps_product-power_PVarray_grid_det-detailed-model-of-a-100-kw-grid-connected-pv-array).
- [10] N. Kumar, T. Saha, and J. Dey, "Sliding-mode control of PWM dual inverter-based grid-connected PV system: modeling and performance analysis," *IEEE Journal of Emerging Selected Topics in Power Electronics*, vol. 4, no. 2, pp. 435–444, 2016.
- [11] F. Lin, K. Lu, and T. Ke, "Probabilistic wavelet fuzzy neural network based reactive power control for grid-connected three-phase PV system during grid faults," *Renewable Energy*, vol. 92, pp. 437–449, 2016.
- [12] J. Sosa, M. Castilla, J. Miret, J. Matas, and Y. Al-Turki, "Control strategy to maximize the power capability of PV three-phase inverters during voltage sags," *IEEE Transactions on Power Electronics*, vol. 31, no. 4, pp. 3314–3323, 2016.

- [13] H. M. Hasanien, "An adaptive control strategy for low voltage ride through capability enhancement of grid-connected photovoltaic power plants," *IEEE Transactions on Power Apparatus and Systems*, vol. 31, no. 4, pp. 3230–3237, 2016.
- [14] E. Santi, A. Monti, D. Li, K. Proddatur, and R. Dougal, "Synergetic control for dc-dc boost converter: implementation options," *IEEE Transactions on Industry Applications*, vol. 39, no. 6, pp. 1803–1813, 2003.
- [15] Z. Jiang and R. Dougal, "Synergetic control of power converters for pulse current charging of advanced batteries from a fuel cell power source," *IEEE Transactions on Power Electronics*, vol. 19, no. 4, pp. 1140–1150, 2004.
- [16] MathWorks, *abc to dq0, dq0 to abc*, MathWorks, Natick, MA 01760-2098, USA, 2015, <http://www.mathworks.com/help/physmod/sps/powersys/ref/abctodq0dq0toabc.html>.
- [17] *Grid Code High and Extra High Voltage*, E.ON Netz GmbH, Bayreuth, Germany, 2006.
- [18] BDEW, *Technical Guideline: Generating Plants Connected to the Medium-Voltage Network*, BDEW, Berlin, Germany, 2008, <http://www.bdew.de>.
- [19] DEIF, *LVRT Capability-Test Results*, <http://www.deifwindpower.com/wind-turbine-solutions/control-systems/lvrt-test-results>.
- [20] H. Chong, R. Li, and B. Jim, "Unbalanced-grid-fault ride-through control for a wind turbine inverter," *IEEE Transactions on Industry Applications*, vol. 44, no. 3, pp. 845–856, 2008.

## Research Article

# Analysis on Photovoltaic Energy-Assisted Drying of Green Peas

**Onur Taşkın, Nazmi İzli, and Ali Vardar**

*Department of Biosystems Engineering, Faculty of Agriculture, Uludag University, 16059 Bursa, Turkey*

Correspondence should be addressed to Onur Taşkın; [onurtaskins@gmail.com](mailto:onurtaskins@gmail.com)

Received 18 August 2016; Revised 23 October 2016; Accepted 10 November 2016

Academic Editor: Ke Ma

Copyright © 2016 Onur Taşkın et al. This is an open access article distributed under the Creative Commons Attribution License, which permits unrestricted use, distribution, and reproduction in any medium, provided the original work is properly cited.

A photovoltaic energy-assisted industrial dryer has been analyzed. The dryer has been tested in various weather and working conditions with 3 kg of green peas from 75.6% initial moisture content to 20% final moisture content (w.b.). The effect of various drying air temperatures at three levels (40, 50, and 60°C) and two distinct air velocities (3 m/s and 4 m/s) was examined. Drying performance was assessed with regard to criteria including drying kinetics, specific and total energy consumption, and color and rehydration ratio. The results have proved that total drying duration reduces as air velocity rate and drying air temperature raise. Relying upon the drying durations, the generation performances of photovoltaic panels were between 5.261 and 3.953 W. On the other part, energy consumptions of dryer were between 37.417 and 28.111 W. The best specific energy consumption was detected in 50°C at 3 m/s for 600 minutes with 7.616 kWh/kg. All drying conditions caused darkening as color parameters. Rehydration assays have showed that rehydrated green peas attained higher capacity with raised air temperature and air velocity.

## 1. Introduction

Green peas (*Pisum sativum*) are one of the most common and popular legumes in the world [1]. According to statistics prepared by Food and Agriculture Organization, dry green pea production in 2014 was nearly 11.3 million tons worldwide [2]. It has been extensively used in the human diet for a long time since it is an excellent source of protein, vitamins, minerals, and other nutrients and also high in fiber and low in fat and finally contains no cholesterol as well [3]. Because of its high moisture content, drying is an alternative method to preserve pea. Dried peas have become popular as they provide the advantage of longer shelf life, palatability, and convenience during its transportation and handling [4]. Also, drying of peas enables effective and practical preservation so as to minimize the losses after harvest. Like other legumes, dried peas can be used in meals or soups. Similarly, it is used in some traditional meals in UK and North America [5]. They are generally dried in thin layer by using hot air for industrial purposes [1].

Since ancient times, sun drying is one of the simple and well-known techniques of lessening the moisture content of the agricultural products. With respect to its negligible cost and energy need, it is advantageous. Conversely, this process

is disadvantageous in terms of its slow speed and labor requirement. During drying, products can be polluted by dirt, dust, animals, insects, and microbial contamination and also this method has no protection against environmental conditions such as rain or storm as well [5]. As a result, loss in food quality in the dried products may have negative effects on their economic worth and trade potential. To prevent decline in quality of materials, various types of drying methods have been built. Conventional dryers among them are proved to be uneconomic because of their high energy cost [6]. Consuming minimum energy at maximum drying efficiency is aimed at industrial drying. For this reason, solar drying is a suitable choice which both provides low cost drying and decreases pollution of fossil fuel usage. Solar drying technology is simple and easy to adopt to domestic sector [7]. So as to benefit from free and renewable energy resources, in recent years, there have been several dryer attempts to preserve agricultural products [8].

About photovoltaic (PV) assisted dryers, Adelajaa et al. [9] demonstrated the integration of a suction fan which is powered by a solar PV module. An experiment was conducted in June on vegetable (*Hydrophyllum*). The designed dryer has drying chamber temperature of 58°C which is in conformance with the optimum temperature for drying

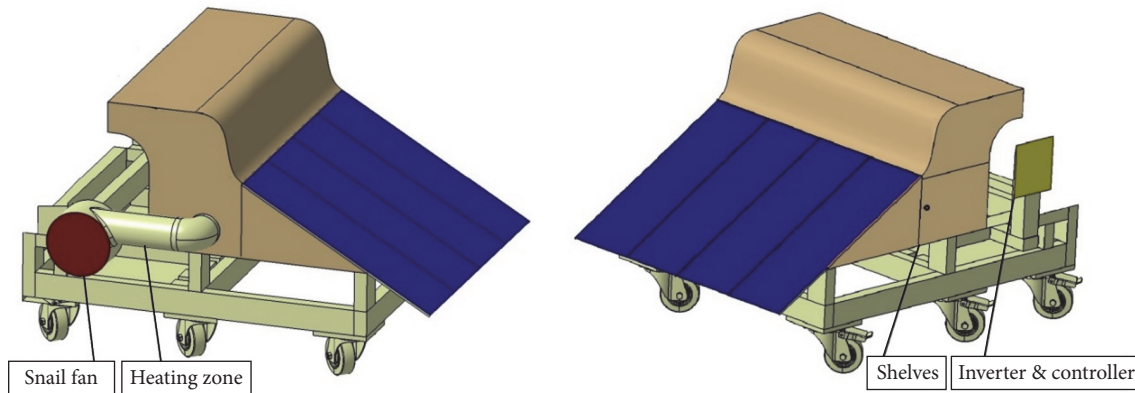


FIGURE 1: Technical drawing.

vegetables and its collector efficiency is 83.2%. Nwosu et al. [10] depicted the design and experimental performance evaluation of a photovoltaic-powered solar drying system. The experimental outcomes indicate that, even at unfavorable weather conditions, the unit can produce cassava in good quality. Aktaş et al. [11] produced and analyzed the solar energy dryer that has 10 kg tomato capacity. Dryer has been used at various conditions. Required electricity and heat energy were provided by solar energy totally. Tomato slices were dried at drying air temperatures of 40°C, 45°C, and 50°C, respectively, and average 0.2 m/s air velocity for 8.5, 7, and 6 hours, respectively. According to the results of the experiment average solar collector efficiency was calculated as 49.33%. Ceylan et al. [6] also designed and produced a new type of solar dryer. In this experimental drying process tomatoes were used as well. The photovoltaic cells were used to run the fan and charge the batteries during the day as well. These charged batteries ran the halogen lamps during the night, and these halogen lamps were used to heat the drying-air-assisted photovoltaic cells. The solar dryer efficiency will increase in the summer season since solar radiation increases in this period. The dryer is called green solar dryer as the required power was supplied by using PV cells. Seveda [12] devised a photovoltaic-powered-forced convection solar dryer and assessed it in the conditions of NEH region of India. Dryer had a 6 kg capacity of chilies per batch. Average air temperature reached in the solar dryer was about 40°C, which was higher than the ambient temperature. Chili drying process in a PV powered-forced convection solar dryer decreases the moisture content from nearly 80.2% (wet basis) to the final moisture content of nearly 10.0% in 32 hours.

In this research, the main objective is to assess the performance of the designed and manufactured PV-assisted dryer. Thin-layer green peas were used in the drying process in this experiment with the effects of various air temperature and air velocity on the drying time, color, rehydration ratio, and specific and total energy consumption.

## 2. Materials and Methods

Green peas (*Pisum sativum*), which were used in the drying experiments, were grown in the region of Yenişehir, Bursa,

Turkey. The product was harvested on June 29, 2016, and then was stored at  $4.0 \pm 0.1^\circ\text{C}$  to inhibit moisture loss. Before the drying experiments were conducted the harvest was carried out once and the same product was used during the all drying experiments. Uniform kernels which have average radius of  $10.9 \pm 0.4$  mm were used. Initial moisture contents of the samples were specified by oven drying (ED 115 Binder, Tuttlingen, Germany) at 105°C for 24 hours. Based on this initial moisture content analysis, moisture content was found to be 75.6%, wet basis.

**2.1. Experimental Setup.** Developed dryer experiments had taken place under outdoor meteorological conditions of Field Laboratory of Department of Biosystems Engineering, Faculty of Agriculture, Bursa, Turkey ( $40^\circ 13' \text{N}$ ,  $28^\circ 51' \text{E}$ ). Technical drawing view of the dryer is exhibited in Figure 1.

This device contains 1kW total capacity polycrystalline solar panel module (SFP250, Solarfield, Turkey) with horizontal angle of  $30^\circ$  always facing south, 1.1 kW snail fan (1.5 1500S, MTA, Turkey) that possesses digital potentiometer, 8 kW electric resistance heater zone, proportional integral derivative (PID) control processor with a PT100 thermocouple (Esm 7730, Emko, Turkey), twelve batteries (DC12V 100A) which are connected in series to get 48 V power source (SPG100/12, SB, China), inverter and controller, digital electric meters, and drying chamber that has four shelves (198 cm–58 cm). There was an 8 cm space between two trays. Only one tray was used in these experiments.

**2.2. Test Procedure.** In this research, the performance of PV-assisted dryer was examined. The design had been performed by taking local conditions into account. The experiments were carried out between the dates July 01 and July 14, 2016, between the hours 10:00 am and 8:00 pm with duple replicate. The dryer was placed away from any shadow throughout the experiment. For thin-layer drying, samples were put on wire mesh trays.

In order to understand the effect of environmental conditions, average environmental data measurements in July were recorded by the datalogger (Cr1000, Campbell Scientific, USA) for 12 days. The dataset is composed of 1 min averaged

measurements of global horizontal irradiance (CM11 pyranometer, Kipp&Zonen, Netherlands), direct normal irradiance (CHP1 pyrhemometer, Kipp&Zonen, Netherlands) with an installed on solar tracker, sunshine duration (CSD 3 Sensor, Kipp&Zonen, Netherlands), ambient temperature (41342, Young, USA), and ambient humidity (41003, Young, USA). The station is placed just besides the dryer.

### 2.3. Analysis Procedure

**2.3.1. Drying Kinetics.** By visually inspecting, damaged, immature, and dry pods were excluded manually. In addition the pea pods were shelled by hand [4]. After separation of green peas, it dried in dryer with air temperatures of 50, 60, and 70°C [13], respectively at 3 m/s and 4 m/s air velocities [14, 15]. Single layers of drying were performed on a mesh tray which was containing fresh green peas of 3 kg. Then digital grain moisture tester gauged the moisture content (Mini GAC plus, Dickey-John, USA) [16]. This procedure was repeated until moisture content was decreased to 20% (w.b.) [17]. After drying process, the product was cooled for 10 minutes and then it was kept in air glass jars for one week by the time color and rehydration measurements were carried out [18].

**2.3.2. Specific and Total Energy Consumption.** Specific energy consumption was defined as the energy required to remove a unit mass of water in drying process [19]. This specific energy calculation was expressed as kWh/kg of the moisture removed. On the other hand, for air heating and blower running total energy consumption of dryer was calculated by using a digital electric counter (AEL MF 07, Kohler, Turkey) [20]. Moreover energy production realized by PV panels has been measured (Bk325, GT Power RC, China) during the drying period and it was excluded from total consumption.

**2.3.3. Color.** A colorimeter has determined the color of initial and dried samples (EZ 4500L, Hunter Lab, USA). Commission Internationale d'Eclairage was embraced with the three-dimensional color space and construed as follows:  $L^*$  is the brightness value which ranges from no reflection for black ( $L = 0$ ) value to perfect diffuse reflection for white ( $L = 100$ ) value.  $a^*$  value is the redness which ranges from negative values that represent green to positive values that represent red.  $b^*$  value is the yellowness which ranges from negative values that stand for blue and positive values that stand for yellow [21]. Before the color measurement operations, calibration of the device was completed by utilizing a standard white plate ( $x = 82.43$ ,  $y = 84.55$ , and  $z = 99.39$ ) and also utilizing a standard black plate ( $x = 0$ ,  $y = 0$ , and  $z = 0$ ). In the course of the measurements, green peas were superposed in order to cover the surface of the black cylindrical box totally [22].

**2.3.4. Rehydration.** Rehydration experiments were conducted with dried samples of 10 g which were put into a cloth and placed in a beaker in which there is 250 mL distilled water. The beakers were retained at room temperature of

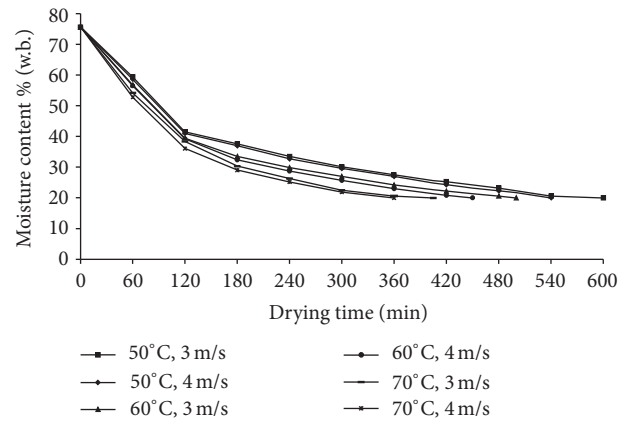


FIGURE 2: Air temperature and air velocity influence on green peas drying.

nearly 20°C, for 14 hours time. Afterwards, these samples were taken out from the beaker and drained over a mesh so as to remove the superficial water, and then they were weighed by digital balance (PS 4500, Radwag, Poland). Rehydration capacity was identified as the ratio of the total weight of the sample to the dry weight of it after rehydration in grams [23].

**2.4. Statistical Analysis.** Obtained results were processed by using MS-Excel software. After examination of the each drying method, so as to assess any significant difference between the color and the rehydration capacity a one-way analysis of variance was used. All calculations were done by means of the JMP software (version 7.0, NC, USA). Unless otherwise specified, differences were regarded as significant at  $P < 0.05$  value.

## 3. Results and Discussion

For reduction of moisture content, effects of different drying air temperatures and air velocities are shown in Figure 2. Obtained results indicated that drying of green peas was performed at air temperatures of 50, 60, and 70°C at a constant drying air velocity of 3 m/s and took about 600, 500, and 405 minutes, respectively. In addition to this, the drying of green peas continued about 540, 450, and 360 minutes in 50, 60, and 70°C at a constant drying air velocity of 4 m/s, respectively. The drying duration was reduced by 1.48 times in proportion to the drying process which was realized in 50 to 70°C at 3 m/s air velocity. Likewise, drying duration was surged about 1.50 times, if the drying temperature reduced from 70 to 50°C at 4 m/s air velocity. As a result, the drying duration is expected to reduce the moisture which was at the highest level in 50°C at 3 m/s air velocity and at the lowest level in 70°C at 4 m/s air velocity and consequently the average total drying duration decreased about 40% times. As it can be seen, higher drying temperatures and air velocities will improve the kinetic energy of water molecules, and ultimately it stimulates water evaporation rate. For this reason, drying duration reduced with increased air temperature and velocity. So these results are in line with the previous researches.

Results about the increase in drying air temperatures are similar to those founded by Taechapairoj et al. [24] for paddy, Doymaz [25] for green bean, Rattanamechaiskul et al. [26] for purple rice, and Doymaz [27] for red kidney bean seeds. In other respects, it has been seen that the increase in air velocity has significantly reduced the drying duration at other researches such as Afzal et al. [28] for barley, Darvishi et al. [29] for soybean, and Chielle et al. [30] for papaya seeds.

The environmental conditions are depicted on Figure 3. Experiments were conducted in clear sunshine sky conditions and started at 10:00 am till the moisture content was reduced to 20%. According to the average daily results gathered from the research shown in Figures 3(a)–3(f), it can be assumed that the ratio of global solar radiation intensity during the experiments was around 667.20 W/m<sup>2</sup> for 50° and 3 m/s, 723.25 W/m<sup>2</sup> for 50° and 4 m/s, 741.74 W/m<sup>2</sup> for 60° and 3 m/s, 798.30 W/m<sup>2</sup> for 60° and 4 m/s, 843.83 W/m<sup>2</sup> for 70° and 3 m/s, and 874.25 W/m<sup>2</sup> for 70° and 4 m/s; and the ratio of direct solar radiation intensity during the experiments was approximately 750.44 W/m<sup>2</sup> for 50° and 3 m/s, 771.48 W/m<sup>2</sup> for 50° and 4 m/s, 782.14 W/m<sup>2</sup> for 60° and 3 m/s, 815.55 W/m<sup>2</sup> for 60° and 4 m/s, 824.93 W/m<sup>2</sup> for 70° and 3 m/s, and 843.10 W/m<sup>2</sup> for 70° and 4 m/s; and the ambient temperature during the experiments is approximately 29.70°C for 50° and 3 m/s, 29.63°C for 50° and 4 m/s, 30.93°C for 60° and 3 m/s, 30.05°C for 60° and 4 m/s, 30.58°C for 70° and 3 m/s, and 30.32°C for 70° and 4 m/s; and the relative humidity during the experiments is approximately 46.87% for 50° and 3 m/s, 47.94% for 50° and 4 m/s, 43.54% for 60° and 3 m/s, 42.64% for 60° and 4 m/s, 39.25% for 70° and 3 m/s, and 35.93% for 70° and 4 m/s. Within this framework, it was concluded that drying time and environmental conditions have influenced the total amount of electricity produced from solar panel.

For various drying treatments, energy consumption variation (electric resistances and blower) and energy production from PV are depicted in Figure 4. When comparison of the different drying processes with regard to energy consumption values was conducted, it was noticed that temperature rise of air that has relative humidity is significant for energy consumption of electric resistances. Additionally, if the heating unit works with low air temperature, the dryer requires less energy. Among all drying methods, the lowest and highest energy consumptions were seen at 50°C at 3 m/s and 70°C at 4 m/s, respectively. During the drying durations, when the PV panels produced energy, the average total energy consumption decreased about 10.56% to 18.71%.

The specific energy increased with increased air velocity (at constant temperature) as it can be seen at Figure 5. Data results display that, for green peas, the highest value of the specific energy was 11.154 kW h/kg in 70°C at 4 m/s and the lowest value of the specific energy was attained in 50°C at 3 m/s to be 7.616 kW h/kg. So it means that choosing the proper temperature and air velocity leads to reduced specific energy consumption. In the literature similar results can be found such as Adabi et al. [31] who dried squash seeds in semifluidized and fluidized-bed dryers. Obtained results indicated that increase in air velocity leads to apparent

increase in the value of specific energy consumption. Chayjan et al. [32] examined the specific energy consumption of several drying methods for black mulberry. From that research, it was understood that drying at higher air velocities ends in more energy consumption.

Summary of the average color values ( $L^*$ ,  $a^*$ , and  $b^*$ ) of fresh and green peas which undergo various drying processes are seen at Table 1. While the brightness values ( $L^*$ ) of fresh samples were 44.11, the greenness/redness ( $a^*$ ) values were  $-5.49$  and the yellowness/blueness ( $b^*$ ) values were 31.82. These results indicate that all of the drying experiments have affected the color changes as expected.  $L^*$  value which is most close to those of fresh green peas was obtained in 70°C at 4 m/s air velocity, whereas the most remote  $L^*$  value was obtained in 50°C at 3 m/s air velocity. Furthermore,  $L^*$  value diminishes on account of the long drying duration. As compared to fresh green peas, it was found that  $a^*$  and  $b^*$  values raised during drying significantly. While the air temperature and air velocity increased, the final  $a^*$  values ranged from  $-0.15$  to  $-2.51$ . For this reason, green peas samples lost their greenness. It can be seen from Table 1 that  $b^*$  value raised with decreased drying duration. It was mentioned that  $b^*$  values of dried green peas reduced from 31.82 to 28.08 and 24.01 during various air temperatures and air velocities. Through the instrument of the statistical analysis, it was confirmed that both increase of the air temperature and increase of the air velocity have influenced the color values ( $P < 0.05$ ) significantly. Similar color deviations were emphasized by some authors. Ben Haj Said et al. [33] asserted that the negative  $a^*$  value of *Allium roseum* leaves increases significantly, after the application of thin-layer convective drying at three temperatures (40, 50, and 60°C) and two air velocities (1.0 and 1.5 m/s). Demiray and Tulek [34] examined the influence of temperature on color change kinetics of carrot slices. Finally, the color values were influenced by hot air drying; for instance,  $L^*$  values decreased from 57.87 to 49.32 at 65°C. Additionally, Aral and Beşe [35] applied the color analysis to thin-layer drying of hawthorn fruit (*Crataegus* spp.) at air temperatures of 50, 60, and 70°C and air velocities of 0.5, 0.9, and 1.3 m/s in a convective dryer. They discovered that decrease of the drying air temperature and air velocity which led to longer drying time and decrease of  $b^*$  value can be regarded as the yellowness that fruit loses.

Rehydration ratio characteristics of green peas which were dried at different temperatures and air velocities are depicted in Table 1. General results were observed as follows. The maximum rehydration capacity, which was 2.35, was obtained in 70°C at 4 m/s. In the same way, the minimum rehydration capacity, which was 2.26, was obtained in 50°C at 3 m/s. Taking the individual effects into account, the average rehydration capacity of samples raises with the increase of air temperature and velocity. In addition, the statistical analysis indicated that there was no significant difference between the rehydration capacity in 50°C at 3 m/s and the rehydration capacity in 70°C at 4 m/s, at 5% probability level only. A behavior like this was reported in a few researches conducted about hot air drying of pumpkin slices [36], nata de coco [37], and *Rosa rubiginosa* fruits [38].

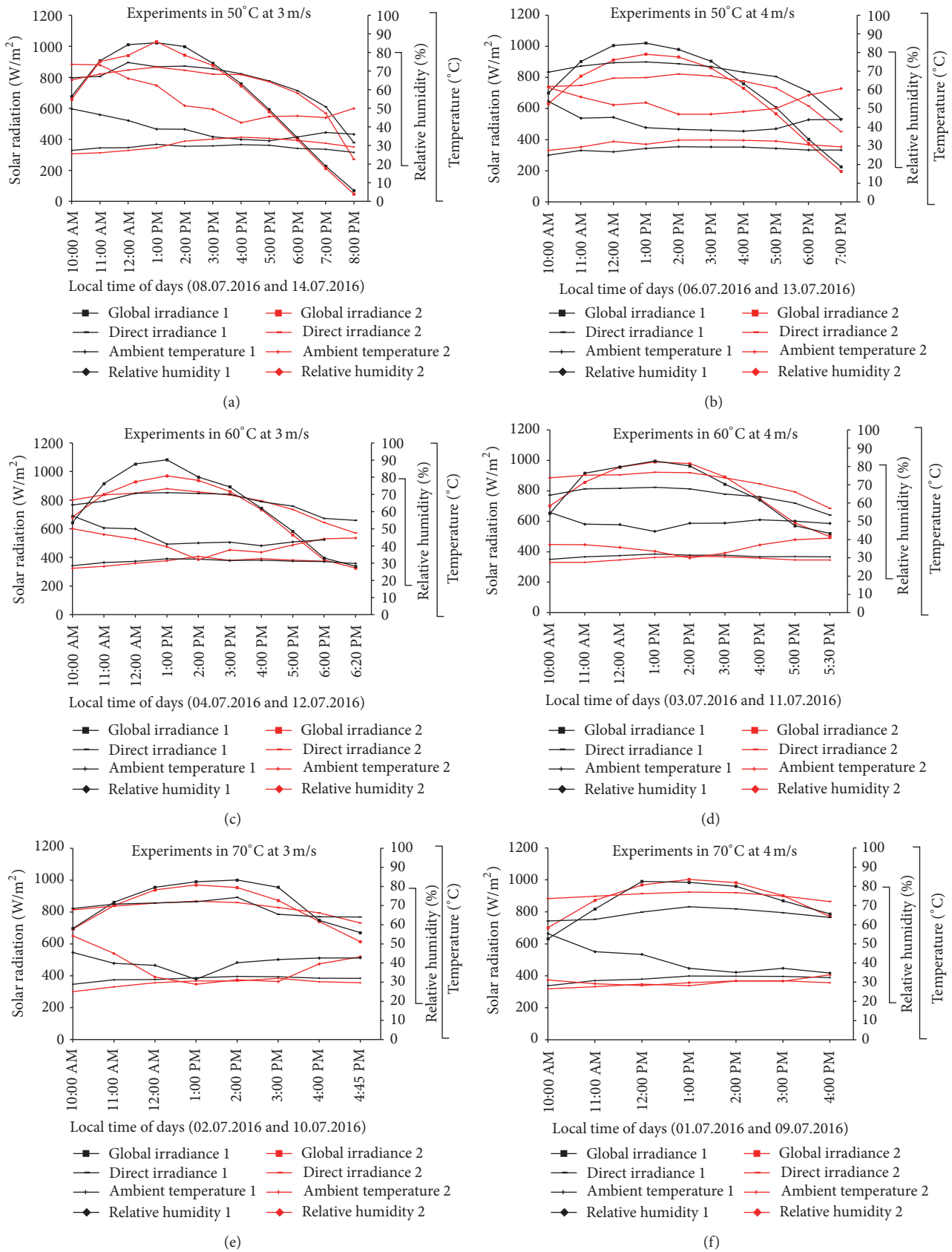


FIGURE 3: Climatic data of experimental dates (black and red lines are symbolize the 1st and 2nd dates, resp.).

TABLE 1: Hunter  $L^*a^*b^*$  values and rehydration ratio of green peas.

		$L^*$	$a^*$	$b^*$	Rehydration capacity
Fresh		$44.11 \pm 0.38^a$	$-5.69 \pm 0.02^c$	$31.82 \pm 0.23^a$	—
3 m/s	50°C	$34.64 \pm 1.10^f$	$-2.51 \pm 0.57^d$	$24.01 \pm 0.71^f$	$2.26 \pm 0.01^a$
	60°C	$36.96 \pm 0.93^e$	$-2.15 \pm 0.03^c$	$26.49 \pm 0.14^d$	$2.27 \pm 0.01^a$
	70°C	$39.55 \pm 0.20^d$	$-0.46 \pm 0.12^a$	$27.36 \pm 0.53^{bc}$	$2.32 \pm 0.09^a$
4 m/s	50°C	$40.93 \pm 0.56^c$	$-2.33 \pm 0.25^{cd}$	$25.67 \pm 0.69^e$	$2.26 \pm 0.01^a$
	60°C	$41.55 \pm 0.72^{bc}$	$-1.32 \pm 0.23^b$	$26.83 \pm 0.91^{cd}$	$2.28 \pm 0.13^a$
	70°C	$42.39 \pm 0.75^b$	$-0.15 \pm 0.10^a$	$28.08 \pm 0.59^b$	$2.35 \pm 0.05^a$

<sup>a-f</sup>Superscripts with different alphabets in the same column differ significantly ( $P < 0.05$ ).

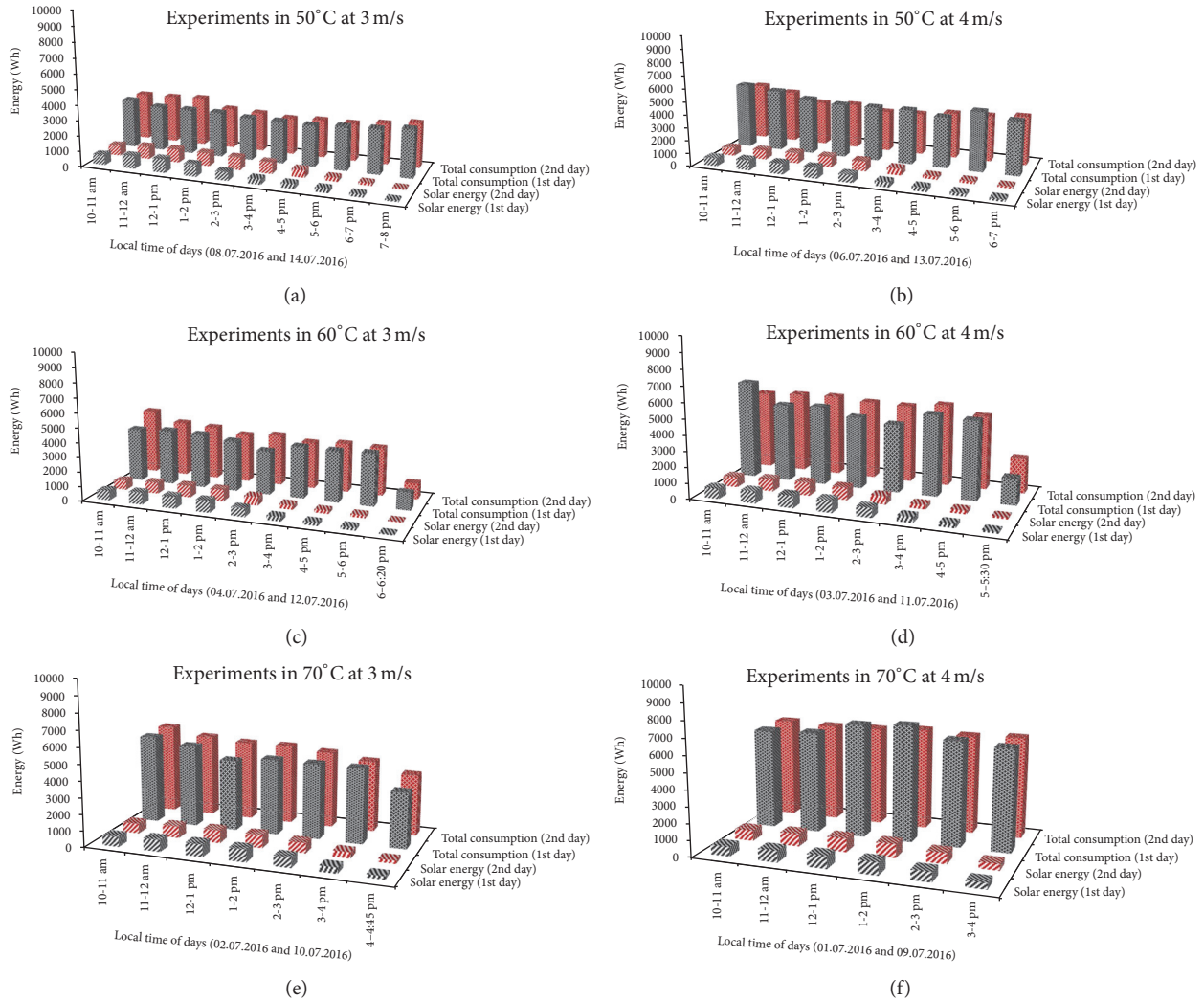


FIGURE 4: Energy consumption and energy production.

## 4. Conclusions

The industrial drying of green peas with PV energy assistance has been investigated in six different applications here. Dried green peas were analyzed with regard to drying time, color, rehydration, specific energy, and total energy consuming. The obtained results displayed that the increase in the drying air temperature (50°C to 70°C) and air velocity (3 m/s to

4 m/s) has resulted in decrease in drying duration. Further, experimental results pointed that the specific energy ranges from 7.561 kW h/kg to 11.154 kW h/kg. Ultimately, the color deviation has been exposed in all treatments and also the statistical analysis about rehydration ratio of dried green peas demonstrates that there are no significant differences about the operating conditions such as air temperature and air velocity. Industrial drying with the PV energy assistance is

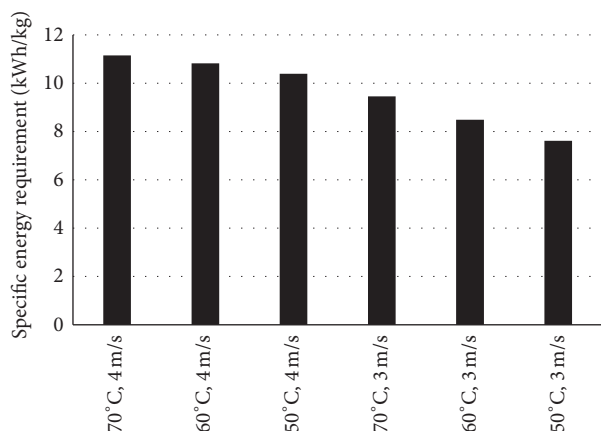


FIGURE 5: Specific energy required for drying of green peas.

a beneficial application for widespread use in agriculture in order to reduce total energy consumption.

### Competing Interests

The authors declare that there is no conflict of interests regarding the publication of this paper.

### Acknowledgments

The authors are grateful to the Research Project Unit of Uludag University for providing the financial support (Project no. OUAP(Z)-2014/20).

### References

- [1] M. Zielinska, P. Zapotoczny, O. Alves-Filho, T. M. Eikevik, and W. Blaszcak, "A multi-stage combined heat pump and microwave vacuum drying of green peas," *Journal of Food Engineering*, vol. 115, no. 3, pp. 347–356, 2013.
- [2] FAO, "Food and Agricultural Organization Statistica Database 2016," <http://faostat3.fao.org/download/Q/QC/E>.
- [3] O. Ismail, B. Beyribey, and İ. Doymaz, "Investigation of dehydration and rehydration kinetics of peas subjected to open-air sun drying," *Latin American Applied Research*, vol. 44, pp. 209–216, 2014.
- [4] İ. Doymaz and F. Kocayigit, "Drying and rehydration behaviors of convection drying of green peas," *Drying Technology*, vol. 29, no. 11, pp. 1273–1282, 2011.
- [5] S. Sahin, G. Sumnu, and F. Tunaboyu, "Usage of solar-assisted spouted bed drier in drying of pea," *Food and Bioprocess Processing*, vol. 91, no. 3, pp. 271–278, 2013.
- [6] I. Ceylan, M. Kaya, A. E. Gürel, and A. Ergun, "Energy analysis of a new design of a photovoltaic cell-assisted solar dryer," *Drying Technology*, vol. 31, no. 9, pp. 1077–1082, 2013.
- [7] A. Mohajer, O. Nematollahi, M. M. Joybari, S. A. Hashemi, and M. R. Assari, "Experimental investigation of a hybrid solar drier and water heater system," *Energy Conversion and Management*, vol. 76, pp. 935–944, 2013.
- [8] D. B. Jadhav, G. L. Visavale, N. Sutar, U. S. Annapure, and B. N. Thorat, "Studies on Solar cabinet drying of green peas (*Pisum sativum*)," *Drying Technology*, vol. 28, no. 5, pp. 600–607, 2010.
- [9] A. O. Adelajaa, B. Y. Ogunmolab, and P. O. Akoladec, "Development of a photovoltaic powered forced convection solar dryer," *Advanced Materials Research*, vol. 62–64, pp. 543–548, 2009.
- [10] P. N. Nwosu, V. K. Sharma, O. U. Oparaku et al., "Experimental investigation of a photovoltaic-powered solar cassava dryer," *Drying Technology*, vol. 30, no. 4, pp. 398–403, 2012.
- [11] M. Aktaş, S. Şevik, H. Doğan, and M. Öztürk, "Drying of tomato in a photovoltaic and thermal solar-powered continuous dryer," *Journal of Agricultural Sciences*, vol. 18, pp. 287–298, 2012.
- [12] M. S. Seveda, "Design of a photovoltaic powered forced convection solar dryer in NEH region of India," *International Journal of Renewable Energy Research*, vol. 3, no. 4, pp. 906–912, 2013.
- [13] J. O. Ojediran and A. O. Raji, "Thin-layer drying characteristics of castor (*Ricinus communis*) seeds," *Journal of Food Processing and Preservation*, vol. 35, no. 5, pp. 647–655, 2011.
- [14] G. Clemente, N. Sanjuán, J. A. Cárcel, and A. Mulet, "Influence of temperature, air velocity, and ultrasound application on drying kinetics of," *Drying Technology*, vol. 32, no. 1, pp. 68–76, 2014.
- [15] S. Soponronnarit, A. Pongtornkulpanich, and S. Prachayawarakorn, "Drying characteristics of corn in fluidized bed dryer," *Drying Technology*, vol. 15, no. 5, pp. 1603–1615, 1997.
- [16] W. Jittanit, N. Saeteaw, and A. Charoenchaisri, "Industrial paddy drying and energy saving options," *Journal of Stored Products Research*, vol. 46, no. 4, pp. 209–213, 2010.
- [17] M. Barzegar, D. Zare, and R. L. Stroshine, "An integrated energy and quality approach to optimization of green peas drying in a hot air infrared-assisted vibratory bed dryer," *Journal of Food Engineering*, vol. 166, pp. 302–315, 2015.
- [18] İ. Doymaz and M. Pala, "The thin-layer drying characteristics of corn," *Journal of Food Engineering*, vol. 60, no. 2, pp. 125–130, 2003.
- [19] I. Das, S. K. Das, and S. Bal, "Specific energy and quality aspects of infrared (IR) dried parboiled rice," *Journal of Food Engineering*, vol. 62, no. 1, pp. 9–14, 2004.
- [20] I. Alibas, "Energy consumption and colour characteristics of nettle leaves during microwave, vacuum and convective drying," *Biosystems Engineering*, vol. 96, no. 4, pp. 495–502, 2007.
- [21] A. K. S. Chauhan and A. K. Srivastava, "Optimizing drying conditions for vacuum-assisted microwave drying of green peas (*Pisum sativum* L.)," *Drying Technology*, vol. 27, no. 6, pp. 761–769, 2009.
- [22] L. A. Ramallo and R. H. Mascheroni, "Quality evaluation of pineapple fruit during drying process," *Food and Bioprocess Processing*, vol. 90, no. 2, pp. 275–283, 2012.
- [23] F. Tunaboyu, *Usage of solar-spouted bed drier in the drying of parboiled wheat, corn and pea [M.S. thesis]*, Natural and Applied Sciences of Middle East Technical University, Ankara, Turkey, 2011.
- [24] C. Taechapairoj, I. Dhuchakallaya, S. Soponronnarit, S. Wetchacama, and S. Prachayawarakorn, "Superheated steam fluidised bed paddy drying," *Journal of Food Engineering*, vol. 58, no. 1, pp. 67–73, 2003.
- [25] I. Doymaz, "Drying behaviour of green beans," *Journal of Food Engineering*, vol. 69, no. 2, pp. 161–165, 2005.
- [26] C. Rattanamechaiskul, N. Junka, C. Wongs-Aree, S. Prachayawarakorn, and S. Soponronnarit, "Influence of hot air fluidized bed drying on quality changes of purple rice," *Drying Technology*, vol. 34, no. 12, pp. 1462–1470, 2016.

- [27] İ. Doymaz, "Hot-air drying and rehydration characteristics of red kidney bean seeds," *Chemical Engineering Communications*, vol. 203, no. 5, pp. 599–608, 2016.
- [28] T. M. Afzal, T. Abe, and Y. Hikida, "Energy and quality aspects during combined FIR-convection drying of barley," *Journal of Food Engineering*, vol. 42, no. 4, pp. 177–182, 1999.
- [29] H. Darvishi, M. H. Khoshtaghaza, and S. Minaei, "Effects of fluidized bed drying on the quality of soybean kernels," *Journal of the Saudi Society of Agricultural Sciences*, vol. 14, no. 2, pp. 134–139, 2015.
- [30] D. P. Chielle, D. A. Bertuol, L. Meili, E. H. Tanabe, and G. L. Dotto, "Convective drying of papaya seeds (*Carica papaya* L.) and optimization of oil extraction," *Industrial Crops and Products*, vol. 85, pp. 221–228, 2016.
- [31] M. E. Adabi, A. Motevali, A. M. Nikbakht, and M. H. Khoshtaghaza, "Investigation of some pretreatments on energy and specific energy consumption drying of black mulberry," *Chemical Industry and Chemical Engineering Quarterly*, vol. 19, no. 1, pp. 89–105, 2013.
- [32] R. A. Chayjan, K. Salari, Q. Abedi, and A. A. Sabziparvar, "Modeling moisture diffusivity, activation energy and specific energy consumption of squash seeds in a semi fluidized and fluidized bed drying," *Journal of Food Science and Technology*, vol. 50, no. 4, pp. 667–677, 2013.
- [33] L. Ben Haj Said, H. Najjaa, M. Neffati, and S. Bellagha, "Color, phenolic and antioxidant characteristic changes of allium roseum leaves during drying," *Journal of Food Quality*, vol. 36, no. 6, pp. 403–410, 2013.
- [34] E. Demiray and Y. Tulek, "Color degradation kinetics of carrot (*Daucus carota* L.) slices during hot air drying," *Journal of Food Processing and Preservation*, vol. 39, no. 6, pp. 800–805, 2015.
- [35] S. Aral and A. V. Beşe, "Convective drying of hawthorn fruit (*Crataegus* spp.): effect of experimental parameters on drying kinetics, color, shrinkage, and rehydration capacity," *Food Chemistry*, vol. 210, pp. 577–584, 2016.
- [36] L. Seremet, E. Botez, O.-V. Nistor, D. G. Andronoiu, and G.-D. Mocanu, "Effect of different drying methods on moisture ratio and rehydration of pumpkin slices," *Food Chemistry*, vol. 195, pp. 104–109, 2016.
- [37] H. Fan, Y. Wu, X. Hu, J. Wu, and X. Liao, "Characteristics of thin-layer drying and rehydration of nata de coco," *International Journal of Food Science and Technology*, vol. 46, no. 7, pp. 1438–1444, 2011.
- [38] E. H. Ohaco, B. Ichiyama, J. E. Lozano, and A. De Michelis, "Rehydration of rosa rubiginosa fruits dried with hot air," *Drying Technology*, vol. 33, no. 6, pp. 696–703, 2014.

## Research Article

# Modeling and Analysis of New Multilevel Inverter for Solar Photovoltaic Power Plant

Xiaoqiang Guo,<sup>1</sup> Ran He,<sup>1</sup> and Mehdi Narimani<sup>2</sup>

<sup>1</sup>Department of Electrical Engineering, Yanshan University, Qinhuangdao, China

<sup>2</sup>Department of Electrical and Computer Engineering, McMaster University, Hamilton, ON, Canada

Correspondence should be addressed to Xiaoqiang Guo; yeduming@163.com

Received 22 June 2016; Revised 18 August 2016; Accepted 28 August 2016

Academic Editor: Md. Rabiul Islam

Copyright © 2016 Xiaoqiang Guo et al. This is an open access article distributed under the Creative Commons Attribution License, which permits unrestricted use, distribution, and reproduction in any medium, provided the original work is properly cited.

Solar photovoltaic (PV) power plant is an effective way to utilize the renewable energy sources. EMI is one of the major concerns in PV power plant. Typically, the multilevel inverters are used in high voltage PV power plant. However, the conventional multilevel inverters require more semiconductors, which complicate the circuit structure and control algorithm. In this paper, a novel five-level inverter is introduced for the high voltage PV power plant applications. The model of the inverter is analyzed. With the redundant switching states, a new modulation strategy is proposed to reduce the common-mode voltage and EMI. The proposed approach is able to eliminate the common-mode voltage; meanwhile it has the capability of balancing the capacitor voltages. The cosimulation tests with the Matlab/Simulink and S-function are carried out. The results verify the effectiveness of the proposed method.

## 1. Introduction

The solar photovoltaic power plant is recently attracting much attention throughout the world. Typically, the multilevel inverters are applied in high voltage PV power plant [1–4], mainly due to the high voltage capability, low switching frequency, and low power losses [5, 6]. The classic multilevel topologies include the diode clamped, flying capacitor, and cascaded H-bridge converters [7–12]. However, these kinds of converters give rise to common-mode voltage (CMV), which could induce the ground leakage currents, as well as electromagnetic interference (EMI). And the EMI is one of the major concerns in PV power plant applications [13–16]. To reduce the EMI, many interesting methods have been reported in literature. For example, the CMV reduction for cascaded converters has been discussed in [17–19]. The CMV reduction strategies for neutral point clamped topologies have been reported in [20–22]. As for other types of multilevel converters, the space vector modulation (SVM) for CMV reduction of a four-level inverter is presented in [23] and for a five-level inverter is presented in [24]. Unfortunately, the balance of the capacitor voltage is not considered in the abovementioned modulation strategies. Actually, the balance of the capacitor voltage is one of the key issues in multilevel

converters [7, 25]. Therefore, the modulation strategy which is able to eliminate the CMV and balance the capacitor voltage needs further investigation.

The objective of this paper is to present the modeling and analysis of a novel five-level inverter for PV power plant applications. The rest of the paper is organized as follows. Section 2 presents the analysis of the system operation principle. The proposed strategy is discussed in Section 3. The simulation interface and results are shown in Section 4. Finally, the conclusion is presented in Section 5.

## 2. Analysis of the New Five-Level Inverter

*2.1. Operation of the Novel Five-Level Inverter.* The novel five-level inverter, as shown in Figure 1, is a combination of a flying capacitor inverter and a neutral point clamped inverter presented in [26]. To ensure the equally spaced steps in the output voltages, the capacitors  $C_{x1}$  and  $C_{x2}$  ( $x = a, b, c$ ) are charged to  $1/4V_{dc}$  and  $C_{x3}$  is charged to  $3/4V_{dc}$ .  $V_{dc}$  is the dc-link voltage. As shown in Table 1, the phase voltages are  $V_{dc}/2$ ,  $V_{dc}/4$ ,  $0$ ,  $-V_{dc}/4$ , and  $-V_{dc}/2$ , with respect to the midpoint  $n$  of the dc-link, corresponding to the phase switching states  $S_k$  ( $k = a, b, c$ ) = 2, 1, 0, -1, -2.

TABLE 1: Switching states of the five-level inverter.

$S_{1x}$	$S_{2x}$	$S_{3x}$	$S_{4x}$	$S_{5x}$	$S_{6x}$	$S_{7x}$	$S_{8x}$	$V_{Cx1}$		$V_{Cx2}$		$V_{Cx3}$		$V_{xn}$	
								$i_x > 0$	$i_x < 0$	$i_x > 0$	$i_x < 0$	$i_x > 0$	$i_x < 0$		
1	1	1	1	0	0	0	0	—	—	—	—	—	—	$V_{dc}/2$	(a)
1	1	0	1	1	0	0	0	C	D	—	—	—	—		(b)
0	1	1	1	0	0	0	1	—	—	—	—	D	C	$V_{dc}/4$	(c)
1	0	1	1	0	0	1	0	D	C	D	C	C	D		(d)
1	1	0	0	1	1	0	0	C	D	C	D	—	—		(e)
1	0	0	1	1	0	1	0	—	—	D	C	C	D	0	(f)
0	1	0	1	1	0	0	1	C	D	—	—	D	C		(g)
0	0	1	1	0	0	1	1	D	C	D	C	—	—		(h)
0	0	0	1	1	0	1	1	—	—	D	C	—	—		(i)
1	0	0	0	1	1	1	0	—	—	—	—	C	D	$-V_{dc}/4$	(j)
0	1	0	0	1	1	0	1	C	D	C	D	D	C		(k)
0	0	0	0	1	1	1	1	—	—	—	—	—	—	$-V_{dc}/2$	(l)

C: charging; D: discharging.

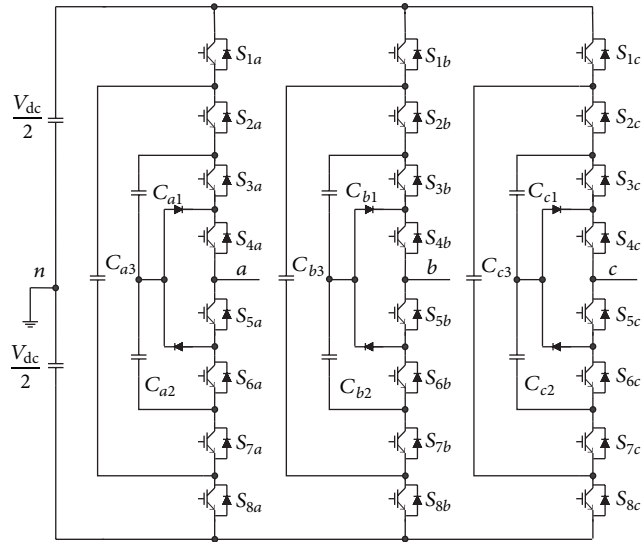


FIGURE 1: Schematic of the novel five-level inverter.

2.2. Common-Mode Voltage in the Novel Five-Level Inverter. The relationship between phase voltages and switching states can be expressed as follows:

$$V_{xn} = \begin{cases} \frac{V_{dc}}{2} & S_x = 2 \\ \frac{V_{dc}}{4} & S_x = 1 \\ 0 & S_x = 0 \\ -\frac{V_{dc}}{4} & S_x = -1 \\ -\frac{V_{dc}}{2} & S_x = -2 \end{cases} \quad x = a, b, c,$$

$$V_{an} = \frac{V_{dc}}{4} \times S_a,$$

$$V_{bn} = \frac{V_{dc}}{4} \times S_b,$$

$$V_{cn} = \frac{V_{dc}}{4} \times S_c.$$

(1)

The CMV is

$$V_{CM} = \frac{(V_{an} + V_{bn} + V_{cn})}{3}.$$

(2)

$S_{sum}$  can be defined as

$$S_{sum} = S_a + S_b + S_c.$$

(3)

And the CMV generated by switching states can be expressed as

$$V_{CM}(S_{sum}) = \frac{V_{dc}}{12} \times S_{sum}.$$

(4)

According to (4), the CMV of all the switching states can be calculated. Table 2 demonstrates the number of switching states corresponding to each CMV; for instance, 19 switching states make CMV zero. The switching states that make zero CMV are shown in Table 3, where

$$S_a + S_b + S_c = 0.$$

(5)

Figure 2 shows the 19 switching states that generate zero CMV where the switching states are symmetric in the space vector diagram. The switching states in the different sectors can be transformed into region I. For example, switching states (01-1), (-110), (-101), (0-11), and (1-10) can be converted to (10-1) in region I using the corresponding angle. Therefore, without considering the voltage balancing of the capacitors, the inverter can properly operate by employing the switching states and selecting the appropriate switching sequence.

TABLE 2: CMV and switching states.

CMV	The number of switching states
$V_{dc}/2$	1
$5V_{dc}/12$	3
$V_{dc}/3$	6
$V_{dc}/4$	10
$V_{dc}/6$	15
$V_{dc}/12$	18
0	19
$-V_{dc}/12$	18
$-V_{dc}/6$	15
$-V_{dc}/4$	10
$-V_{dc}/3$	6
$-5V_{dc}/12$	3
$-V_{dc}/2$	1

TABLE 3: Switching states with zero CMV.

CMV	Switching states
0	2-1-1, 20-2, 10-1, 11-2, 02-2, 01-1, -12-1, -220, -110, -211, -202, -101, -1-12, 0-22, 0-11, 1-21, 2-20, 1-10, 000

### 3. Proposed Strategy

**3.1. Modulation Strategy.** The CMV can not be eliminated in the conventional carrier-based modulation presented in [6] and this is because the different switching states generate different CMVs. For example, when the given reference falls into the shaded triangle in Figure 2, only one of the three switching states, namely, (10-1), is with zero CMV; however with the conventional modulation the CMV cannot be kept zero.

Figure 3(a) shows the three-level space vector diagram and Figure 3(b) is the same as Figure 2 rotated by 30 degrees. There are 27 switching states and 7 redundant switching states in Figure 3(a) where the redundant switching states operate similar to synthesize reference vectors. Therefore, regardless of redundant switching states, the number of actually working switching states is 19, which is the same as five-level switching states with zero CMV. In other words, there is corresponding relationship between three-level switching states and five-level switching states with zero CMV as shown in Table 4. For example, switching state (20-2) in a five-level space vector diagram with zero CMV is corresponding to a (200) switching state in a three-level diagram, and similarly switching state (10-1) in a five-level diagram is corresponding to switching states (211) or (100) in a three-level diagram.

Table 4 shows the relationship between the three-level switching states and five-level switching states with zero CMV. This feature results in the three-level modulation strategy employing Table 4 being used for a five-level inverter while achieving zero CMV.

To achieve the three-level modulation strategy, there are space vector modulation and carrier-based modulation. Due to the complex calculation and implementation of space

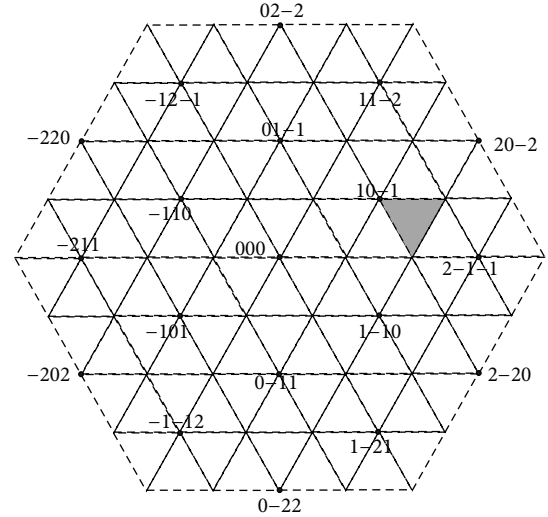


FIGURE 2: Space vector diagram in a five-level inverter.

TABLE 4: Relationship between three-level switching states and five-level switching states.

Three-level switching states	Five-level switching states
200	20-2
211, 100	10-1
210	11-2
211, 110	01-1
220	02-2
120	-12-1
020	-220
121, 010	-110
021	-211
022	-202
122, 011	-101
012	-1-12
112, 001	0-11
002	0-22
102	1-21
202	2-20
101, 212	1-10
201	2-1-1
222, 111, 000	000

vector modulation, the carrier-based modulation is used in this paper.

It should be noted that the zero CMV is achieved where the capacitor voltages are balanced. The following section will present a strategy to balance the capacitor voltages in each phase.

**3.2. Capacitor Voltage Balancing Strategy.** The capacitor voltages  $V_{C_{x1}}$  and  $V_{C_{x2}}$  should be kept at  $1/4$  of the dc bus voltage ( $V_{dc}/4$ ) and  $V_{C_{x3}}$  should be maintained at  $3/4$  of the dc bus voltage ( $3V_{dc}/4$ ) to ensure the proper operation of the five-level inverter. The voltage deviation of flying capacitor is

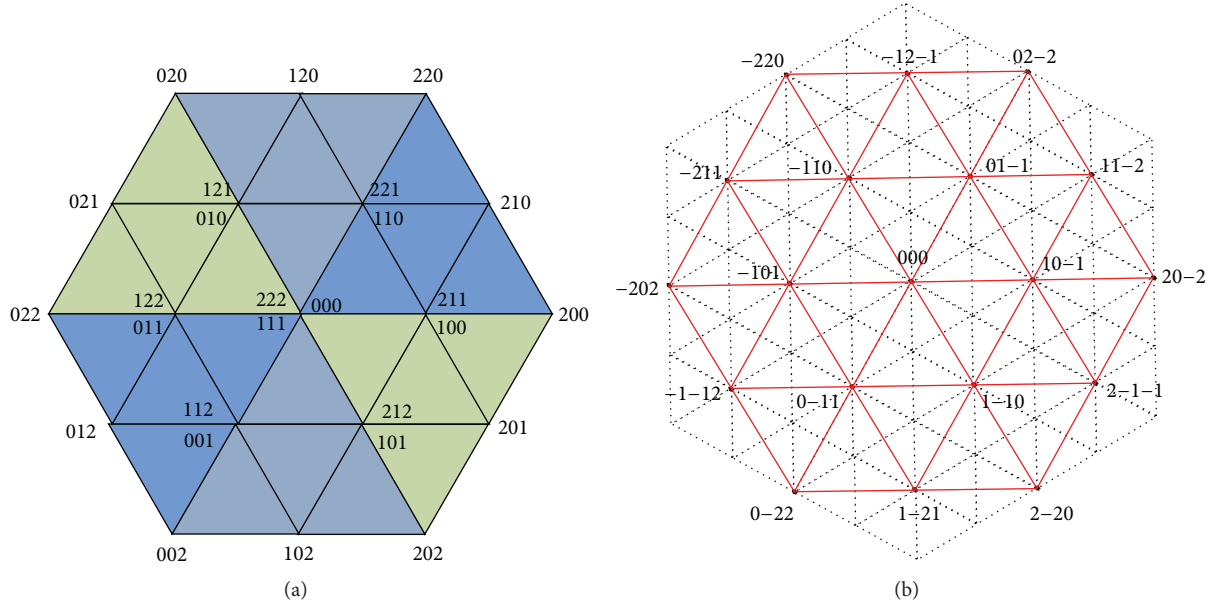


FIGURE 3: Space vector diagram: (a) three levels and (b) five levels (CMV = 0).

defined as the difference between flying capacitor voltage and the given value, which can be expressed as

$$\begin{aligned}\Delta V_{C_{x1}} &= V_{C_{x1}} - \frac{V_{dc}}{4}, \\ \Delta V_{C_{x2}} &= V_{C_{x2}} - \frac{V_{dc}}{4}, \\ \Delta V_{C_{x3}} &= V_{C_{x3}} - \frac{3V_{dc}}{4},\end{aligned}\quad (6)$$

where  $V_{C_{x1}}$ ,  $V_{C_{x2}}$ , and  $V_{C_{x3}}$  are capacitor voltages and  $\Delta V_{C_{x1}}$ ,  $\Delta V_{C_{x2}}$ , and  $\Delta V_{C_{x3}}$  are the deviation of capacitor voltages. The capacitor voltage can be balanced by controlling the absolute value of the deviation voltages close to zero.

The switching states  $(a) \sim (k)$  can affect the current flowing into the flying capacitors and can change the capacitor voltages by either charging or discharging. Taking switching state  $(b)$  as an example, when  $i_k > 0$ , the capacitor  $C_{x1}$  is charged, and when  $i_k < 0$ , the capacitor  $C_{x1}$  is discharged.

The capacitor voltage balancing strategy can be defined as follows:

- (i) Switching state  $S_k = 1$  is employed to control capacitor voltages  $V_{C_{x1}}$  and  $V_{C_{x3}}$ .
- (ii) Switching state  $S_k = -1$  is employed to control capacitor voltages  $V_{C_{x2}}$  and  $V_{C_{x3}}$ .
- (iii) Switching state  $S_k = 0$  is employed to control capacitor voltages  $V_{C_{x1}}$  and  $V_{C_{x2}}$ .

Details of the control method are shown in Tables 5, 6, and 7.

**3.3. Integration Capacitor Voltage Balancing with PWM Schemes.** The abovementioned capacitor voltage balancing

TABLE 5: Control table for capacitor voltage:  $S_x = 1$ .

$S_x$	Input conditions		Output results
	$\Delta V_{C1}$	$\Delta V_{C3}$	The chosen switching states
1	>0	>0	(c)
	>0	<0	(d)
	<0	>0	(c)
	<0	<0	(b)

TABLE 6: Control table for capacitor voltage:  $S_x = -1$ .

$S_x$	Input conditions		Output results
	$\Delta V_{C2}$	$\Delta V_{C3}$	The chosen switching states
-1	>0	>0	(j)
	>0	<0	(k)
	<0	>0	(j)
	<0	<0	(i)

TABLE 7: Control table for capacitor voltage:  $S_x = 0$ .

$S_x$	$i_x$	Input conditions		Output results
		$\Delta V_{C1}$	$\Delta V_{C2}$	The chosen switching states
0	>0	>0	>0	(h)
		>0	<0	(e)
		<0	>0	(g)
		<0	<0	(e)
0	<0	>0	>0	(e)
		>0	<0	(f)
		<0	>0	(h)
		<0	<0	(h)

method can be easily integrated with the proposed zero CMV modulation strategy. The schematic diagram of the

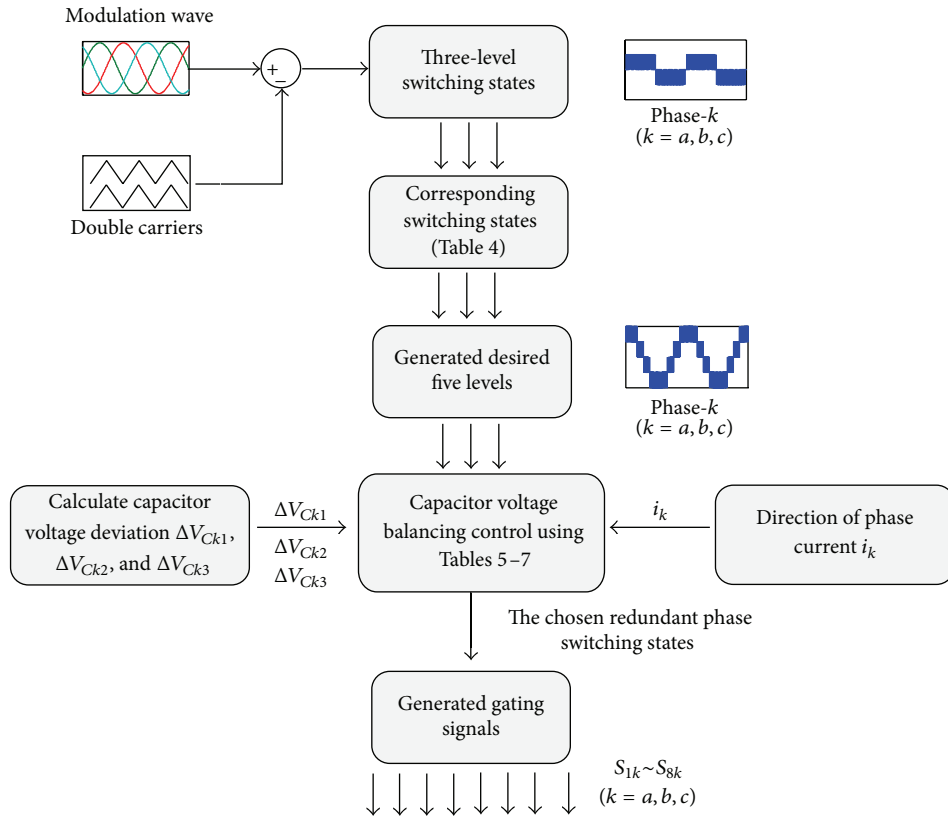


FIGURE 4: The control diagram of the novel five-level inverter.

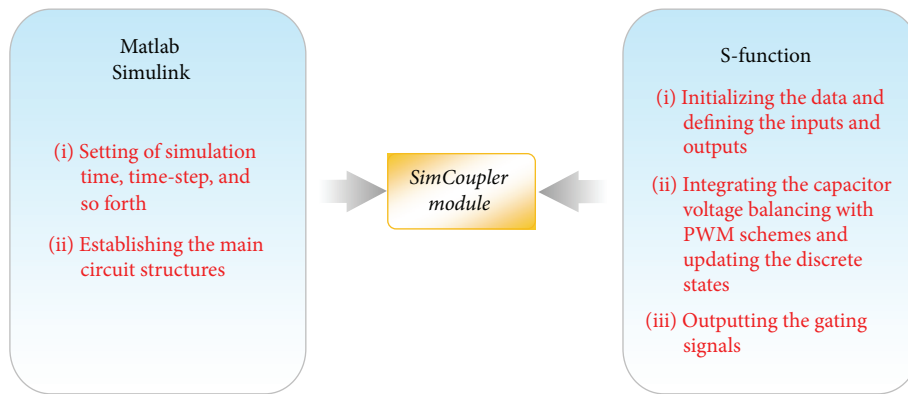


FIGURE 5: Matlab/Simulink and S-function cosimulation.

integration is shown in Figure 4. The procedure consists of the following steps:

- (1) First, the three-level switching states are generated by a dual-carrier-based PWM scheme.
- (2) According to Table 4, the five-level switching states corresponding to three-level switching states can be determined to keep the novel five-level inverter with zero CMV.
- (3) Finally, the capacitor voltage balancing can be achieved by using control tables of Table 5, 6, and 7 and considering the direction of phase current  $i_k$ .

#### 4. Simulation Interface and Results

The cosimulation between Matlab/Simulink and S-function is realized to verify the effectiveness of the proposed method, as shown in Figure 5. The simulation parameters are listed in Table 8. In Simulink environment, the model of each system component is expressed by block diagram, and the lines among the block diagram indicate the direction of the signal flow. From the perspective of the whole system, *Simulink* is fast and convenient. However, for some complex and lengthy program code, it is not suitable with modularity. That is the reason why S-function is used for the simulation interface.

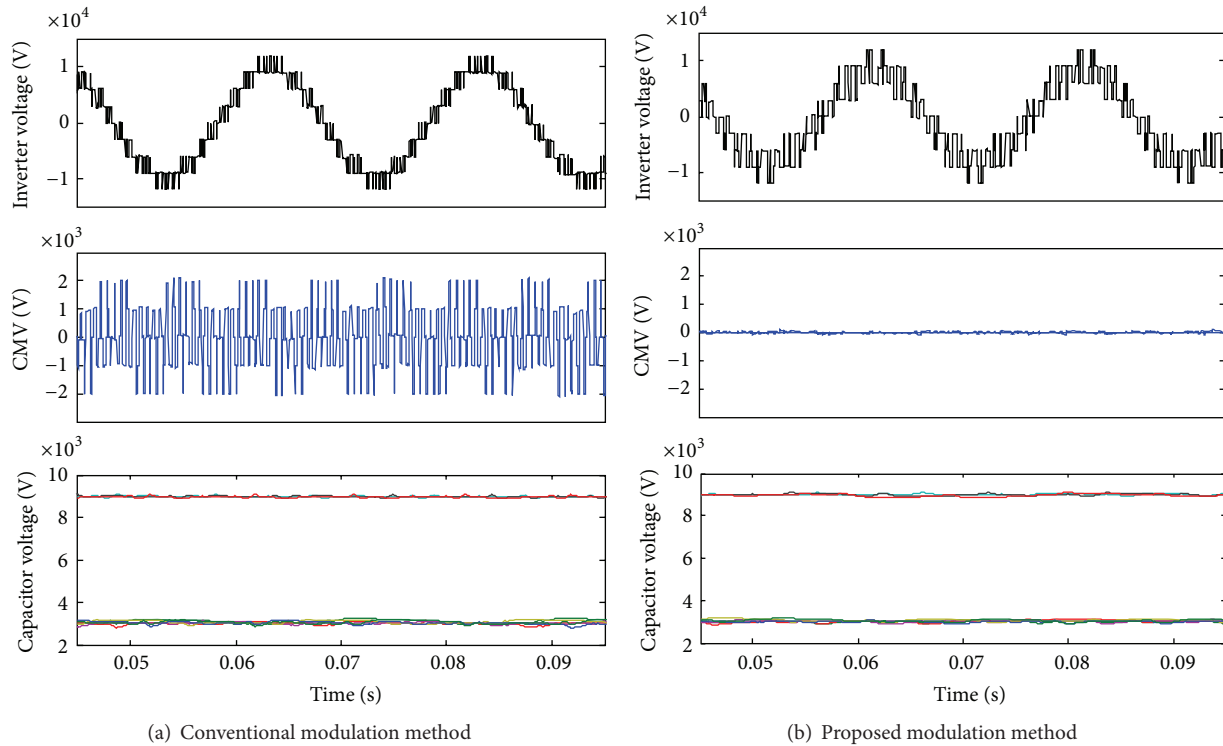


FIGURE 6: Simulation results of different modulations.

TABLE 8: Simulation parameters.

Inverter parameters	Values
Input dc voltage	12 kV
Capacitor	1000 $\mu$ F
Inverter rating	3 MVA
Output frequency	50 Hz
Output inductance	5 mH
Power factor	0.9
Modulation index	0.95
Switching frequency	700 Hz

The cosimulation system is very useful to tackle the demand of the simulation and implementation of complex multilevel inverter systems.

Figure 6 shows the performance of the five-level inverter with conventional and proposed modulations. The total harmonic distortion of the line-line voltage with conventional modulation is 17.32% and the CMV cannot be eliminated, varying within the range of  $V_{dc}/6$  and  $-V_{dc}/6$ . Whereas the total harmonic distortion of the line-line voltage with proposed modulation is 37.41%, however, the CMV can be effectively eliminated. It should be noted that, like other modulation strategy regarding the common-mode voltage reduction, the voltage THD will be higher. However, it mainly consists of high frequency components. So the THD can be reduced with the output filter, as shown in Figure 7.

To evaluate the dynamic performance of the proposed modulation, a step change from half load to full load has been

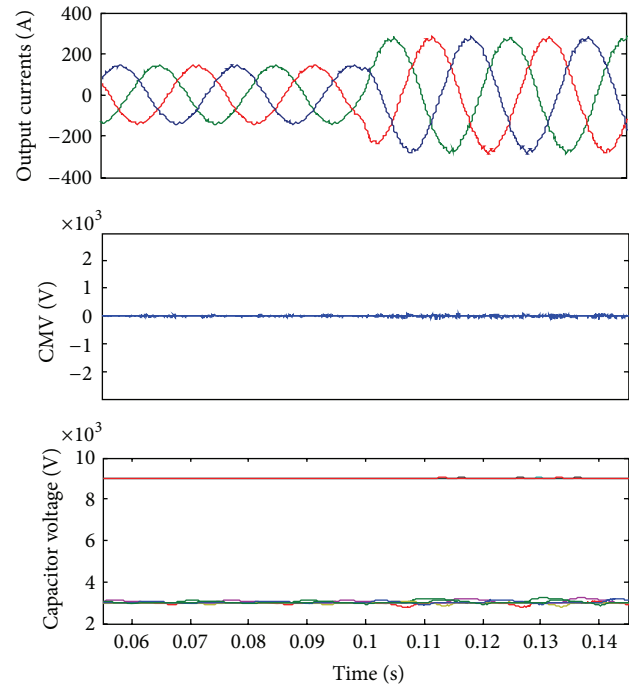


FIGURE 7: Simulation results from half to full loads.

studied at  $t = 0.1$  s, as shown in Figure 7. The voltage of the flying capacitors can be maintained at the nominal values and the CMV can be kept constant at zero before and after the step change.

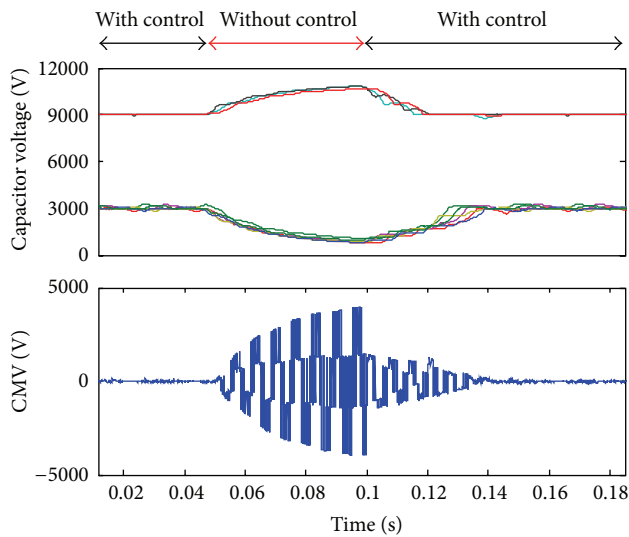


FIGURE 8: Simulation results with and without proposed controller.

In order to verify the performance of the proposed control strategy with and without the proposed control, the simulation test is carried out and shown in Figure 8. In this case, the proposed controller is enabled and, at  $t = 0.05$  s, the controller is disabled; then the controller is reactivated at  $t = 0.1$  s. As can be seen from Figure 8, when the controller is deactivated, the capacitor voltages diverge and the CMV gets bigger. However, when the controller is reactivated, the capacitor voltage starts converging and the CMV approaches zero rapidly, which verifies the effectiveness of the proposed control strategy.

## 5. Conclusion

The modeling and analysis of a novel five-level inverter for PV power plant applications has been presented in this paper. The common-mode voltage can be eliminated by selecting the specific switching states. Also, the balancing of flying capacitor voltages can be achieved with a simple control strategy. In contrast to the conventional solutions, our proposal reduces the number of calculations which simplifies the implementation, and thus it is very attractive for PV power plant applications, where the EMI is a major concern. It should be noted that this paper mainly focuses on the CMV and EMI reduction of the five-level inverter for PV power plant. The MPPT and other issues of PV power plant are the subject of the future research.

## Competing Interests

The authors declare that there is no conflict of interests regarding publication of this paper.

## Acknowledgments

This work was supported by Science Foundation for Distinguished Young Scholars of Hebei Province (E2016203133) and China Postdoctoral Science Foundation (2015T80230).

## References

- [1] H. Nademi, A. Das, R. Burgos, and L. E. Norum, "A new circuit performance of modular multilevel inverter suitable for photovoltaic conversion plants," *IEEE Journal of Emerging and Selected Topics in Power Electronics*, vol. 4, no. 2, pp. 393–404, 2016.
- [2] S. Essakiappan, H. S. Krishnamoorthy, P. Enjeti, R. S. Balog, and S. Ahmed, "Multilevel medium-frequency link inverter for utility scale photovoltaic integration," *IEEE Transactions on Power Electronics*, vol. 30, no. 7, pp. 3674–3684, 2015.
- [3] M. Hamzeh, A. Ghazanfari, H. Mokhtari, and H. Karimi, "Integrating hybrid power source into an Islanded MV microgrid using CHB multilevel inverter under unbalanced and nonlinear load conditions," *IEEE Transactions on Energy Conversion*, vol. 28, no. 3, pp. 643–651, 2013.
- [4] L. Liu, H. Li, Y. Xue, and W. Liu, "Decoupled active and reactive power control for large-scale grid-connected photovoltaic systems using cascaded modular multilevel converters," *IEEE Transactions on Power Electronics*, vol. 30, no. 1, pp. 176–187, 2015.
- [5] J. Rodríguez, S. Bernet, B. Wu, J. O. Pontt, and S. Kouro, "Multilevel voltage-source-converter topologies for industrial medium-voltage drives," *IEEE Transactions on Industrial Electronics*, vol. 54, no. 6, pp. 2930–2945, 2007.
- [6] S. Kouro, M. Malinowski, K. Gopakumar et al., "Recent advances and industrial applications of multilevel converters," *IEEE Transactions on Industrial Electronics*, vol. 57, no. 8, pp. 2553–2580, 2010.
- [7] K. Wang, Z. Zheng, Y. Li, K. Liu, and J. Shang, "Neutral-point potential balancing of a five-level active neutral-point-clamped inverter," *IEEE Transactions on Industrial Electronics*, vol. 60, no. 5, pp. 1907–1918, 2013.
- [8] J. Zaragoza, J. Pou, S. Ceballos, E. Robles, C. Jaen, and M. Corbalán, "Voltage-balance compensator for a carrier-based modulation in the neutral-point-clamped converter," *IEEE Transactions on Industrial Electronics*, vol. 56, no. 2, pp. 305–314, 2009.
- [9] J. Pou, J. Zaragoza, S. Ceballos, M. Saeedifard, and D. Boroyevich, "A carrier-based PWM strategy with zero-sequence voltage injection for a three-level neutral-point-clamped converter," *IEEE Transactions on Power Electronics*, vol. 27, no. 2, pp. 642–651, 2012.
- [10] J. I. Leon, S. Kouro, S. Vazquez et al., "Multidimensional modulation technique for cascaded multilevel converters," *IEEE Transactions on Industrial Electronics*, vol. 58, no. 2, pp. 412–420, 2011.
- [11] S. Kouro, J. Rodríguez, B. Wu, S. Bernet, and M. Perez, "Powering the future of industry: high-power adjustable speed drive topologies," *IEEE Industry Applications Magazine*, vol. 18, no. 4, pp. 26–39, 2012.
- [12] J. I. Leon, S. Kouro, L. G. Franquelo, J. Rodríguez, and B. Wu, "The essential role and the continuous evolution of modulation techniques for voltage-source inverters in the past, present, and future power electronics," *IEEE Transactions on Industrial Electronics*, vol. 63, no. 5, pp. 2688–2701, 2016.
- [13] R. Araneo, S. Lammens, M. Grossi, and S. Bertone, "EMC issues in high-power grid-connected photovoltaic plants," *IEEE Transactions on Electromagnetic Compatibility*, vol. 51, no. 3, pp. 639–648, 2009.
- [14] Z. Wang, S. Fan, Y. Zheng, and M. Cheng, "Design and analysis of a CHB converter based PV-battery hybrid system

- for better electromagnetic compatibility," *IEEE Transactions on Magnetics*, vol. 48, no. 11, pp. 4530–4533, 2012.
- [15] W. Chen, Y. Duan, L. Guo, Y. Xuan, and X. Yang, "Modeling and prediction of radiated emission from solar cell in a photovoltaic generation system," *IEEE Journal of Photovoltaics*, vol. 6, no. 2, pp. 540–545, 2016.
- [16] Y. Bae and R.-Y. Kim, "Suppression of common-mode voltage using a multicentral photovoltaic inverter topology with synchronized PWM," *IEEE Transactions on Industrial Electronics*, vol. 61, no. 9, pp. 4722–4733, 2014.
- [17] P. C. Loh, D. G. Holmes, Y. Fukuta, and T. A. Lipo, "Reduced common-mode modulation strategies for cascaded multilevel inverters," *IEEE Transactions on Industry Applications*, vol. 39, no. 5, pp. 1386–1395, 2003.
- [18] A. K. Gupta and A. M. Khambadkone, "A space vector modulation scheme to reduce common mode voltage for cascaded multilevel inverters," *IEEE Transactions on Power Electronics*, vol. 22, no. 5, pp. 1672–1681, 2007.
- [19] J. Rodríguez, J. Pontt, P. Correa, P. Cortés, and C. Silva, "A new modulation method to reduce common-mode voltages in multilevel inverters," *IEEE Transactions on Industrial Electronics*, vol. 51, no. 4, pp. 834–839, 2004.
- [20] H. Zhang, A. Von Jouanne, S. Dai, A. K. Wallace, and F. Wang, "Multilevel inverter modulation schemes to eliminate common-mode voltages," *IEEE Transactions on Industry Applications*, vol. 36, no. 6, pp. 1645–1653, 2000.
- [21] H.-J. Kim, H.-D. Lee, and S.-K. Sul, "A new PWM strategy for common-mode voltage reduction in neutral-point-clamped inverter-fed ac motor drives," *IEEE Transactions on Industry Applications*, vol. 37, no. 6, pp. 1840–1845, 2001.
- [22] A. Von Jouanne, S. Dai, and H. Zhang, "A multilevel inverter approach providing DC-link balancing, ride-through enhancement, and common-mode voltage elimination," *IEEE Transactions on Industrial Electronics*, vol. 49, no. 4, pp. 739–745, 2002.
- [23] N. Rashidi-Rad, A. Rahmati, A. Abrishamifar et al., "Reduction of common-mode voltage in an even level inverter by a new SVM method," *International Journal of Advanced Computer Science*, vol. 2, no. 9, pp. 343–347, 2012.
- [24] M. M. Renge and H. M. Suryawanshi, "Five-level diode clamped inverter to eliminate common mode voltage and reduce dv/dt in medium voltage rating induction motor drives," *IEEE Transactions on Power Electronics*, vol. 23, no. 4, pp. 1598–1607, 2008.
- [25] C. Wang and Y. Li, "Analysis and calculation of zero-sequence voltage considering neutral-point potential balancing in three-level NPC converters," *IEEE Transactions on Industrial Electronics*, vol. 57, no. 7, pp. 2262–2271, 2010.
- [26] M. Narimani, B. Wu, G. Cheng, and N. Zargari, "Improved multilevel voltage source converters and systems," United States US Patent 20,140,376,287 A1.